Thesis for the Degree of Doctor of Philosophy

Alkali Uptake and Release from Oxygen Carriers in Chemical Looping Applications

Development and Application of Reactor Systems and Measurement Techniques

Viktor Andersson

Department of Chemistry and Molecular Biology

University of Gothenburg

Gothenburg, Sweden 2023

Alkali Uptake and Release from Oxygen Carriers in Chemical Looping Applications
Development and Application of Reactor Systems and Measurement Techniques
ISBN 978-91-8069-543-5

Doktorsavhandling vid Göteborgs Universitet
http://hdl.handle.net/2077/78816

Atmospheric Science
Department of Chemistry and Molecular Biology
University of Gothenburg
SE-413 90 Gothenburg
Sweden

Printed by Stema Specialtryck AB
Borås, Sweden 2023

ISBN 978-91-8069-543-5 (print)
ISBN 978-91-8069-544-2 (pdf)

Alkali Uptake and Release from Oxygen Carriers in Chemical Looping Applications

Development and Application of Reactor Systems and Measurement Techniques

VIKTOR ANDERSSON

Abstract

Chemical looping combustion (CLC) of biomass is a heat and power generation technology with minimal associated costs for carbon capture, potentially resulting in negative CO_2 emissions. The CLC technology utilizes fluidized beds of oxygen carrier (OC) particles to separate CO_2 from the combustion air. The high content of potassium and sodium compounds in biomass fuels may cause detrimental problems during thermal conversion, including agglomeration, fouling and corrosion, while also enhancing conversion processes due to their catalytic abilities. Further knowledge about processes involving these alkali metals, including their uptake and release from OC materials and the control of alkali emission, is critical for the upscaling and commercialization of biomass CLC.

The aim of this thesis is to improve the understanding of interactions between alkali compounds and OCs under conditions representative of biomass CLC. A novel technique based on temperature modulated surface ionization was developed to determine the contributions of alkali chlorides, hydroxides, and sulfates to the flux from different reactors. A novel laboratory-scale reactor was developed, facilitating continuous alkali vapor injection to a fluidized bed while monitoring the concentrations of alkali and gas in the reactor exhaust. An additional method was developed to monitor the real-time alkali release and mass loss from small, fixed bed samples, including OC particles and solid biomass.

The type of OC material is observed to play a crucial role in alkali uptake, where fluidized beds of the promising CLC materials: calcium manganite, manganese oxide, and ilmenite, exhibiting varying levels of efficiency depending on the specific gas conditions present. Ilmenite showed near complete absorption of the injected alkali, especially during reducing conditions, making it a promising option to limit alkali emissions. The alkali speciation analysis revealed that NaCl and KCl were the predominant alkali species emitted during NaCl and KCl injection, and a similar pattern was observed for alkali sulfates. Alkali hydroxide injections resulted in highly efficient alkali uptake with emissions dominated by alkali hydroxides and chlorides. The study highlights the balance between alkali absorption efficiency and fuel conversion and oxidizing efficiency of the OC materials. While ilmenite demonstrated excellent alkali uptake, manganese oxide and calcium manganite exhibited superior fuel conversion and oxidizing efficiency. In addition, ilmenite previously used in an industrial process releases alkali in both inert and oxidizing environments at high temperatures. The described development and application of new methods are concluded to open new possibilities to understand and optimize biomass CLC.

Keywords: Alkali speciation, Biomass, Chemical looping combustion, Oxygen carriers

Sammanfattning

Kemcyklisk förbränning av biomassa kan användas för värme- och elproduktion med minimala kostnader för koldioxidinfångning, vilket kan resultera i negativa CO_2 utsläpp. Tekniken använder fluidiserade bäddar av syrebärarpartiklar för att separera CO_2 från förbränningsluften. De höga halterna av kalium- och natriumföreningar i biomassa kan orsaka stora problem för termisk bränsleomvandling, så som agglomerering, påväxt och korrosion, medan de samtidigt kan förbättra förbränningsprocessen genom sin katalytiska förmåga. För att kunna skala upp och kommersialisera kemcyklisk förbränning av biomassa så krävs förbättrade kunskaper om alkaliprocesser, inklusive absorption och desorption från syrebärarmaterial samt speciering av alkaliutsläpp i rökgaserna.

Målet med denna avhandling är att förbättra förståelsen av alkaliföreningars växelverkan med syrebärare under förhållanden som representerar kemcyklisk förbränning av biomassa. En ny mätmetod som baseras på ytjonisation med temperaturmodulering har utvecklats för att bestämma bidragen av alkaliklorider, -hydroxider och -sulfater i utsläppen från olika reaktorsystem. En ny reaktor på laboratorieskala utvecklades, där alkaligas förs in i en fluidiserad bädd medan koncentrationen av alkali och gaser mäts i reaktoravgaserna. Ytterligare en metod utvecklades, där alkaliutsläpp och viktminskning mäts i realtid från små prover, så som syrebärarpartiklar eller biomassa.

Typen av syrebärare har stor betydelse för alkaliupptag och fluidbäddar av tre lovande material för kemcyklisk förbränning: kalciummanganat, manganoxid och ilmenit, uppvisar olika grad av upptag beroende på omgivande miljö. Ilmenit upptar nästan all introducerad alkali, speciellt under reducerande förhållanden, vilket gör den eftertraktad med avseende på minskade alkaliutsläpp. Mätningar visar att KCl och NaCl dominerar utsläppen när dessa alkalisalter förs in i reaktorn, och liknande resultat erhölls för alkalisulfater. Injektion av alkalihydroxid resulterande i högt alkaliupptag av fluidbäddarna, och alkaliutsläppen domineras av alkalihydroxider och alkaliklorider. Studien visar på betydelsen av en avvägning mellan effektiviteten av alkaliabsorption och bränsleomvandling/syreupptagningseffektivitet hos syrebärarna. Medan ilmenit visar excellent alkaliupptag, så är manganoxid och kalciummanganat överlägsna med avseende på bränsleomvandling och oxidationseffektivitet. Det observerades även att ilmenit som tidigare använts vid industriförbränning av biomassa släpper ifrån sig alkali i både inert och oxiderande miljö vid höga temperaturer. Sammanfattningsvis konstateras att utvecklingen och tillämpningen av de nya metoderna skapar nya möjligheter att förstå och optimera kemcyklisk förbränning av biomassa.

List of Publications

I Viktor Andersson, Amir H. Soleimanisalim, Xiangrui Kong, Fredrik Hildor, Henrik Leion, Tobias Mattisson, Jan B.C. Pettersson
Alkali-wall interactions in a laboratory-scale reactor for chemical looping combustion studies. Fuel Processing Technology (**2021**), 217, 106828

II Viktor Andersson, Amir H. Soleimanisalim, Xiangrui Kong, Henrik Leion, Tobias Mattisson, Jan B.C. Pettersson
Alkali interactions with a calcium manganite oxygen carrier used in chemical looping combustion. Fuel Processing Technology (**2022**), 227, 107099

III Viktor Andersson, Yaxin Ge, Xiangrui Kong, Jan B.C. Pettersson
A Novel Method for On-Line Characterization of Alkali Release and Thermal Stability of Materials Used in Thermochemical Conversion Processes. Energies (**2022**), 15, 4365

IV Viktor Andersson, Ivana Stanicic, Xiangrui Kong, Henrik Leion, Tobias Mattisson, Jan B.C. Pettersson
Alkali Desorption from Ilmenite Oxygen Carrier Particles used in Biomass Combustion. Manuscript submitted for publication to Fuel (**2023**).

V Viktor Andersson, Xiangrui Kong, Henrik Leion, Tobias Mattisson, Jan B.C. Pettersson
Design and First Application of a Novel Laboratory Reactor for Alkali Studies in Chemical Looping Applications. Fuel Processing Technology (**2023**), 252, 107988

VI Viktor Andersson, Xiangrui Kong, Jan B. C. Pettersson
Online Speciation of Alkali Compounds by Temperature-Modulated Surface Ionization: Method Developement and Application to Thermal Conversion. Manuscript submitted for publication to Energy & Fuels (**2023**).

VII Viktor Andersson, Xiangrui Kong, Henrik Leion, Tobias Mattisson, Jan B.C. Pettersson
Gaseous Alkali Interactions with Ilmenite, Manganese Oxide and Calcium Manganite under Chemical Looping Combustion Conditions. Manuscript submitted for publication to Fuel Processing Technology (**2023**).

Statement of contribution

Viktor Andersson has contributed to the papers in the following ways:

I Principal author, conduction of lab experiments, analysis and result evaluation.

II Principal author, conduction of lab experiments, SEM analysis and result evaluation.

III Principal author, conduction of experiments, method development and conceptualization, analysis and result evaluation.

IV Principal author, conduction of lab experiments, parts of material analysis and kinetic calculations, analysis and result evaluation.

V Principal author, CFD simulation and evaluation, design and implementation of new lab equipment, method development, conduction of lab experiments, analysis and result evaluation.

VI Principal author, method development and conceptualization, conduction of lab experiments, analysis and result evaluation.

VII Principal author, conduction of lab experiments, analysis and result evaluation.

Related peer-reviewed papers not included in this thesis

- Ivana Stanicic, Viktor Andersson, Malin Hanning, Tobias Mattisson, Rainer Backman, Henrik Leion
  Combined manganese oxides as oxygen carriers for biomass combustion — Ash interactions
  Chemical Engineering Research and Design (**2019**), 149, 104-120
- Xiangrui Kong/Ivana Stanicic, Viktor Andersson, Tobias Mattisson, Jan B.C. Pettersson
  Phase Recognition in SEM-EDX Chemical Maps using Positive Matrix Factorization
  MethodsX (**2023**), 11, 102384.

Acknowledgements

I would like to express my deepest gratitude to several individuals that helped me along my Ph.D. journey.

Firstly, I would like to thank my supervisor Jan Pettersson for believing in me, for your guidance and for your unwavering support. You have not only helped me immensely on my journey to becoming a scientist, you have also encouraged me and always given me credit for my achievements along the way. The combination of great supervision and the feeling of pride and joy made this a very pleasant journey.

I would like to extend my gratitude to my co-supervisors, Xiangrui Kong, Tobias Mattisson and Henrik Leion. Kong, you never fail to impress me with your high efficiency and profound knowledge. You truly helped me greatly, especially during my first years and now in the final process of writing my thesis. Tobias, you have always intrigued me to expand our studies and explore alternative ways of conducting our research. I always leave our meetings feeling motivated and filled with several new ideas. Henrik, thank you for introducing me to this field of research and for guiding me through my studies around the world. Your support and encouragement made me pursue a career in science.

I have always been surrounded by supportive and inspirational colleagues. Amir, thank you for a very pleasant collaboration in my first year. You truly helped me kick-start my research with your knowledge and experience. Thank you, Fredrik and Victor, for all the practical assistance in the lab throughout the years. Pavleta, thank you for all the inspirational and encouraging discussions. I would also like to thank all my great colleagues at the Atmospheric Science division at GU and the Chemical Looping colleagues at Chalmers.

A very special thank you to Ivana. I am beyond grateful to have such an exceptional friend and colleague to share this journey with. You have helped me countless of times, both during our Chalmers and Ph.D. studies, and it gives me immense joy to share both challenges and achievements with you.

I would like to thank my parents, relatives and friends for the endless support, but yet relaxed attitude towards higher education. I feel truly fortunate to have such amazing people in my life.

Lastly, I would like to thank the most important person in my life. Dominique, my friend, partner and soulmate. You always support and believe in me, and it is a true privilege to pursue a career alongside you.

Viktor Andersson

Gothenburg, Sweden, 2023

Contents

List of Abbreviations

AR	Air Reactor
BECCS	Bioenergy Carbon Capture and Storage
CCS	Carbon Capture and Sorage
CFB	Circulating Fluidized Bed
CFD	Computational Fluid Dynamics
CLC	Chemical Looping Combustion
CLG	Chemical Looping Gasification
CLOU	Chemical Looping with Oxygen Uncoupling
EDS	Energy Dispersive Spectroscopy
FBC	Fluidized Bed Combustion
FR	Fuel Reactor
GHG	Greenhouse Gas
HTC	High Temperature Corrosion
IPCC	Intergovernmental Panel for Climate Change
KPS	Knopf, Pöschl and Shiraiwa
ML	Monolayer
NET	Neutral Energy Technology
OC	Oxygen Carrier
OCAC	Oxygen Carrier Aided Combustion
SEM	Scanning Electron Microscope
SI	Surface Ionization
SID	Surface Ionization Detector
SMPS	Scanning Mobility Particle Sizer

TGA Thermogravimetric Analyzer

TMSI Temperature Modulation Surface Ionization

XMT X-ray Microtomography

XPS X-ray Photoelectron Spectroscopy

XRD X-ray Diffraction

Part I

Description of Thesis

1

Introduction

In an era defined by the pressing challenges of climate change and dwindling fossil fuel reserves, more than 80% of the world's total energy consumption is still provided by fossil fuel sources [1]. As of 2014, CO_2 emissions from fossil fuel combustion represented almost 80% of the global anthropogenic greenhouse gas emissions (GHGs) [2]. The large cumulative volume and the long residence times in the atmosphere makes CO_2 the largest contributor to global warming [3]. Although both the Paris Agreement (2015) and the Glasgow Climate Pact (2021) commit to limit global warming, energy-related CO_2 emissions continued to grow by 0.9% in 2022, despite a global economic slowdown [4–6].

As societies grapple with the imperative to drastically reduce GHG emissions, researchers, policymakers, and industries are increasingly turning their attention to CO_2-neutral energy alternatives. One example is biomass, which consumes similar amount of CO_2 during its growth as is subsequently emitted during its combustion, making it regarded as a CO_2-neutral fuel source. Another way to drastically reduce CO_2 emissions from the heat and power generation sector is by utilizing carbon capture and storage (CCS) technologies [7–9]. However, reducing emissions of GHGs is probably not enough to reach the goal of limited global warming that was set by the Paris Agreement [10]. Instead, the Intergovernmental Panel on Climate Change (IPCC) suggests the implementation of negative emission technologies (NETs) as a measure to reach the climate goals [11]. Although several NETs are proposed, one low-cost alternative is the use of CCS in biomass conversion applications, called bioenergy with carbon capture and storage (BECCS) [12, 13]. Chemical looping combustion (CLC) is a promising technology in which a variety of fuels, including solid biomass, can be thermally converted with subsequent CO_2 capture and storage, enabling net negative CO_2 emissions [14, 15]. The technology is most commonly realized as two interconnected circulating fluidized bed (CFB) reactors, where the bed material consists of solid metal oxide particles called oxygen carriers (OC). The products from the fuel conversion in a CLC system mainly consist of water and CO_2. The CLC process provides the same net energy release as conventional combustion, but with the added benefit of low-cost CO_2 sequestration, after water has been removed by condensation [16, 17].

The transition from fossil fuels to biomass in the pursuit of achieving neutral or negative CO_2 emissions relies on a sustainable supply of biomass. The feasibility of using biomass in the energy generation sector often depends on several socio-economic factors, including competition with the food industry and the loss of biodiversity or other environmental

impacts [18]. However, biomass can be utilized from several different sources, such as plantations of fast-growing crops, agricultural residues or wood acquired from afforestation of degraded land. The wide range of sources increases the potential for biomass to be implemented in the heat and power generation sector, with an overall technical energy potential of 160 – 270 EJ by 2050 [19]. This corresponds to 27 – 45% of the world's total energy supply in 2019, which was 600 EJ [1]. In addition, implementation of biomass may cause significant operational challenges to the conversion technologies. Compared to fossil fuels, biomass is generally accompanied by a high water content, generates a lower heating value and contains significant amounts of inorganic compounds [20]. Among the most problematic aspects are the high content of alkali metals, primarily K and Na, which are readily released during the conversion process.

Alkali metals are known for their unique chemical properties to either catalyze or inhibit chemical reactions, depending on the specific conditions. Although studies show that alkali metals have catalytic effects on tar cracking [21, 22], char reactivity [23, 24] and biomass gasification rates [25, 26], their presence in fluidized bed combustion (FBC) is often related with degradation issues. Some of the most common issues include agglomeration of fluidized bed particles [20, 27–29], alkali-induced fouling and corrosion of heat extraction equipment [20, 30–32] or interference with downstream components used for gas reforming [33]. Another important aspect to consider is the interaction between alkali metals and the OC bed material that provides the oxygen required to convert the fuel in a CLC process. As such, a comprehensive understanding of alkali metal behavior in chemical looping is essential for optimizing system performance and designing robust and sustainable processes. However, most of the alkali-related studies in the literature are based on off-line characterization of material from industrial processes and related to solid-solid interactions between ash and OC [34–36]. Meanwhile, significant fractions of the alkali will likely be in the gas phase surrounding the OC bed material, and gas-solid reactions are expected to be highly important, but not studied to a large extent in the literature. The complex behavior of alkali compounds makes in-depth studies on gaseous alkali processes challenging. Chemical transformations or condensation on surrounding surfaces can pose problems during extractive sampling in large-scale experiments, while steep temperature gradients and large surface-to-volume ratios are some challenges in laboratory-scale experiments.

The primary aim of this thesis is to gain knowledge about the gas-solid interactions between alkali and OC materials. This is done by examining the uptake and release of gaseous alkali compounds by OC materials under fluidized bed conditions representative of CLC operation. The work includes developing novel alkali monitoring methods and designing new laboratory reactor systems to monitor the alkali dynamics between different alkali salt compounds and different OC materials. The knowledge gained will enhance understanding of alkali behavior in both gas and condensed phases, facilitating systematic studies related to alkali interactions within biomass conversion technologies. This research seeks to enable the development of more efficient and reliable biomass conversion technologies with the potential to outperform and eventually replace the fossil-based energy generation industry on which we currently rely.

2

Background

The following sub-sections present the background on applications that utilize oxygen carriers to enable or enhance the thermal conversion of biomass, including CLC. Subsequent sections provide insight into biomass utilization with a particular emphasis on alkali release and its effects on the processes related to heat and power generation, and an introduction to alkali monitoring techniques.

2.1 Chemical looping technologies

There are a number of ways to capture CO_2 from commercial biomass-fired power plants to obtain BECCS. Either by post-combustion methods to separate CO_2 from the other flue gases [37], pre-combustion methods where the fuel is first gasified to CO and H_2 and then reformed to consist mainly of CO_2 and H_2 [9], or oxyfuel combustion where pure oxygen is used to oxidize the fuel [38]. These are expensive ways to separate the CO_2 due to their need for energy-intensive gas separation. A comparably cheaper option for CO_2 sequestration from power production plants is CLC.

The CLC technology, which has been developed in recent decades, shows promising results for biomass combustion [39–43]. It operates on the principle of separating the fuel from the combustion air by using two separate fluidized bed reactors, schematically shown in Figure 2.1a. One reactor containing the combustion air, is termed the air reactor (AR), while the other that houses the fuel is called the fuel reactor (FR). Between the two reactors circulates metal oxide particles (denoted M_xO_y in Figure 2.1), called oxygen carriers (OCs). These OCs transfer both oxygen and heat from the AR to the FR. As the OC particles are fluidized by air in the AR, they undergo oxidation via the exothermic reaction 2.1. Following this, the oxidized OCs are conveyed to the FR,where they undergo reduction while oxidizing the fuel according to reaction 2.2. Lastly, the reduced OCs are transported back to the AR for regeneration, completing the redox loop.

$$M_xO_{y-1} + \frac{1}{2}O_2 \rightarrow M_xO_y \tag{2.1}$$

$$(2n+m)M_xO_y + C_nH_{2m} \rightarrow (2n+m)M_xO_{y-1} + mH_2O + nCO_2 \tag{2.2}$$

Compared to conventional combustion in which the oxygen demand is met by mixing the fuel with air, in CLC, the oxygen demand is fulfilled by the OC [14]. While the flue gases from conventional combustion are diluted with nitrogen from the air, the flue gases from the FR in a CLC process consist mainly of CO2 and water. By avoiding the expensive gas separation in CLC, the cost for CO2 capture is reduced compared to other technologies, and the total heat generated from reaction 2.1 and 2.2 matches that of conventional combustion [44].

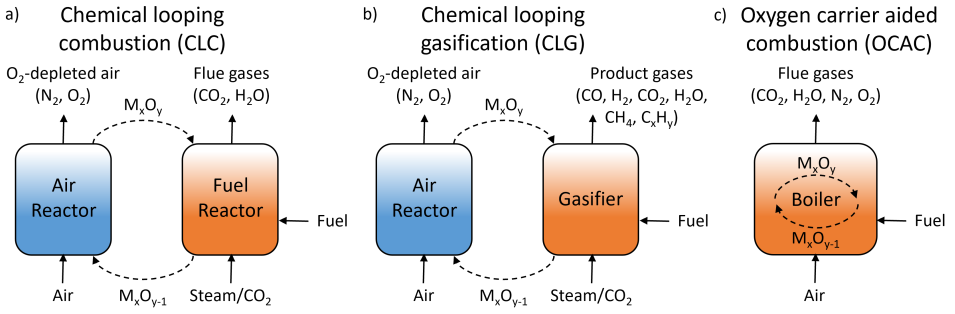

Figure 2.1: Schematic overview of three technologies that utilize oxygen carriers (M_xO_y): a) CLC, b) CLG and c) OCAC.

The use of oxygen carriers is not exclusively restricted to CLC. If the amount of oxygen transported from the AR to the FR is restricted, it will result in partial combustion of the fuel. While CLC aims for complete fuel conversion to form products of CO_2 and H_2O, partial combustion is used in another technology called chemical looping gasification (CLG). In CLG, the reducing reactor, into which fuel is being fed, is called a gasifier, see Figure 2.1b. The goal of partial fuel conversion in the CLG gasifier is to form products rich in *e.g.*, CH_4, CO and H_2, which is considered valuable fuel sources that can be used in other processes [45, 46].

Oxygen carriers can also be used as bed material in conventional fluidized bed boilers. The process is called oxygen carrier aided combustion (OCAC), schematically displayed in Figure 2.1c. The fuel conversion is restricted to one fluidized bed reactor, where the OC undergoes oxidation and reduction according to reactions 2.1 and 2.2 in oxygen-rich and fuel-rich parts of the boiler, respectively [35, 47–49]. The benefits of using a bed of OC in the OCAC technology over a bed of sand that is generally used in conventional fluidized bed boilers are increased combustion efficiency and more even temperature distribution within the bed. This enables an increased fuel load, reduced need of excess oxygen and overall lower formation of harmful NO_x and CO emissions [47]. The downside of using OCAC over CLC or CLG is that it does not facilitate inherent CO_2 separation. It might, however, be beneficial to implement OCAC on facilities equipped with post-combustion CO_2 capture as it results in lowered air-to-fuel ratios and thus higher CO_2 concentrations in the exhaust, which in turn lowers the cost for gas separation [50, 51].

2.1.1 Chemical looping with oxygen uncoupling

The process of thermally converting solid fuels involves several stages and reactions. The moisture content evaporates early during the heating process, before the fuel undergoes pyrolysis. The volatile matter will then react with the OC while the remaining fuel mainly consists of char and inorganic content. The rate of reactions between solid char and solid OC is usually low [52]. Therefore, the char which mainly consists of carbon or hydrocarbons, first needs to be gasified to form volatile products that can react with the OC. The char is generally gasified with CO2 or steam according to the endothermic reactions 2.3 and 2.4, respectively.

$$C + C_nH_m + (1+n)CO_2 \rightarrow 2(1+n)CO + \frac{m}{2}H_2 \tag{2.3}$$

$$C + C_nH_m + (1+n)H_2O \rightarrow (1+n)CO + (1+n+\frac{m}{2})H_2 \tag{2.4}$$

Gasifying the char is the most time-consuming step along the fuel conversion process. Although the gasification rate can be increased by increasing the operating temperature or by adding CO_2 or O_2, the char generally requires long residence times within the bed to attain full conversion [53, 54]. An alternative way to bypass the slow char gasification step is to employ OCs that releases gaseous oxygen under the appropriate thermodynamic conditions. The process is known as chemical looping with oxygen uncoupling (CLOU) and only applies to certain OC materials according to reaction 2.5 [54–56].

$$M_xO_y \rightarrow 2M_xO_{y-1} + O_2 \tag{2.5}$$

By using an OC with CLOU properties, the fuel char can react directly with the gaseous O_2 released by the OC, avoiding the need for preliminary gasification. Although OCs with CLOU properties are highly suitable for solid fuels, they have also demonstrated increased conversion rates for gaseous fuels [54].

2.2 Oxygen carriers

A crucial aspect of optimizing chemical looping processes is the choice of OC material. The decision is influenced by factors like fuel composition and conversion conditions. Key considerations encompass reactivity, chemical stability, toxicity, cost and availability [57]. The ideal OC should exhibit high reactivity with fuel and oxygen for efficient combustion, possess a high oxygen transfer capacity to minimize the required quantity and have favorable physical properties. This includes a high melting temperature to prevent sintering, robust mechanical strength to resist attrition and extend lifespan, and low agglomeration rates when combined with fuel. To be economically and environmentally feasible, the material should be cost-effective and devoid of toxic or hazardous components. Broadly, these materials generally fall into two categories: cost-efficient but less effective

options and high-performance synthetically manufactured materials, which tend to be more expensive [57]. The work presented here involves three different OC materials: calcium manganite, manganese oxide, and ilmenite. The OC materials were chosen for this thesis since they are currently considered state of the art in the CLC community. They are, however, highly suitable for other conversion applications as well [35, 58–60], and in the case for ilmenite, several successful operations in commercial applications has been reported [34, 35, 48, 49, 61].

2.2.1 Low-cost oxygen carriers

Among the low-cost materials with oxygen-carrying properties are naturally occurring minerals, such as ilmenite, manganese ore and iron ore, and byproducts from the industry, such as LD-slag [35, 62–64]. While these materials may be suboptimal for gaseous fuels due to their slow methane conversion rates, they exhibit better performance with solid biomass fuels due to their sufficient reaction rates towards CO and H_2 [65, 66]. Another reason is that the aggressive ashes in solid biomass result in harsh environments in the boiler, which is expected to lower the OC lifetime considerably. Since the costs for manufactured OC are likely to be at least one order of magnitude higher than those of minerals, leveraging low-cost OC materials emerges as the sole economically feasible option [58].

Arguably, the most scrutinized mineral-based OC material in recent years is ilmenite. This iron-titanium oxide mineral ($FeTiO_3$) possesses a high oxygen-carrying capacity, excellent chemical stability, and affordability, making it an attractive alternative for biomass conversion applications [34, 35, 49, 67]. While it is extensively utilized in industrial OCAC facilities, the material was also chosen as a model when designing a 1000 MW_{th} CLC plant [16, 48, 68]. Ilmenite is abundant in various geological deposits worldwide and it endures elevated temperatures and harsh conditions related to biomass conversion. The oxidation of natural ilmenite involves two key steps: (i) the conversion of Fe^{2+} to Fe^{3+} and (ii) the formation of phases enriched in both Fe and Ti [69]. The first phase, converting Fe^{2+} to Fe^{3+}, occurs initially through surface diffusion, followed by slower lattice diffusion. During the oxidation process, iron migrates out of the ilmenite structure, leading to the formation of a surface hematite (Fe_2O_3) layer and needle-like rutile (TiO_2) texture within the sample [70]. In the reduction of ilmenite, the Fe_2O_3-Fe_3O_4 transformation outpaces both the steps Fe_3O_4-FeO and FeO-Fe [71]. Therefore, the formation of surface hematite is vital to reach high fuel conversion and improve the oxygen-carrying abilities of ilmenite. The hematite layer grows during repeated redox cycles, which is typically referred to as ilmenite activation [72].Studies report that ilmenite exhibits a desired feature to adsorb potassium, which, over time, infiltrates the particles and reacts with titanium to form stable alkali-titanate compounds [34, 36, 73].

2.2.2 Manufactured oxygen carriers

Manufactured OC materials are generally unsuitable for solid fuels due to their considerable cost. However, their use can be justified in the relatively harmless combustion environment of gaseous fuels due to their high conversion efficiency towards methane. An array of materials has been studied for manufactured OC materials including metal oxides, mixed metal oxides, and perovskite-type compounds. Common active phases often incorporate elements like Ni, Cu, Mn or Fe. To bolster their structural integrity, these compounds are often anchored to an inert material, such as zirconia (ZrO_2) or alumina (Al_2O_3) [74–76]. Although Ni-based materials have shown excellent reactivity, their toxicity coupled with their high cost diminishes their appeal [77]. Similarly, Cu-based materials have shown promise, *e.g.*, by their CLOU properties, but they come with a high price and a significant risk of agglomeration at high temperatures [66, 77].

In contrast, Mn-based materials offer a cost-effective option with compelling CLOU properties. They also exhibit high thermal stability and regenerative ability over the multiple redox cycles related to continuous CLC operation [74]. Since the two most oxidized forms of manganese (MnO_2 and Mn_2O_3) decompose in air at temperatures around 516 and 820 °C, respectively, they are not likely to be present in CLC (generally operating around 950 °C) [14, 74]. Instead, the most likely forms of manganese oxides present in a high temperature CLC application are Mn_3O_4 and MnO [74]. The thermodynamic properties of manganese oxide allow for recurring oxidation and reduction in conditions relevant for thermal conversion applications [62]. However, the kinetics for re-oxidation can be slow for Mn-based materials, promoting their amalgamation with other elements like Ca, Mg, Fe or Ti [78].

Other materials that have shown promise for CLC due to their CLOU properties are different combinations of calcium manganite. Such materials have been successfully used in CLC with gaseous fuels [79, 80], and in a 100 kW CLC unit operated with solid biomass fuel [41]. The materials have demonstrated excellent performance, achieving high fuel conversion rates [80] and exhibiting a prolonged operational lifetime [81]. Calcium manganite ($CaMnO_{3-\delta}$) is perovskite-type materials where additional elements can be included in the perovskite structure (*e.g.*, Ti) or occur in a separate phase (*e.g.*, Mg) [82, 83]. The degree of oxygen deficiency is described by the δ-factor, and equals zero for a perfect perovskite structure [84]. The δ-factor depend on the surrounding oxygen fugacity and the difference in δ for the AR and FR determines the how much oxygen will be available for oxidation according to reaction 2.6 [78].

$$ABO_{3-\delta_{AR}} \leftrightarrow ABO_{3-\delta_{FR}} + 1/2(\delta_{FR} - \delta_{AR})O_2 \tag{2.6}$$

Since the OC can be produced from low-cost materials that are not associated with health or safety issues, and it has not shown signs of agglomeration, its implementation can be justified over *e.g.*, Ni or Cu-based materials [41, 82].

2.3 Alkali release during biomass conversion

Solid fuels always contain a certain concentration of inorganic species that can be classified based on their volatility. The inorganic content of biomass can range from <1 wt% to 40 wt%, depending on the fuel source [28], with non-volatile elements like Ca, Mg, Si, Al and Fe, volatile elements including K, Na, Cl and S [20, 85]. However, the behavior of an element in biomass ashes is not solely dictated by its inherent volatility. For example, the fate of potassium is determined by the presence of other elements, resulting in non-volatile K-silicates in the presence of Si and volatile KCl when Cl is available. Biomass ashes are generally categorized into bottom ash and fly ash. The first primarily compose of non-volatile species that remain after fuel conversion and accumulates in the beds [20]. The volatile compounds either condense onto cooler surfaces, such as non-volatile ash or heat transfer surfaces, or they nucleate to form aerosol particles when the flue gas temperature drops. Therefore, the fly ash generally appears in flue gases as aerosol particles or fragments of bottom ash particles [20]. The size of the aerosol particles depends on the volatile compound concentration in the gas, and these particles grow due to the continued condensation of volatile compounds or through coagulation and agglomeration of aerosol particles [86].

Some of the more challenging ash species associated with biomass conversion are the alkali metals, sodium and potassium. The concentration of K and Na differs significantly with several orders of magnitude between different fuel sources. High concentrations are usually found in fast-growing crops like straw, with typical K concentrations between 11 – 28 g kg^{-1} dry fuel and Na concentrations between 0.15 – 1 g kg^{-1} dry fuel [87]. In contrast, slow-growing biomass contains lower amounts of alkali metals, with concentrations around 0.7 g K and 0.06 g Na for one kilogram of dry pine wood [87]. The alkali can either be integrated into the organic structure or reside in the inorganic matrix [88]. Consequently, the alkali is released at two different temperatures during the conversion process. The first release takes place below 700 °C, where organically-associated alkali is released during the devolatilization process [89–91]. A majority of the alkali is still intact after the devolatilization, retained in the remaining char in the form of different salts, like chlorides, carbonates, sulphates or silicates [89, 90, 92]. At higher temperatures, when the char is oxidized or gasified, the alkali can either transition to the gas phase or remain in the condensed form. KCl is a primary gaseous release species when Cl is readily available, while K-silicates can remain in condensed form up to 1200 °C [89]. Regardless if the alkali is present in gaseous or condensed form, in either bottom ashes or fly ashes, they significantly impacts the conversion system.

2.3.1 Agglomeration

Alkali retained in bottom ash of a FBC process can adversely affect both the fluidized bed material and the fuel conversion process, leading to agglomeration through various

mechanisms. Some ashes can form phases with low melting temperature, like K-Ca-P, which can coat the particle surface and cause agglomeration. [20, 93]. Another example is K-Si melts that can deposit onto bed particles and induce agglomeration [28]. These types of ashes will interact with all types of bed materials, both oxygen carrying and inert materials such as silica sand. However, alkali often forms volatile compounds, like KCl(g) or KOH(g), that can react with silica-containing bed materials and form glassy K-Si products with low melting temperatures that cause agglomeration [27–29, 94].

Agglomeration should be avoided since it may lead to defluidization. Strategies to mitigate bed agglomeration includes continuous bed material replacement, lowering combustion temperatures below the agglomerate melting points, or by using alternative bed materials that adsorbs alkali without causing agglomeration [95, 96]. Since the first two options comes with a cost penalty, the third option is often more compelling. Besides common bed materials like olivine, dolomite and feldspar, one material that can adsorb alkali without causing agglomeration is ilmenite [34, 36]. Studies show that potassium migrates into the ilmenite over time, to form stable products of alkali-titanates, with a higher melting temperature than potassium-silicatess [34, 67, 97].

2.3.2 Catalytic activity

The catalytic properties of alkali can offer advantages in FBC if agglomaration is avoided. For instance, the presence of potassium has shown catalytic effects on tar cracking, which is important to reach a high-quality product gas in biomass gasification [21, 22]. Since tar removal in the hot gas stream is costly, it is more favorable to achieve primary tar reduction within the fluidized bed. Active bed materials like ilmenite and olivine have been found to reduce tar [60, 98], and the gradual formation of ash layers on particle surfaces may further enhance tar conversion [98–101].

In addition, the presence of alkali has several advantages for fuel conversion [22, 23, 102]. Increasing the K content of biomass has been demonstrated to enhance gasification reactivity [103, 104], and a high K/C ratios in the fuel or introduction of supplementary K lead to increased gasification rates [25, 26]. A recent review article summarized the catalytic effects of various alkali compounds on biomass pyrolysis, with sodium compounds being less potent than potassium but more common and cost-effective [87]. It was also noted that alkali additives lower the decomposition temperature of cellulose pyrolysis, with potassium showing a stronger influence on levoglucosan and hydrocarbon yields compared to sodium [105–107].

2.3.3 High temperature corrosion

Gaseous alkali emissions can lead to severe issues like fouling and corrosion in heat exchangers [32, 41, 108], interference with gas reforming equipment [33] and affect down-

stream equipment such as fuel cells, catalysts, and turbines [109, 110]. These gaseous alkali compounds can nucleate into aerosol particles or condense on cold surfaces. Steam superheaters, which extract heat from the flue gas stream of a fluidized bed boiler, are particularly susceptible to alkali condensation due to their lower operating temperatures compared to the combustion bed (400 – 600 °C versus 800 – 900 °C) [28]. Alkali is typically released as chlorides, hydroxides, or in atomic form (K and Na) depending on the fuel source [85, 89, 90], with alkali chlorides being the primary culprits in high-temperature corrosion (HTC) [20, 111–115]. Alkali condensation creates a sticky surface that attracts further alkali deposition from impaction of alkali aerosols or fly ash particles, leading to heat exchanger insulation and thus decreased heat transfer efficiency and reduced thermal efficiency of the boiler.

Mitigating fouling and corrosion can involve the use of soot-blowers to mechanically remove ash deposits from superheaters during boiler operation, although this is costly. Lowering the superheater steam temperature can also mitigate HTC in biomass combustion but at the expense of decreased power generation efficiency [116]. Another approach is to introduce sulfur into the fluidized bed to inhibit the formation of aggressive alkali chlorides, favoring the formation of less corrosive alkali sulfates [20, 117, 118]. Adding sulfur, whether in elemental form or through sulfur-containing fuel co-firing, allows for higher superheater temperatures and increased energy output from the boiler [119]. Using alkali adsorbing bed materials, such as ilmenite, may also reduce the gaseous alkali emissions [34, 49, 67].

Conclusively, alkali metals and their release characteristics have a major role in thermochemical conversion of biomass. In addition, most of the alkali-related studies available in the literature are based on off-line characterization of material from industrial processes and related to solid-solid interactions between ash and OC [34–36]. These studies may not explain the interactions between gaseous alkali compounds and solid OC under conditions within the fuel conversion process. Therefore, reliable and adequate alkali monitoring methods are needed to gain further knowledge regarding the faith of alkali in thermal conversion applications and to develop more efficient and reliable biomass conversion technologies with reduced environmental impacts.

2.4 Alkali monitoring techniques

Several measurement techniques have been applied to characterize alkali in combustion related research. The different methods can be divided into two groups: offline and online methods. Offline techniques necessitate samples extracted from the process, which are subsequently analyzed using various material analysis techniques. Notable among these are scanning electron microscopy (SEM), frequently paired with energy dispersive spectroscopy (EDS) [34, 36, 120], X-ray diffraction (XRD) [29, 121], X-ray photoelectron spectroscopy (XPS) [35] and X-ray microtomography (XMT) [120]. Although offline methods may have a limited time resolution, they provide valuable information about the distribution and concentration of alkali within samples. It is noteworthy, however, that offline methods

often study samples that have experienced ambient conditions, analyzing their final state. The results can be obscured if properties change during the sampling procedure.

Online measurement techniques offer real-time insights to alkali chemistry within the operational environment [122].Generally, the techniques are based on two approaches: continuous extraction of sample gas for subsequent analysis or in-situ measurements. In-situ techniques usually employ optical diagnostic methods, such as laser-induced fluorescence [123–125] or absorption spectroscopy [126–128]. Although providing detailed molecular data from within the combustion process, the measurements are often affected by the harsh conditions within the combustion facilities or the optical density in the sample flow [129]. Extractive gas sampling techniques, on the other hand, commonly utilize various ionization approaches, such as mass spectrometry [130–132] or plasma techniques [133].

An alternative approach, blending cost-effectiveness with adaptability for online alkali monitoring, is based on the principle of surface ionization (SI). The employed instrument is termed a surface ionization detector (SID), and it has high selectivity and sensitivity to sodium and potassium compounds and offer robust measurements with a high time resolution. The device has been used extensively in combustion-related studies ranging from commercial [134], to pilot [41, 42, 73] and laboratory-scale [108, 135, 136] reactor systems. Its versatility is evident, given its utility in assessing alkali emissions across a wide range of conversion applications, including gasification [134, 137–139], CLC [41, 42, 73] and OCAC [42]. While studies have provided valuable information about alkali emissions in various applications and from various fuel sources, one limitation is that the device cannot discriminate between potassium and sodium compounds. A SID was used for online alkali monitoring in this work, where additional method development was performed with the aim to speciate different alkali compounds. The ability to specify the alkali compounds is a highly desirable feature since potassium and sodium often coexist in biomass, where potassium compounds may have stronger catalytic effects over sodium, while simultaneously being more corrosive. In addition, the corrosion is more severe for alkali chlorides compared to alkali sulfates.

3

Materials and methods

The work presented in this thesis investigates alkali interactions with different OC materials by measuring the alkali concentration in the exhaust from different reactors. The experiments are carried out during *i*) continuous alkali gas injection to fluidized beds of unused OC particles, and *ii*) alkali release from alkali-containing OC particles that have been used for biomass combustion. The studies utilize two different fluidized bed batch reactors and a thermogravimetric analyzer (TGA) unit. Additional experiments involve designing and developing novel reactor systems, the alkali measurement system (i.e., the SID), and the method of using a SID in combination with a TGA. This section of the thesis presents the OC materials and reactor systems.

3.1 Oxygen carriers

Three different OC materials were used in the presented work: calcium manganate, manganese oxide and ilmenite. The first two are synthetically manufactured materials and the latter is a natural ore. All materials had a particle size distribution in the range 90 – 250 μm.

The calcium manganate, with molar composition $CaMn_{0.775}Ti_{0.125}Mg_{0.1}O_{3-\delta}$, was manufactured with a spray-drying technique by the Flemish Institute for Technological Research (VITO, Belgium). It is a perovskite-type material where Ca, Mn and Ti are incorporated in the perovskite structure while Mg is present as a separate phase [83]. The same batch of material has been used previously in a 10 kW CLC study with gaseous fuels [83], where it is assumed to not have been in contact with alkali or other ash components.

The manganese oxide, consisting of 40 wt.% Mn_3O_4 and 60 wt.% Mg-ZrO_2, was manufactured by Johansson et al. using a freeze granulation method [75]. While manganese oxide presents the active OC-phase the magnesium stabilized zirconia acts as an inert support material [75]. The support material improves the particle integrity while also increasing the material porosity, which results in a larger surface area for reaction. The material has been used in different CLC systems previously, where it was proven to be a successful OC material [74, 75].

The ilmenite, consisting of Norwegian rock ilmenite with molar composition $FeTiO_3$ was provided by Titania A/S. The material comprises mostly of Fe and Ti while low levels of Si, Mg and other elements/components are also present. The batch of material used in **Papers III** and **IV** had been used as OC during OCAC of biomass in a 115 MW_{th} CFB boiler in Örtofta, Sweden [48, 49]. The material composition of both the OCAC ilmenite and unused ilmenite can be seen in Table 3.1.

Table 3.1: Composition of reference ilmenite provided by the supplier Titania A/S and ilmenite extracted after 225 h of OCAC operation in the Örtofta power plant.

Papers: wt% dry	**III** and **IV** *OCAC ilmenite*	**III**, **IV** and **VII** *Unused ilmenite*
Fe	19.0	33.3
Ti	16.0	23.9
Si	4.8	0.9
Ca	10.8	0.3
Mg	2.0	1.8
Al	1.5	0.3
Na	1.0	0.1
K	1.8	0.1
Mn	0.6	0.1

3.2 Fluidized bed reactors

Two different batch reactors on laboratory-scale were used to study alkali-OC interactions. One of the reactors, called **Reactor I**, consisted of stainless steel alloy 304 and shaped like a 915 mm long vertical tube with 26 mm inner diameter, as illustrated in Figure 3.1a. The central part of the reactor was externally heated by a 600 mm tall furnace. A perforated plate, of stainless steel alloy 316, was used as a combined particle filter and gas distributor plate. A thermocouple was placed on the flange to measure the reactor temperature.

A significant problem with **Reactor I** is extended hot regions above and below the fluidized bed where alkali interacts with the hot reactor walls, influencing alkali-OC interactions. A novel fluidized bed reactor was designed, based on the knowledge gained from experiments in the first reactor and fundamental understanding of alkali processes at high temperatures. This reactor, called **Reactor II** in Figure 3.1b, consist of corrosion-resistant Kanthal APMT™ steel material and is significantly shorter than the previous, with a shorter heated section and different geometries of the inlet and outlet sections.

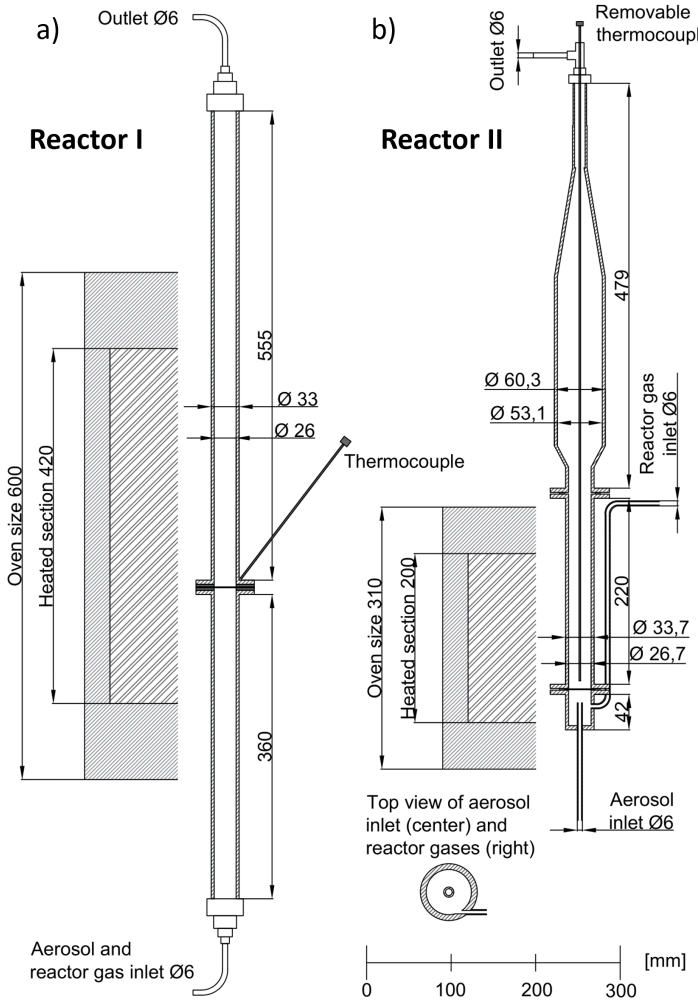

Figure 3.1: Schematic overview of the fluidized bed batch reactors (dimensions in mm).

3.3 Fluidized bed experiments

The experimental setup for the fluidized bed experiments was similar for both reactors and is schematically illustrated in Figure 3.2. The reactors are placed in electrically heated furnaces where the temperature is adjusted based on temperature measurements on the lower flanges. A flow of inert, reducing or oxidizing reactor gas, controlled by an

automated valve system, is mixed with a flow of alkali aerosol particles suspended in nitrogen. The alkali aerosol particles rapidly evaporate to their molecular constituents at temperatures above 500 °C. The mixture of gaseous alkali and environmental reactor gas passes through the perforated plate into the bed of OC particles with superficial gas velocities that are high enough to fluidize the bed. Proper bed fluidization is ensured by monitoring the differential pressure and its fluctuations over the bed. This is achieved by online pressure measurements in the inlet and outlet. The gas leaving the reactor is led to different instruments for online monitoring of the gas concentrations, sub-micron particle concentrations and alkali concentrations.

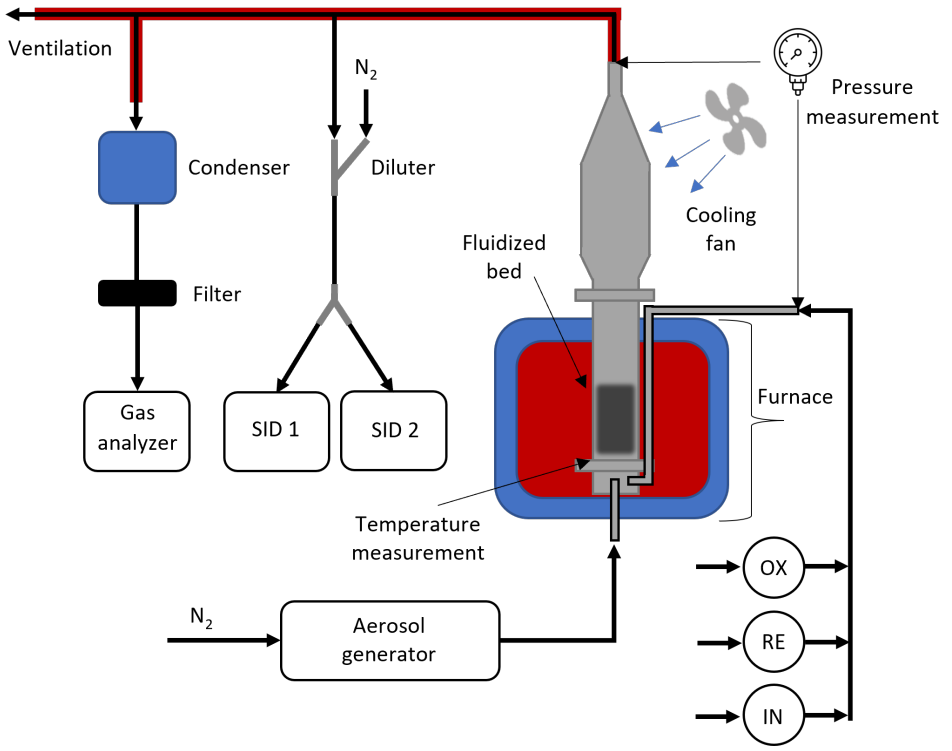

Figure 3.2: Schematic illustration of the experimental setup for the fluidized bed reactor experiments. The schematic illustrates **Reactor II**. Adapted from **Paper VII**.

The experimental parameters for the different measurement campaigns are listed in Table 3.2. The table includes operating temperatures, the fluidized bed composition and inventory, alkali compounds and loading and the type of measurement equipment being used in the studies. All fluidized bed experiments with OC particles are conducted at temperatures between 800 and 900 °C. Additional experiments are carried out with empty reactors at temperatures between room temperature and 900 °C.

Table 3.2: Experimental parameters used for the fluidized bed experiments in the different experimental campaigns.

	Paper I	Paper II	Paper V	Paper VII
Reactor	I	I	II	II
Temperature (°C)	25 – 900	800, 850, 900	25 – 900	900
OC amount (g)	0	0, 20	0, 5, 10, 20	0, 40
OC material	-	Calcium manganate	Calcium manganate	Calcium manganate, Manganese oxide, Ilmenite
Alkali compound	KCl	KCl	KOH, KCl	KCl, KOH, K_2SO_4, NaCl, NaOH, Na_2SO_4
Alkali loading (mg m^{-3})	0, 6, 12	6, 12	5.4	20 – 40
Alkali flow (L min^{-1})	2	2	1	1
Reactor gas flow (L min^{-1})	0.3	0.3	0.3	0.5
Cooling fan	No	No	Yes	Yes
Exhaust gas measurements	Particles, Gas, Alkali (1 SID)	Gas, Alkali (1 SID)	Gas, Alkali (1 SID)	Gas, Alkali (2 SIDs)
Heating of exhaust lines	No	No	No	Yes

To resemble the different conditions of a CLC process, the environmental reactor gas consisted of either pure N_2, synthetic air (21% O_2 in N_2) or synthetic fuel gas (50% H_2 in CO), resulting in inert, oxidizing or reducing gas conditions, respectively. Instead of having the OC circulate between the oxidizing AR and reducing FR of a CLC process, this work uses a single reactor where the inlet reactor gases are shifting between oxidizing and reducing conditions. Inert conditions are applied between the reducing and oxidizing conditions for safety reasons as well as to resemble transport through the inert loop-seals of a CLC process. These redox cycles were typically repeated several times per experiment.

Exhaust gas is led through a nitrogen diluter before being fed to the instruments for particle and alkali measurements, and through a cooler and particle filter to a gas analyzer. The excess gas flow is discarded to ventilation. The alkali concentration is measured online with a SID. A single SID is used in **Papers I**, **II** and **V**, which report the total alkali concentration in the sample gas with a time resolution of 1 s. The experiments in Paper VII also uses that SID, but with the addition of an extra SID that is being operated differently, providing information about the composition of the alkali compounds leaving the reactor. The SID is described in further detail in Section 4.2. The instrument to measure sub-micron particles is a scanning mobility particle sizer (SMPS), which measured particles in the range between 16 and 770 nm. A gas analyzer was used to measure the concentrations of CO, CO_2, H_2, CH_4 and O_2.

3.4 Thermogravitertic analyzer experiments

A TGA system was also employed for studying alkali release from used OC particles. Here, alkali was measured in the exhaust while the OC was subjected to inert or oxidizing conditions at high temperatures. The configuration comprises a SID connected to the exhaust of a commercial TGA, schematically illustrated in Figure 3.3. This setup allows for real-time monitoring of the sample mass while measuring the alkali release from the sample. The TGA was operated with a constant stream of N_2 balance gas, accompanied by either inert (N_2) or oxidizing (synthetic air) purging gas. Samples between 0.5 – 20 mg of OC material were loaded on a sample holder of platinum and subjected to a temperature ramp until reaching 1000 °C, where they were maintained at a constant temperature.

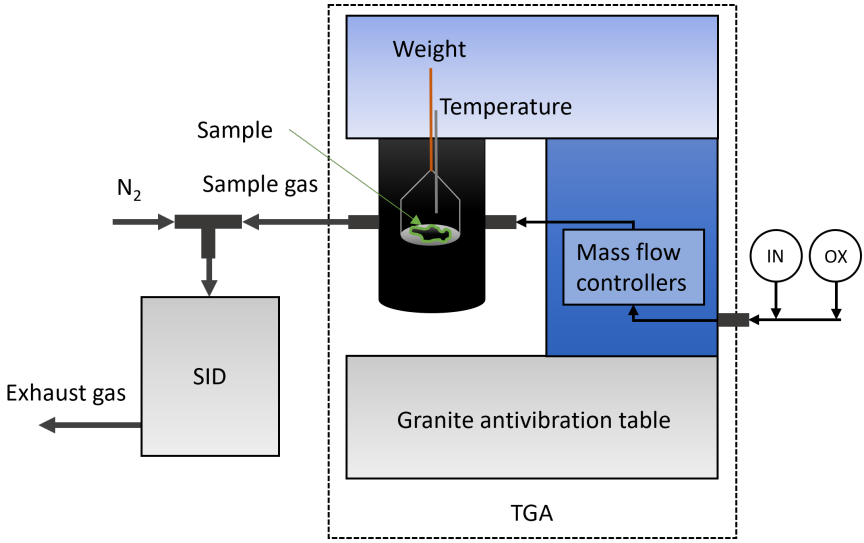

Figure 3.3: Experimental setup of the SID and TGA (Model Q500; TA instruments) used for detecting alkali desorption from a sample, adapted from **Paper IV**.

Alkali compounds released from the sample are transported with the exhaust gases leaving the TGA and diluted with N2 before entering the SID. Alkali losses between the sample and the SID, due to molecular diffusion in the hot TGA compartment and aerosol particle losses in the sampling lines, are presented and discussed in the results section.

4

Experimental techniques for alkali studies

The following subsections present the experimental techniques used during the alkali studies presented in this thesis. These include generation, online monitoring and characterization of different alkali compounds, as well as general calibration procedures and material analyses.

4.1 Alkali aerosol generation

All alkali-related studies presented in this thesis rely on a stable and controllable alkali dosing system. A method that has been proven successful in previous studies is to introduce alkali in the form of sub-micron particles suspended in a gas [33, 129, 140]. The particles in this work are generated by an aerosol particle atomizer, by atomizing a solution of alkali salt dissolved in ultrapure water with pressurized nitrogen gas (see illustration in Figure 4.1). The alkali solution is atomized by expansion through a critical orifice, forming polydisperse alkali droplets suspended in nitrogen. The droplets are dried in an open path diffusion dryer [141]. The mass concentration of alkali particles is proportional to the particle size, which is controlled by changing the concentration of the liquid solution.

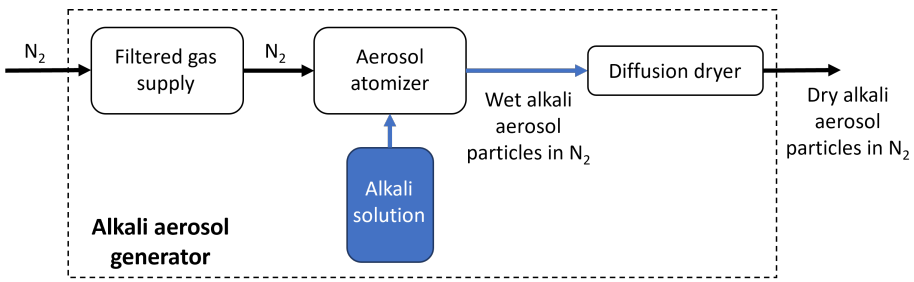

Figure 4.1: Schematic illustration of the alkali aerosol generator.

4.2 Surface ionization detector (SID)

The method of SI has been used for alkali measurements over the past decades [129, 142–144]. The concept is based on the natural phenomenon where atoms thermally desorb from a metal surface in ionic form [143, 144]. The degree of ionization (α) can be obtained by the Saha-Langmuir Eq. 4.1, and described as the ratio between the number of positive ions (n_+) and neutral atoms (n_0) leaving a surface area per time unit [129, 145],

$$\alpha = \frac{n_+}{n_0} = \frac{g_+(1-r_+)}{g_0(1-r_0)} exp\left[\frac{e(\phi - IP)}{k_B T}\right] \tag{4.1}$$

where the statistical sum ratio g_+/g_0 between ions and neutral atoms equals 0.5 for alkali metals and the reflection coefficients r_+ and r_0 are close to zero [129]. The $e\phi$ is the surface work function, eIP is the ionization potential of the desorbing species, k_B is Boltzmann's constant and T is the surface temperature. For most atoms and molecules, the surface work function is smaller than the ionization potential ($\phi < IP$), which favors desorption of neutral species and ion desorption can safely be ignored [135]. However, the opposite is true for alkali metals, *i.e.*, $\phi > IP$, which strongly favors emission of ions. The probability of ionization (β) described by Eq. 4.2, is typically > 99% and 89% for K and Na, respectively, on a platinum surface at 1500 K [146].

$$\beta = \frac{\alpha}{\alpha + 1} \tag{4.2}$$

Other alkali metals, such as Rb, Cs and Li, also have a high ionization probability [146], but are usually less abundant and therefore ignored in biomass conversion studies. Alkaline earth elements can also desorb in ionic form, but their binding energy to a platinum surface is substantially higher than for alkali atoms and their desorption rates are negligible below 1500 K [147]. As a consequence of the criteria above, the SI method has a high selectivity and sensitivity for K and Na compared to other atoms and molecules, which makes it ideal for alkali detection in biomass conversion processes.

The SI technique has been used to measure alkali in various instruments, such as aerosol mass spectrometers [148, 149] and in SIDs. The SID is a portable instrument that can be assembled from low-cost equipment to measure the concentration of alkali in a gas flow. It consists of a 70 mm high cylindrical measurement cell with 70 mm diameter. The main components are schematically shown in Figure 4.2.They include a resistively heated platinum filament (red coil in Figure 4.2) and a closely situated metal ion collector plate (blue plate in Figure 4.2). When an alkali-containing gas flow enters the SID compartment, a fraction of the alkali will evaporate and dissociate on the hot filament before subsequently desorbing as alkali ions. The filament is operated at a positive potential, forcing the positively charged alkali ions to diffuse to a grounded collector plate where they induce a current. The current is amplified and measured with a signal intensity proportional to the mass concentration of alkali in the sample gas [135, 143].

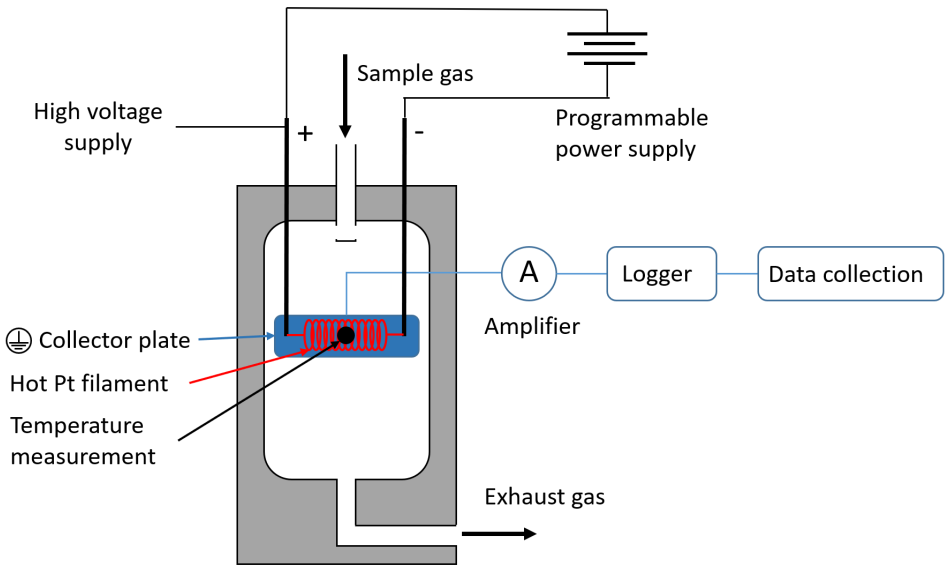

Figure 4.2: Schematic overview of the SID including the hot platinum filament (red) and ion collector plate (blue). Adapted from **Paper VI**.

4.3 Temperature modulated surface ionization (TMSI)

Previous studies using the SID report the total alkali concentration (K and Na), without further discrimination [41, 42, 73, 134, 137, 138, 150]. However, discrimination between sodium and potassium compounds may be possible based on differences in their aerosol evaporation characteristics as a function of temperature combined with the desorption kinetics of alkali from the hot platinum filament. A novel method based on temperature modulated surface ionization (TMSI) was developed for online speciation of alkali compounds. The method is based on rapid shifts between two or more filament temperatures while monitoring the produced alkali ion current, and the theory is shortly described in the following section.

In general, sodium atoms bind more strongly to platinum surfaces compared to potassium, which consequently result in lower desorption rate coefficients in comparison. Therefore, the concentration of sodium will generally be higher compared to potassium at the platinum surface for a given temperature and incident alkali flux. In addition, the influence of temperature on the desorption rate coefficient can be described by the Arrhenius Eq. 4.3, where lower temperatures result in decreased desorption rate coefficients. Therefore, lowering the filament temperature will result in a higher concentration of adsorbed alkali if the alkali flux to the surface remains constant.

The time-dependent alkali surface concentration, $c_s(t)$, at temperature T can be described by Eq. 4.4 [129], where F is the incident flux of alkali atoms to the surface and k_+ and k_0 are the ionic and neutral alkali desorption rate coefficients.

$$k(T) = Aexp(\frac{E_a}{k_B T}) \tag{4.3}$$

$$\frac{dc_s(t,T)}{dt} = F - (k_+(T) + k_0(T))c_s(t,T) \tag{4.4}$$

The differential Eq. 4.4 is solved numerically to mimic the typical time required to switch between filament temperatures, where the desorption rate coefficient, *k(T)*, is described by the Arrhenius Eq. 4.3.

Figure 4.3 display the calculated flux of sodium and potassium from platinum at 570 and 1118 °C surface temperatures. When the surface temperature initially drops towards 570 °C, potassium and sodium fluxes rapidly decrease, reaching a minimum after about 10 seconds, before gradually recovering within the first 60 seconds. The sodium flux is significantly lower than that of potassium, due to the higher activation energy required for sodium desorption. When the temperature is raised back to 1118 °C, the emitted potassium and sodium fluxes peaks before they stabilize at a similar constant level for both systems. These peaks result from the accumulation of surface coverage during the preceding low-temperature period. The potassium peak precedes the sodium peak during the temperature increase, indicating a lower stability of the K-Pt system compared to the Na-Pt system.

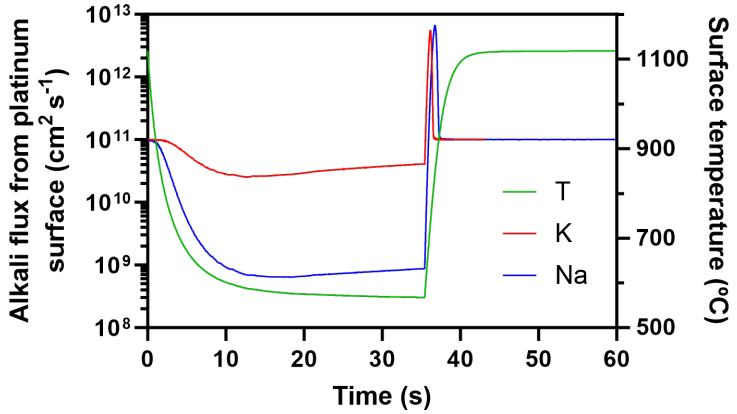

Figure 4.3: Calculated flux of sodium (blue line) and potassium (red line) from a hot platinum filament as a function time. The filament temperature (green line) was shifted between 570 and 1118 °C at 0 and 60 s, assuming a constant flux of alkali to the surface of $1 \cdot 10^{11}$ s^{-1} while ignoring desorption of neutral alkali atoms, k_0. Adapted from **Paper VI**.

A qualitative comparison of the displayed results indicates that a method to distinguish between Na and K may be based on the observed signal levels reached at each temperature, or on the transient signals observed when changing temperature. The description assumes that alkali compounds enter a SID in molecular form. However, in recent applications where the SID is used to monitor alkali from combustion or gasification processes, the alkali has been in the form of submicron particles suspended in the sample gas [41, 134, 139, 150, 151]. This introduces complexity but offers an opportunity to distinguish between various types of alkali salts. The typical temperature used in the TMSI method, 1100 °C, exceeds the temperature at which sub-micron alkali salt particles rapidly evaporate [140]. Consequently, in the vicinity of the hot filament, the aerosol evaporates and may either impact the filament as molecules or leave the SID with the exhaust. The specific behavior depends on the physical properties of the alkali salt particles, particularly their evaporation rates as a function of temperature. For example, aerosol particles of KCl and K_2SO_4 rapidly evaporate at temperatures exceeding 500 °C and 800 °C, respectively, (see Section 5.2.2 below) leading to markedly different behavior near the hot filament.

Based on the considerations above, a method of temperature-modulation of the platinum filament was developed to speciate the alkali compounds in a sample gas. This is achieved by injecting a controlled flow of alkali aerosol particles of KCl, KOH, K_2CO_3, K_2SO_4, NaCl, NaOH, Na_2CO_3 or Na_2SO_4 into the SID during periodic shifts in platinum filament temperature, while measuring the produced ion current. The filament temperature was generally shifted between 550 – 1100 – 800 and 1100 °C, with a time duration of 30 s at each temperature. The signal intensity for each type of alkali salt display a unique dependence on filament temperature. Therefore, the alkali signal obtained with the TMSI method in reactor experiments could be described by a linear combination of the signals for pure salts. This enabled speciation of the alkali emissions from reactor experiments.

4.4 Aerosol particle measurements and SID calibration

A SMPS was used to measure the aerosol size number distributions in several experiments in this work. The SMPS unit reports the number of particles of with a specific size within a wider size distribution. In this work, a complete scan of aerosol particles in the size range 16 – 770 nm is reported every 120 s. By assuming the particles are spherical with a defined particle density, the SMPS can report the mass concentration of particles within that size distribution.

The SMPS was used to calibrate the SID signal, which is essential for all experiments in this work. The SID calibration procedure is explained in detail in Paper III. Basically, aerosol particles of different alkali compounds are generated by the aerosol generator and fed to the SID and SMPS in parallel. When the alkali aerosol particles enters the SID, they give rise to an ion current (generally reported in nA) while the SMPS provides an aerosol mass concentration. By gradually adjusting the aerosol concentration, a SID calibration curve can be generated. The calibration curve for a flow of KCl aerosol particles suspended

in nitrogen is shown in Figure 4.4. As indicated by the calibration tests, a linear relation is observed between the SID signal and the alkali particle concentration of the sample gas.

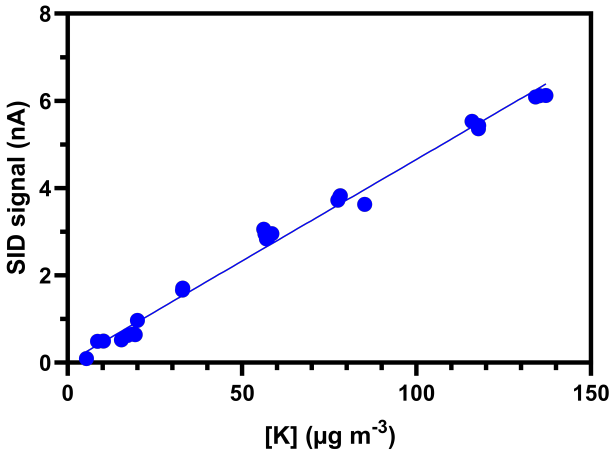

Figure 4.4: The SID signal as a function of mass concentration of K ($\mu g \cdot m^{-3}$) based on SMPS measurements from a flow of KCl aerosol particles. Adapted from **Paper III**.

4.5 Material analyses

Scanning electron microscopy with energy dispersive X-ray spectroscopy (SEM-EDS) was used for complementary chemical analysis of different OC materials and the wall material of the fluidized bed **Reactor I**. The material used to determine the composition of **Reactor I** was obtained by grinding from parts of the reactor which had not experienced high temperatures. The composition was in accordance with that of stainless steel alloy 304 [152]. For the OC particles, the morphology and elemental composition of the particle surface were studied by placing particles onto carbon tape. To study the particle cross-section, samples were prepared by molding in epoxy before being polished in several steps to obtain a flat and even surface. The SEM-EDS analysis was performed by first investigating a large area to observe trends and then gradually increasing the magnification to study individual particles. In **Paper II**, samples of calcium manganite OC were analyzed before and after being used in the alkali fluidized bed experiments. In **Paper IV**, the SEM-EDS analysis was performed on ilmenite as received from the OCAC power plant and on ilmenite samples after TGA experiments in inert and oxidizing atmospheres.

5

Results and Discussion

A major part of the work in this thesis involves developing new methods and reactor systems to investigate alkali processes in conditions relevant to thermal conversion of biomass. Therefore, this section begins by describing the development of the novel TMSI method which characterizes alkali compounds in a sample gas. The subsequent section describes the challenges in conducting detailed alkali studies at high temperatures in a typical laboratory reactor, including transmission and evaporation of alkali aerosol particles and molecular diffusion and penetration of gaseous alkali species. Thereafter, the development of a novel fluidized bed reactor optimized for studying interactions between gaseous alkali and fluidized OC particles is presented. Results from studies using the new reactor to characterize the uptake of different alkali compounds by various OC materials under CLC conditions are thereafter presented. Further studies investigated the alkali release from OC particles previously used for OCAC of biomass. The latter study was enabled after developing a new method to study alkali release and mass loss from fixed bed samples, including solid biomass. The chapter is then concluded by discussing the relevance of the discoveries to industrial applications.

5.1 Alkali salt speciation

The SID has been used to measure alkali concentrations in several combustion and gasification applications [41, 42, 73, 134, 137–139, 150] where the total alkali concentrations are reported without further speciation. The results presented here, and in **Paper VI**, demonstrate a new way of operating the SID that enables alkali speciation based on differences in aerosol evaporation as a function of temperature for different alkali salts, combined with the desorption kinetics of alkali from the hot platinum filament.

5.1.1 Changes in alkali intensity with filament temperature

Initially, the dependence of the detected SID signal on the filament temperature for different alkali compounds was investigated in a wide temperature range. The filament temperature was periodically changed between low temperature and 1100 °C.

Figure 5.1 shows the measured ion current as a function of time during constant injection of KCl aerosol. The alteration in filament temperature exerts a significant influence on the observed ion current, resulting in systematic variations as the lower temperature is increased in steps. Gradually increasing the lower filament temperature from 450 to 1000 °C leads to a rise in the signal intensity. A peak in the alkali signal appears when the temperature is rapidly increased from low temperatures to 1100 °C. The size of the peak steadily diminishes with increasing temperatures and is not observable when the low filament temperatures exceeds 800 °C. This indicates that alkali accumulates on the filament surface at low temperatures before being released, generating a transient peak in alkali desorption upon rapid temperature increase. This observed behavior is qualitatively consistent with the results from the simplified model presented in Figure 4.3.

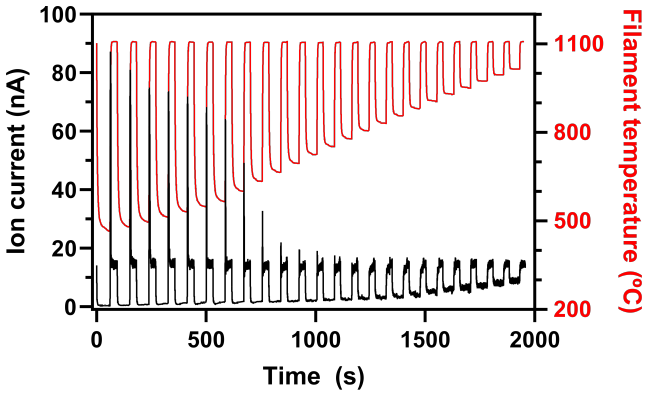

Figure 5.1: Ion current (black) measured by the SID during a constant influx of KCl aerosol particles and periodic shifts in filament temperature (red). Adapted from **Paper VI**.

Similar experiments as shown in Figure 5.1 were also conducted with NaCl, KOH, NaOH, K_2CO_3, Na_2CO_3, K_2SO_4 and Na_2SO_4. SSteady state alkali signal intensities at each temperature step were calculated for each salt, and the results are summarized in Figure 5.2. Significantly higher signal intensities are observed for potassium compounds at low temperatures compared to sodium compounds. At 550 °C, the signal intensity for potassium chloride, hydroxide and carbonate is around 1.5 nA, while the corresponding for sodium salts is around 0.05 nA. Alkali sulfates generally produce low signals compared to other salts, as seen previously [129], although the trend remains valid where the signal for K_2SO_4 is 0.2 nA and the corresponding for Na_2SO_4 is 0.04 nA at 550 °C. This indicates that it is possible to distinguish between K and Na by operating the SID at low filament temperatures, where the signal is dominated by K compounds in the sample gas.

The signal for each alkali salt displays a unique dependence on filament temperature. Hydroxides exhibit a nearly linear temperature dependence, with considerably higher signals at 800 °C compared to other salts. KCl and NaCl exhibit different responses at

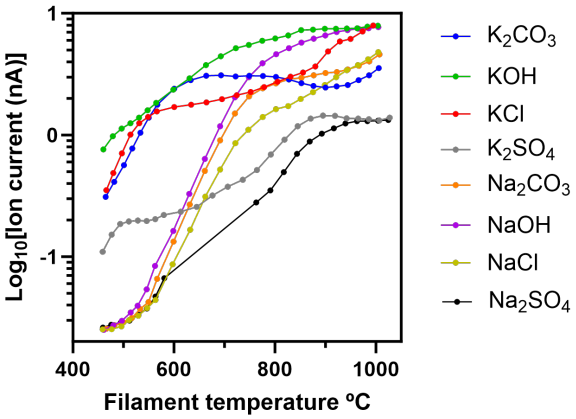

Figure 5.2: Steady state ion current as a function of filament temperature measured during constant injection of K_2CO_3 (blue), KOH (green), KCl (red), K_2SO_4 (grey), Na_2CO_3 (orange), NaOH (magenta), NaCl (yellow) and Na_2SO_4 (black). Adapted from **Paper VI**.

lower temperatures, while becoming more alike at higher temperatures. Distinct patterns also emerge for carbonates, where K_2CO_3 induce a notably high signal around 700 °C, after which its sensitivity to temperature diminishes.

5.1.2 Alkali speciation based on temperature modulation

Based on the results for temperature dependence displayed in Figure 5.2, a procedure has been selected where the filament temperature is repeatedly changed between three temperatures according to the following cycle: 550 – 1100 – 800 – 1100 °C. Experiments were carried out with pure salts and the results showed excellent repeatability and characteristic patterns depending on the type of alkali salt.

The temperature modulation between three filament temperatures is effective for distinguishing between pure alkali salts. However, the signals obtained at three temperatures may not be sufficient to separate individual salts in a salt mixture. To enhance selectivity, information about the transient signals generated during the transition from low to high temperature was incorporated into the analysis. Figure 5.3 illustrates the transient behavior of alkali signal intensity as the filament temperature increases from 550 to 1100 °C (Figure 5.3a) and from 800 to 1100 °C (Figure 5.3b). Elevating the filament temperature from 550 to 1100 °C results in transient peaks in the alkali signal for all salts examined in this study. Notably, there is a considerable difference in the magnitude of the transient peak between sodium and potassium salts, with the latter generating smaller peaks. The response in the alkali signal as the filament temperature increases from 800 to 1100 °C is displayed in Figure 5.3b. For potassium salts, KCl and K_2SO_4 do not produce a transient

peak, while K_2CO_3 generates a minor peak, and KOH displays a clear peak. In contrast, sodium salts produce substantially larger peaks, with the order of peak magnitudes being $NaOH > Na_2CO_3 > NaCl > Na_2SO_4$.

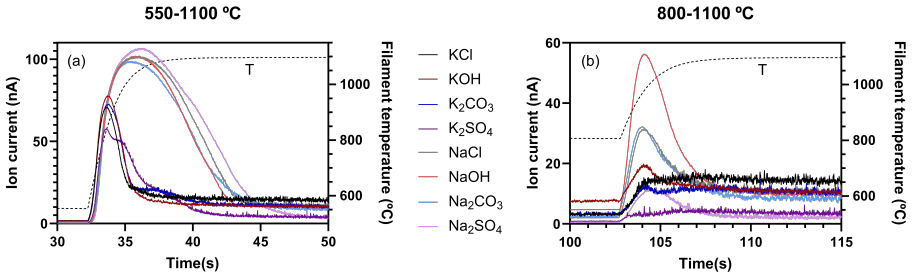

Figure 5.3: Transient change in ion current as the filament temperature is increased from (a) 550 to 1100 °C, and (b) 800 to 1100 °C, with constant injection of KCl, KOH, K_2CO_3, K_2SO_4, NaCl, NaOH, Na_2CO_3 and Na_2SO_4. Adapted from **Paper VI**.

While the time dependence of the transient peaks may be used to speciate different alkali salts, it adds complexity to the analysis during online measurements. Instead, a simplified approach is employed, based on the total integrated area of each transient peak. Therefore, the TMSI procedure used in this study produces five characteristic parameters with a time resolution of 2 min: the steady state signal intensities at 550, 800 and 1100 °C and the total areas of the transient peaks produced by temperature increases from 550 to 1100 °C and from 800 to 1100 °C. The resulting five parameters for each alkali salt compound are summarized in Figure 5.4. The temperature dependence of the steady state alkali signal intensity is consistent with Figure 5.2. Both sodium and potassium exhibit similar temperature dependencies when bound to the same counter ion. Hydroxides produce a strong signal at 800 °C, chlorides result in a minor alkali signal change between 550 and 800 °C, compared to a more significant change between 800 and 1100 °C, and carbonates display similar trends to chlorides but with a less pronounced impact on temperature between 800 and 1100 °C. The displayed results for transient peak areas display major differences for potassium salts compared to sodium salts at the two temperatures, as well as major differences depending on the type of alkali salt. Together, the results described in Figure 5.4 serve as "fingerprints" for the different alkali salts, which improve the possibilities to distinguish them in an unknown mixture.

Discussions regarding specific trends observed for each salt compound, and the procedure for calculating the transient peak areas and steady state signal intensities are presented in **Paper VI**. The novel TMSI method, combined with the summarized data for pure alkali salt compounds, are later used in **Papers VI** and **VII** to determine the composition of the alkali emissions in experiments with OC particles and biomass samples.

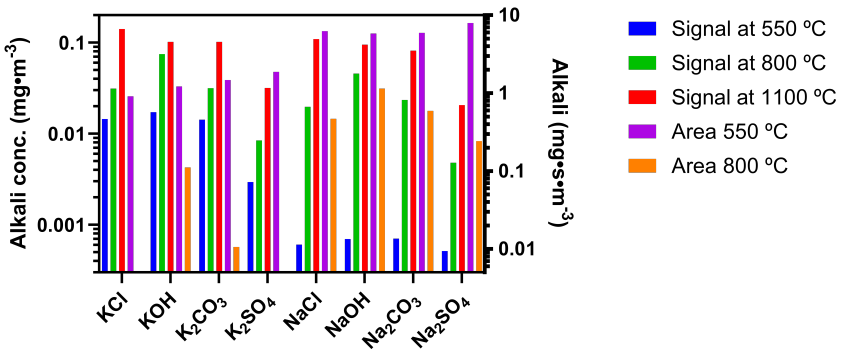

Figure 5.4: SID results from periodic temperature modulation during constant injection of KCl, KOH, K_2CO_3, K_2SO_4, NaCl, NaOH, Na_2CO_3 and Na_2SO_4. The results comprise of steady state alkali signal intensities at 550 °C (blue), 800 °C (green) and 1100 °C (red), and transient peak areas that arise when the filament temperature is increased from 550 to 1100 °C (purple) and 800 to 1100 °C (orange). Adapted from **Paper VI**.

5.2 The behavior of alkali compounds in reactors

Laboratory-scale reactors are essential for in-depth studies of processes like CLC. However, the smaller scale of these reactors can introduce certain challenges when interpreting results. One issue is the higher surface-to-volume ratio in laboratory reactors compared to larger facilities. Additionally, smaller reactors may experience higher wall temperatures due to external heating, unlike larger-scale facilities where heating primarily occurs through the ongoing thermal conversion process. The interaction between alkali components and these high-temperature reactor surfaces can interfere with the specific reactions of interest, such as alkali-OC interactions in CLC. Since OCs play a crucial role in CLC, it is vital to study the gas-solid reactions between gaseous alkali compounds released during fuel conversion and the solid OC particles. To achieve this, it is important to assess the extent to which reactants, like alkali, come into contact with OC particles, which can be challenging if reactor walls have a substantial impact on the process.

5.2.1 Influence of temperature on alkali behavior

The influence of reactor wall processes in alkali studies, presented in **Paper I**, was demonstrated with experiments in an empty laboratory-scale fluidized bed reactor that is considered a standard set-up for studies related to CLC. The experiments were conducted with a constant flow of KCl to the empty **Reactor I** (Figure 3.1a) at temperatures between 25 and 900 °C under recurring reducing, inert and oxidizing conditions. Figure 5.5 presents the steady state values of alkali concentration, particle number concentration

and particle mass concentration for each gas atmosphere and temperature, measured from the reactor exhaust. The two inert conditions, one following the reducing stage and the other following the oxidizing stage, are displayed in bright green and dark green colors, respectively.

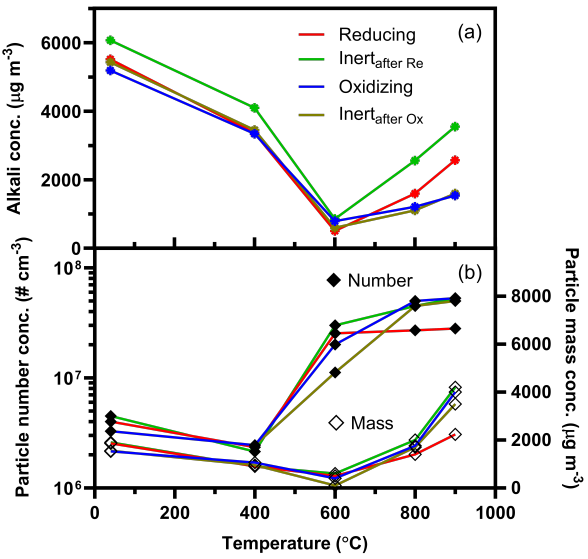

Figure 5.5: (a) Alkali and (b) particle mass and number concentrations as a function of reactor temperature. Measurements were conducted in **Reactor I** during continuous injection of 6 mg $\cdot$ m^{-3} KCl under repeated redox cycles. Each redox cycle consists of reducing (red lines), inert (bright green lines), oxidizing (blue lines) and again inert (dark green lines) conditions.

The alkali concentration in Figure 5.5a shows minimal alkali losses in the reactor at room temperature, and noticeable losses at 400 °C. At these low temperatures, the KCl aerosol particles remain intact and the particle losses at 400 °C are likely a result of particle diffusion in regions with steep temperature gradients. Increasing the temperature to 600 °C causes the KCl salt particles to rapidly evaporate, with most of the resulting gaseous constituents being lost in the reactor. This can be attributed to the diffusion coefficients of KCl molecules being orders of magnitude higher than those of the original salt particles. As a result, the alkali gas will rapidly diffuse to and interact with the inner reactor walls. Alkali reaching the wall surface will either be adsorbed and remain or re-evaporate from the surface and be carried away with the reactor gases. Although up to 92% of the alkali is lost to the walls at 600 °C, the alkali outlet concentration recovers when the reactor temperature increases further to 800 and 900 °C, indicating that more alkali can re-evaporate from the steel surface at higher temperatures. Besides being dependent on temperature, the ability of alkali to re-evaporate from the walls also depends on the gas

composition. Changing the gas composition affects the chemical composition of the wall surface, which affects alkali bound to the surface. The highest alkali concentrations are observed under reducing conditions and the following inert conditions, whereas oxidizing and the following inert conditions yield substantially lower outlet concentrations.

The resulting number and mass concentrations of aerosol particles measured by a SMPS are shown in Figure 5.5b. The SMPS measures the total number concentration and particle diameters in the range between 16-770 nm, and the mass concentration is calculated by assuming particles are spherical with the density of solid KCl. The measured number concentration at 25 and 400 °C aligns with that produced by the aerosol generator, indicating that the aerosol particles remain intact when passing through the reactor. At 600 °C, a substantial drop in mass concentration is observed, while the number concentration increase with approximately one order of magnitude, indicating the formation of newly nucleated particles. The newly nucleated particles are smaller in size but greater in number compared to the particles produced by the aerosol generator. This suggest that the alkali particles evaporate in the hot reactor and subsequently nucleate in the colder downstream regions to form new aerosol particles.

To further evaluate the alkali processes at different temperatures, the following sections provide an in-depth analysis. This encompasses the evaporation and transportation of alkali aerosol particles, and molecular diffusion and penetration of gaseous alkali compounds.

5.2.2 Alkali aerosol evaporation and diffusion

The evaporation of aerosol salt particles as a function of temperature can be described by a semi-quantitative kinetic model, explained in detail in the literature [140]. The model was used in this work to predict the evaporation of aerosol particles at different temperatures in the reactor experiments. The parameter values used for the modelling calculations were taken from Table 1 in reference [140]. The calculation account for changes in the volumetric flow rate, and thus the residence time in the reactor, as a function of temperature.

Figure 5.6 shows the shrinking of 45 nm sized alkali aerosol particles as a function of temperature under conditions representative of the experiments in **Reactor I**. Considering KCl, the aerosol particles begin to evaporate when temperatures exceed 400 °C and are completely evaporated below 520 °C, in accordance with the experimental findings shown in Figure 5.5. Furthermore, it was seen that complete evaporation of KCl particles occurs within a temperature range of 65 °Cwhen operating parameters, like the volumetric flow rate of the gas, the particle diameter and the reactor length, were increased or decreased by approximately 50%. Therefore, minor changes in operating conditions will likely not have a significant impact on the aerosol evaporation during high temperature reactor experiments. However, the type of aerosol compound has a significant effect on the aerosol evaporation, as displayed in Figure 5.6. Compared to KCl, a NaCl particle evaporates at slightly higher temperatures, while KOH evaporates at lower temperatures. The results

show that K_2SO_4 evaporate at significantly higher temperatures compared to the others, with complete evaporation around 800 °C.

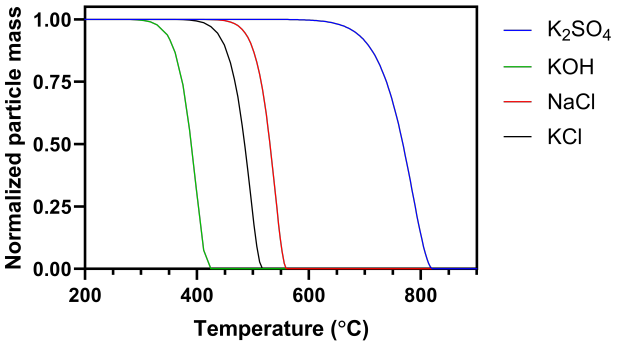

Figure 5.6: Calculated relative particle mass of KCl, NaCl, KOH and K_2SO_4 aerosol particles after passing through Reactor I as a function of reactor temperature. The original particle diameter was 45 nm, and the displayed particle mass is normalized to the mass of the original particles. The kinetic evaporation model and parameter values are described in [140].

The probability for alkali aerosol particles to penetrate the reactor without interacting with walls is calculated from empirical aerosol equations. The penetration, P, of aerosol particles passing through a tube in a laminar flow is calculated from a dimensionless deposition parameter, μ, according to Eq. 5.1 below [86].

$$P = \begin{cases} 1 - 5.50\mu^{2/3} + 3.77\mu & \text{for } \mu < 0.009 \\ 0.819exp(-11.5\mu) + 0.0975exp(-70.1\mu) & \text{for } \mu \geq 0.009 \end{cases} \tag{5.1}$$

The equations have an accuracy of 1% for all values of μ, which is calculated with Eq. 5.2 and based on the particle diffusion coefficient D ($m^2 \cdot s^{-1}$), the tube length L (m) and volumetric flow rate of the gas Q ($m^3 \cdot s^{-1}$).

$$\mu = DL/Q \tag{5.2}$$

$$D = \frac{k_B T C_c}{3\pi\eta d_p} \tag{5.3}$$

$$C_c = 1 + \frac{\lambda}{d_p} 2.34 + 1.05exp(-\frac{0.39 d_p}{\lambda})] \tag{5.4}$$

The diffusion coefficient of aerosol particles were calculated with the Stokes-Einstein Eq. 5.3, from Boltzmann's constant k_B ($m^2 kg \cdot s^{-2} K^{-1}$), temperature T (K), the dimensionless Cunningham correction factor C_c, the viscosity η (Pa · s) and the particle diameter d_p (m). The Cunningham correction factor is calculated by Eq. 5.4, based on the mean free path of particles λ (m) and the particle diameter.

The penetration of 45 nm KCl particles was calculated for reactor temperatures of 25 and 500 °C, using diffusion coefficients of $3.2 \cdot 10^{-5}$ and $1.0 \cdot 10^{-4}$ $cm^2 \cdot s^{-1}$, respectively. The total particle penetration was calculated by combining a 2 m long tube feeding aerosols to the reactor with the almost 1 m tall reactor and a 1 m long exhaust tube. The total transmission of particles through the reactor system and tubes is above 96% at both temperatures. The effect from the three times higher diffusion coefficient at 500 °C is almost completely cancelled out by the almost three times higher volumetric flow rate, resulting in lower residence times in the reactor at high temperature. Therefore, according to the model in Eq. 5.1, 45 nm KCl particles will follow the laminar gas flow with minimal losses to the walls while being fed to the reactor, inside the reactor at both 25 and 400 °C and in the exhaust lines leaving the reactor. However, the model does not account for temperature gradients in the exiting flow, where thermophoretic forces tend to drag small particles towards the cold walls [86], which may result in increased losses.

5.2.3 Molecular diffusion and penetration of gaseous alkali

As previously described and as shown in Figure 5.6, alkali aerosol particles rapidly evaporate to their molecular constituents at high temperatures. Therefore, the alkali will be in gaseous form inside the heated section of the reactor during high-temperature operation. With drastically increased diffusion coefficients for gases compared to aerosol particles, the alkali gas is expected to rapidly reach the reactor wall surface. In addition to what is presented in **Paper I**, the amount of alkali gas reaching the reactor wall by molecular diffusion can be calculated with a radial diffusion model, developed by Knopf, Pöschl and Shiraiwa (KPS method) [153]. The same model was used to calculate alkali losses due to molecular diffusion in **Paper III**. The model calculates the penetration of gas molecules trough a laminar flow reactor according to Eq. 5.5,

$$P_X = exp\left(-\frac{\gamma_X}{1 + 3\gamma_X/2N_{Shw}^{eff} Kn_X}\frac{\omega_X}{D_{tube}}t\right) \tag{5.5}$$

where P_X is the penetration of gas species X in a laminar flow, γ_X is the uptake coefficient which is assumed to be unity, N_{Shw}^{eff} is the effective Sherwood number, Kn_X is the Knudsen number, ω_X is the thermal molecular velocity, $D_{reactor}$ is the reactor diameter and t is the residence time. All parameters are listed and described in Table 1 of **Paper III**, including values for KCl(g) in N_2 at 900 °C. The penetration of alkali gas molecules through the reactor depends on the gas-phase diffusion coefficient, which can be calculated based on Graham's law of diffusion, according to Eq. 5.6 [154], where M_1 and M_2 are the molecular masses of species 1 and 2, respectively. Based on known values for N_2 [155], the gas-phase diffusion coefficient for KCl at ambient atmosphere was calculated to 0.095 $cm^2 \cdot s^{-1}$. The coefficient was adjusted for high temperatures according to Eq. 5.7, where D_g is the diffusion coefficient and p is the pressure. Based on Graham's method, the gas-phase diffusion coefficient for KCl molecules at 900 °C was calculated to 0.85 $cm^2 \cdot s^{-1}$.

$$\frac{Rate_1}{Rate_2} = \sqrt{\frac{M_2}{M_1}} \tag{5.6}$$

$$D_g \propto T^{1.5}/P \tag{5.7}$$

Figure 5.7 show the penetration of KCl molecules as a function of the axial distance travelled in **Reactor I** when operated at 500, 700, 900 and 1100 °C, calculated from the employed KPS method. The calculations were simplified by assuming a uniform temperature profile inside the reactor, and thus ignoring the effects of large regions with temperature gradients. Figure 5.7 shows that the penetration of KCl molecules is below 10% after 40 cm travelled distance at all temperatures, indicating that KCl molecules rapidly diffuse to the inner reactor walls. Minor influence of temperature is observed, where the penetration decreases with increasing temperature. With a furnace height of 60 cm (see Figure 3.1), it is likely that all KCl molecules will reach the hot walls of **Reactor I** during high temperature operation.

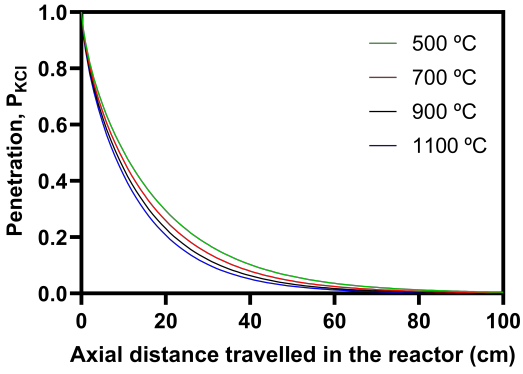

Figure 5.7: Penetration of KCl molecules as a function of the axial distance travelled in **Reactor I** at different temperatures, calculated with the KPS method [153]

5.2.4 Influence on redox processes

Experiments were carried out with a constant injection of KCl to the empty **Reactor I**, operated at 900 °C temperature during several consecutive redox cycles. Figure 5.8a shows the observed alkali and gas concentrations measured in the reactor exhaust from five consecutive redox cycles. High reproducibility is observed between the redox cycles for both alkali and gas concentrations. To easier elaborate on the influence of different gas conditions, the alkali and gas concentrations for a single redox cycle is depicted in Figure 5.8b. The colored areas in the figure mark periods with reducing (orange), inert (white) and oxidizing (blue) gas conditions. The gas concentrations generally reach their steady state

levels within approximately 100 s or less. Significant transients occur when transitioning in and out of reducing conditions, while minor transient changes are observed during the transitions between inert and oxidizing atmosphere. When introducing reducing gases, the alkali concentration rapidly decreases, and gradually recovers after approximately 200 s. Upon returning back to inert gas composition, the system experiences a major release of alkali, which diminishes over time and eventually approaches the previous level. The short time scales to reach steady state after each gas shift suggested that changes in gaseous alkali concentration are dominated by changes in surface properties of the wall, and the observed pattern is seen across all cycles.

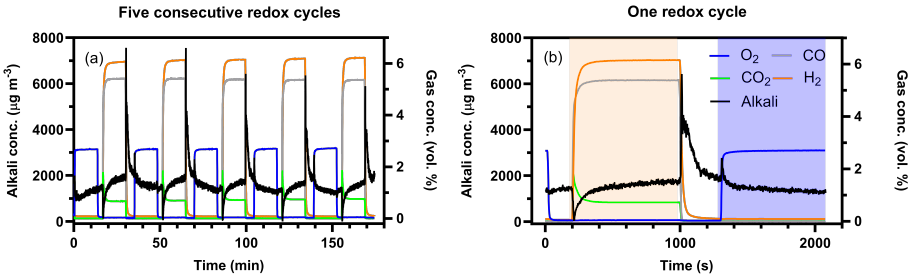

Figure 5.8: Alkali and gas concentrations measured during (a) five consecutive redox cycles, and (b) one redox cycle, with constant injection of 6 mg · m^{-3} KCl to **Reactor I** operated at 900 °C. Colored fields mark periods with reducing (orange), inert (white) and oxidizing (blue) conditions. Figures adapted from **Paper I**.

As previously described, the concentration of alkali leaving the reactor depends on the balance between the flow of alkali from the gas phase to the wall and the amount of alkali that can subsequently evaporate from the steel surface. The composition of the wall material was determined with SEM-EDS analysis. The composition aligns with that of stainless steel alloy 304, compositing mainly of Fe, Cr and Ni. In oxidizing conditions, the steel surface is expected to consist of chromium and iron oxides [112–114, 156], where potential products from reaction with KCl include K_2CrO_4 and $K_2Fe_2O_4$ [32, 112, 113]. Surface conditions remain relatively stable during the inert phase following the oxidizing stage, but undergo significant changes when transitioning to reducing conditions. Initially, there is a sharp drop in alkali concentration at the start of the reducing phase, followed by a gradual recovery to a higher level over a few hundred seconds. Simultaneously, there is a peak in CO_2 production Figure 16b, followed by a decrease on a similar timescale as the alkali changes. This behavior may be attributed to the reduction of iron oxides on the surface layer, as predicted by an Ellingham diagram [157] and catalyzed by the presence of KCl [158]. The reduction of this surface layer provides binding sites for potassium, which is temporarily lost to the newly formed surface. However, the kinetics slow down after the initial changes, limiting the growth of a potassium-rich phase over longer timescales. The existing literature suggests that the oxide layer is dominated by Cr_2O_3 with the potential

formation of K_2CrO_4 in presence of KCl [32], but further studies are required to pinpoint the precise surface state responsible for these observations. Intriguingly, the newly formed alkali-containing phase seems to be stable only under reducing conditions, as evidenced by a sharp rise in alkali concentration when switching back to inert conditions.

5.2.5 Influence of a fluidized bed

The influence of a fluidized bed was studied by conducting experiments with a constant injection of KCl to **Reactor I**, operated with a fluidized bed of 20 g calcium manganite at 900 °C. The results are presented in detail in **Paper II**. Figure 5.9 shows the observed alkali and gas concentrations measured in the reactor exhaust from one redox cycle. Included in the figure is the observed alkali concentration from the corresponding experiment without a fluidized bed present in the reactor (red dashed line).

As seen in Figure 5.9a, the alkali behavior is affected by the presence a fluidized bed of OC particles compared to the empty reactor experiments, and changes in gas composition lead to changes in the alkali level. The transient behavior is generally less pronounced and observed patterns are not always in the same direction as the observed patterns with an empty reactor. The most notable example is an increase in alkali concentration at the beginning of the reducing phase when an OC bed is present compared to the observed behavior with an empty reactor. In addition, changes in alkali level are observed due to oxidation and reduction of the OC.

Figure 5.9b shows the differential alkali concentration obtained by subtracting the concentration measured in the empty reactor (red dashed line in Figure 5.9a) from the results obtained with OC in the reactor (black solid line in Figure 5.9a). Negative values are interpreted as alkali uptake by the OC, while positive values are interpreted as alkali release from the OC. The observed difference in Figure 5.9b is negative or close to zero for most conditions. The initial part of the reducing stage is an exception, where positive values suggests alkali release from the OC.

To summarize Section 5.2, alkali in the form of aerosol particles remain in condensed form up to several hundred degrees with relatively low particle diffusion coefficients. This allows alkali to be transported to and from reactors with limited losses to the tube walls, as well as transported through a reactor without significant wall losses at temperatures below the aerosol evaporation point, which is 500 °C for 45 nm sized KCl particles. It is, therefore, convenient to use aerosol particles as a method to dose alkali into a reactor over a wide concentration range. At higher temperatures, the alkali compounds will rapidly evaporate and form gaseous compounds with greatly increased diffusion coefficients. This increases their interaction with available surfaces, such as reactor walls or fluidized bed particles. Since the gaseous alkali rapidly reach the hot walls of **Reactor I** when no fluidized bed is present, the concentration of detectable alkali in the exhaust will be affected by the alkali desorption rate from the walls. The reactor employed here is a typical setup for fluidized bed studies on laboratory-scale and the observations indicate that the properties

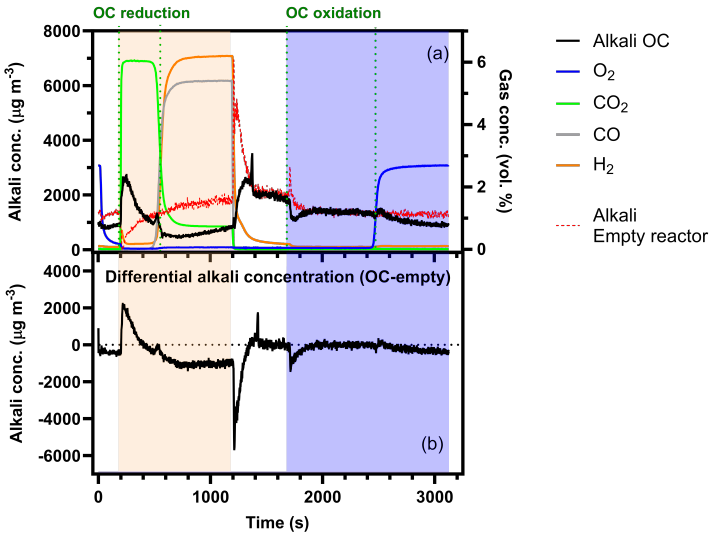

Figure 5.9: (a) Outlet alkali and gas concentrations measured from experiments with continuous injection of 6 mg · m^{-3} KCl to 20 g fluidized bed of calcium manganite (solid lines) and empty reactor (red dashed line) during one redox cycle at 900 °C. (b) Differential alkali concentration obtained by subtracting the alkali concentration in empty reactor experiment (dashed red line) from the OC experiment (solid black line). Colored areas mark stages with inert (white), reducing (orange) and oxidizing (blue) conditions.

of the reactor walls influence the actual amount of alkali that is able to reach and interact with a fluidized bed of OC particles. Detailed interactions between OCs and alkali may therefore be obscured by the large effects from the reactor walls.

5.3 Development of a novel fluidized bed reactor

One significant outcome of the alkali experiments in **Reactor I** was the problems regarding the extended hot regions above and below the fluidized bed where alkali in gaseous form can interact with the hot reactor walls, influencing the alkali interactions with the fluidized bed. Other problems relate to the ineffective cooling of the gas flow leaving the fluidized bed, which limits the aerosol nucleation processes, and the presence of cold reactor walls where surface condensation of alkali gas or newly nucleated alkali aerosols may be significant.

The studies of **Reactor I** inspired the development of a novel laboratory reactor. The new reactor was designed to limit alkali losses below and above the fluidized bed, to facilitate investigations of the interactions between alkali and the bed particles. The

development and first application of the novel reactor is presented in **Paper V**. The reactor design is based on fundamental understanding regarding the behavior of alkali aerosol particles and gases in the relevant temperature ranges, as discussed in Sections 5.2.2 and 5.2.3. The geometry was developed through an iterative process of computational fluid dynamics (CFD) simulations, where the final configuration (**Reactor II** in Figure 3.2b) was constructed in a stainless steel material with excellent corrosion resistance.

5.3.1 Design considerations and construction

The novel laboratory reactor configuration is schematically presented in Figure 5.10, where the color scheme illustrates: heated areas (red), insulated areas (green), and areas at ambient temperatures (blue). Figure 5.10a depicts the reactor before experiments, and Figure 5.10b shows its dimensions in mm along with the flow directions of aerosol, reactor gases, and exhaust gas. The configuration can be separated into three main sections: *i)* a gas and alkali inlet section below the fluidized bed, *ii)* a hot middle section including the fluidized bed, and *iii)* a third section with lower temperatures downstream of the fluidized bed including the exhaust gas outlet.

i) In the first section, a narrow tube in the center of the reactor body which exits just before the fluidized bed is used to introduce the cold flow of alkali aerosol particles, see Figure 5.10c. The use of a narrow tube diameter results in a high velocity and short residence time for the inlet gases, which enables the aerosol flow to maintain a relatively low temperature. As a result, the alkali remain in condensed form with limited wall losses beneath the fluidized bed [86]. The operating temperature of the bed is maintained by preheating the separate flow of reactor gases before it is introduced to the reactor. Additionally, the inlet for the reactor gases is tangentially connected to the reactor body (see Figure 5.10d), creating a swirling motion for the preheated gas inside the reactor. This swirling motion of the reactor gas surrounds the central aerosol flow, which further limits the transport of alkali to the reactor walls. This specific inlet configuration is designed to prevent aerosol evaporation beneath the bed, keep the alkali flow separated from the reactor walls while simultaneously achieving a uniform temperature within the fluidized bed. Consequently, interactions between alkali and the reactor walls beneath the bed should be significantly reduced compared to **Reactor I**.

ii) Another major difference from previous reactor is that the furnace height is reduced from 420 to 200 mm. This eliminates a substantial portion of the heated wall surface where there is no fluidized bed, resulting in an overall decrease in alkali-wall interactions. Moreover, the stainless steel surface layer of **Reactor I** generally consists of iron and chromium oxides which can react chemically with alkali, forming potential products of K_2CrO_4 and $K_2Fe_2O_4$ [112, 113]. Therefore, the hot sections of the new reactor is constructed in APMT$^{\mathbf{TM}}$ (Sandvik AB) which forms a stable,

non-scaling α-Al_2O_3 surface oxide in the relevant conditions, aiming to restrict chemical reactions with alkali.

iii) The final reactor section downstream of the furnace experience ambient temperatures, and is notable for a larger reactor diameter compared to the preceding sections. The increased diameter results in lower gas velocities which extends the residence time and therefore enhance the cooling of the gas as it exits the fluidized bed. Rapid cooling of the hot reactor gases improves the alkali aerosol nucleation process and thus the subsequent alkali particle transportation away from the reactor, to the alkali detectors [86]. In addition, the lowered gas velocity prevents fluidized bed particles to be carried away by the gas stream. Moreover, the increased diameter reduce the surface-to-volume ratio, which favorable when aiming to limit alkali condensation onto cold surfaces.

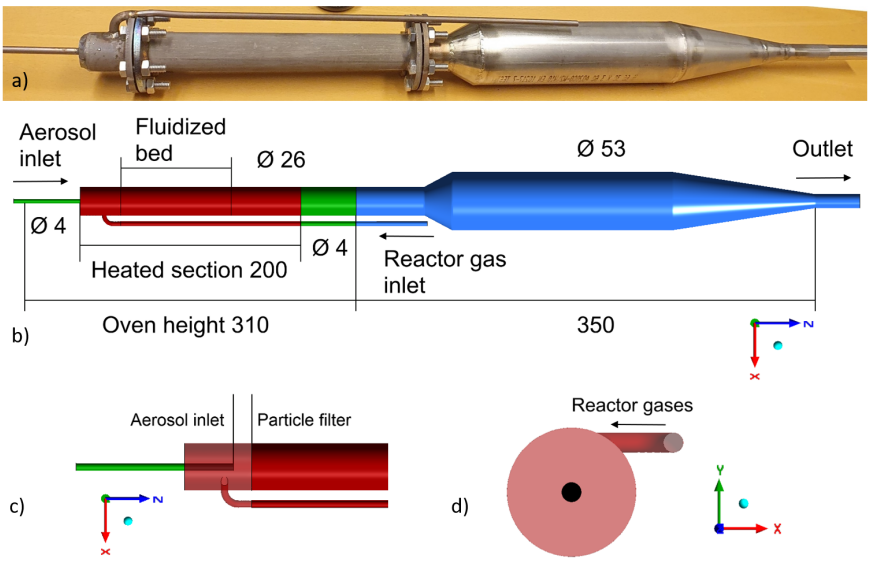

Figure 5.10: Schematic overview of the laboratory-scale fluidized bed reactor with dimensions in (mm). Red fields mark heated areas, green fields mark insulated areas and blue fields mark ambient temperature areas. Adapted from **Paper V**.

5.3.2 Computational fluid dynamics simulations

CFD simulations were used to refine the geometric configuration of the new reactor, concerning alkali processes at relevant temperatures. A detail description about the CFD simulation process, including the simulation schemes, physical models, boundary conditions, and the characteristics of the mesh can be found in **Paper V**. Additional CFD

simulations were carried out for the previously used **Reactor I**, and Figure 5.11 compares the temperature profiles within the two reactors.

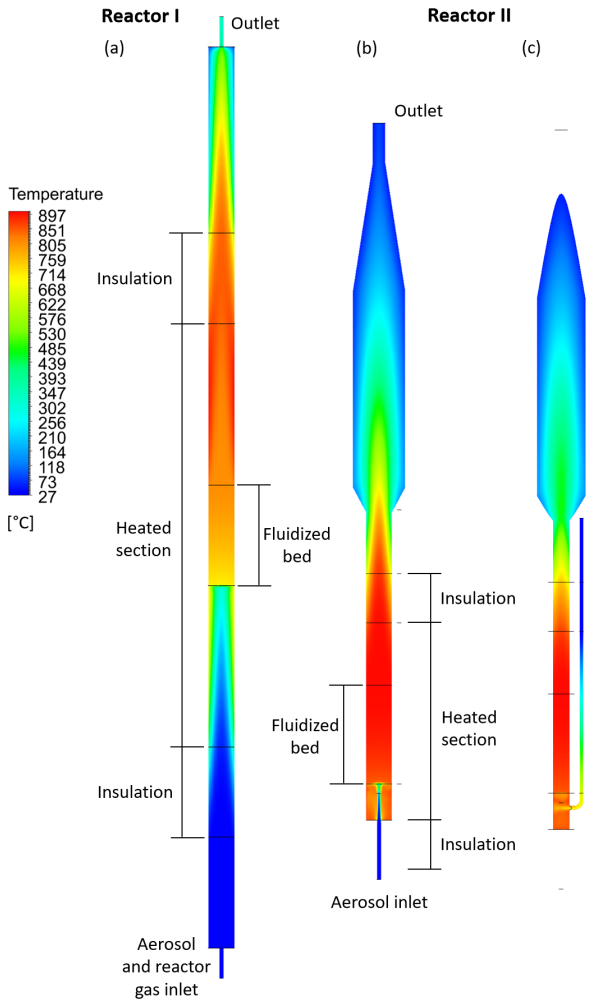

Figure 5.11: Results from CFD simulations showing temperature profiles of the cross section flow path in (a) the center of **Reactor I**, (b) the center of **Reactor II**, and (c) in the center of the reactor gas inlet tube of **Reactor II**.

Reactor I, Figure 5.11a, displays extensive regions of elevated temperature both above and below the fluidized bed within the heated section. A substantial fraction of the injected alkali aerosol flow encounters high temperatures prior to reaching the fluidized bed, leading to the evaporation of alkali salts and subsequently rapid diffusion of alkali-containing

compounds towards the walls. Consequently, alkali-wall interactions significantly influence the flow of alkali reaching the fluidized bed. This situation is also applicable after the fluidized bed, where alkali compounds leaving the bed are highly likely to interact with the heated wall before exiting the reactor.

In contrast, the redesigned inlet and outlet regions in the new reactor significantly mitigate these issues. The temperature profiles in the cross section flow path of **Reactor II**, Figure 5.11b, shows that most of the aerosol flow stays below 400 °C, meaning that the alkali remain in particle form, before reaching the fluidized bed. As alkali particles enter the bed, the temperature rapidly rises above the evaporation point, facilitating gaseous alkali interactions with the solid bed particles. The wider reactor section downstream of the furnace experience ambient temperatures that effectively cools the gas flow leaving the fluidized bed, as seen in Figure 5.11b. The results show that the gas flow temperature is below 100 °C before exiting the reactor, with the resulting assumption that all alkali will exist in the form of aerosol particles

Another issue in **Reactor I** (Figure 5.11a) is the temperature gradient within the central part containing the bed, where **Reactor II** (Figure 5.11b) display a more uniform temperature distribution. The enhanced uniformity can primarily be attributed to the gas preheating system integrated into the new reactor design. This is illustrated in Figure 5.11c, showing the inlet configuration of the reactor gas flow, where gas is preheated in a tube alongside the main reactor body inside the furnace.

5.3.3 Experimental functionality validation

Experiments were carried out to evaluate the performance of the novel reactor. The alkali interactions with the inner reactor walls were studied by injecting KOH aerosol particles to the empty reactor when operated at temperatures between 160 and 900 °C under reducing, oxidizing and inert conditions. The results were in line with the findings from the empty reactor experiments conducted in **Reactor I**. Namely that limited losses of alkali aerosol particles were seen when the reactor operated at temperatures below 500 °C while a sharp drop in the outlet alkali concentration was observed at higher operating temperatures, where the alkali is in molecular form. Further details can be found in **Paper V**.

Important to emphasize is that the new laboratory reactor was designed to limit the alkali losses to reactor walls above and below a fluidized bed. When the reactor is operated without a fluidized bed present, the gaseous alkali will still be able to rapidly diffuse to and interact with the reactor walls in the new reactor. To investigate the influence from reactor walls during fluidized bed operation, experiments were carried out with different amounts of OC particles present in the reactor. Figure 5.12 shows the outlet alkali concentration measured during one redox cycle at 900 °C in an empty reactor and with a fluidized bed of 5, 10 or 20 g of calcium manganite present in the reactor. Strong interactions between KOH and the inner steel walls are observed in the absence of a fluidized bed. The alkali concentration exhibits significant transient effects when shifting gas composition, before a

steady state is established within a few hundred seconds. The transient behavior becomes particularly pronounced when reducing conditions are applied, while transitions between inert and oxidizing conditions have a comparatively minor impact. The introduction of just 5 g of OC (black line in Figure 5.12) significantly influences the outcome and alters the qualitative behavior in different gas conditions. The transient peak observed during reducing conditions disappears, and the alkali concentration remains consistently lower than observed in the empty reactor throughout all stages. This pattern is also observed when using 10 and 20 g of OC (green and red lines in Figure 5.12), with the alkali concentration decreasing as the size of the fluidized bed inventory increases. Furthermore, changes in gas composition affect the surface properties of the OC, which in turn changes the alkali levels during the oxidation and reduction of the OC. These transient effects tend to be less pronounced compared to the results obtained in the empty reactor, where the dominant factor is the interaction between alkali and the reactor wall.

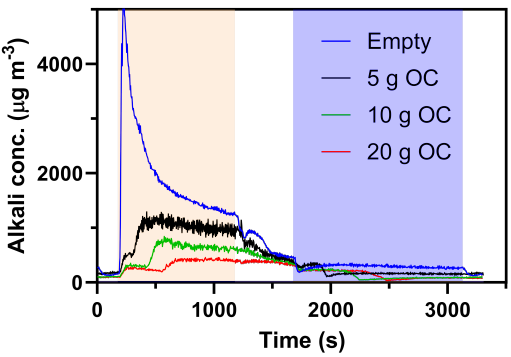

Figure 5.12: Outlet alkali concentrations measured during one redox cycle with KOH injection to the reactor operated at 900 °C. The colors represent results for experiments with empty reactor (blue lines) and when the reactor is filled with 5 g OC (black lines), 10 g OC (green lines) and 20 g OC (red lines). Colored areas mark stages with oxidizing (blue), inert (white) and reducing (orange) atmospheres. Adapted from **Paper V**.

The observations indicate that in the OC results, alkali-OC interactions are dominant, while the influence of alkali-wall interactions is minor and diminishes as the inventory size increases. To assess the relative importance of these two surface types within the reactor, the total surface areas of the OC bed and the hot reactor walls can be estimated. The calcium manganite material has a BET specific surface area of 0.2 $m_2 \cdot g^{-1}$ [82], resulting in approximate total surface areas of 1, 2 and 4 m^2 for the 5, 10 and 20 g of OC beds, respectively. In contrast, the hot zone of the reactor has a geometric area of 0.016 m^2, roughly 60 to 240 times smaller than the total surface areas of the fluidized beds. Although the actual wall surface area is expected to be larger due to microscopic surface features, the OC surface area substantially exceeds the wall area within the hot zone of the reactor, aligning with the notable effects observed when introducing 5-20 g

of OC. The extensive wall interactions witnessed in empty reactor experiments are thus unlikely to influence the results observed during fluidized bed operation to a significant extent. Increasing the fluidized bed inventory will further reduce the influence of reactor walls and is, therefore, beneficial in future alkali experiments.

Figure 5.13 provides a comparative illustration of the observed alkali concentrations while operating both types of laboratory reactors at 850 °C with a constant KCl injection. Figure 5.13a displays significant differences in the empty reactor results. Three distinct transients are observed in **Reactor I** (black line), including an abrupt drop in alkali signal when introducing reducing gases, followed by a peak when shifting to inert atmosphere, and a second peak when shifting to oxidizing atmosphere. In contrast, **Reactor II** (red line) lacks these transients in inert and oxidizing conditions, and the alkali concentration exhibits a sharp increase in the initial phase of the reducing period. The alkali concentrations converge towards similar levels for both reactors, in the end of each stage of the redox cycle. The lack of transients in **Reactor II** may be due to a more stable surface layer on the hot reactor walls. While oxide layers on the wall surface of 5.13 may be more affected by changes in gas composition (see Section 5.2.4).

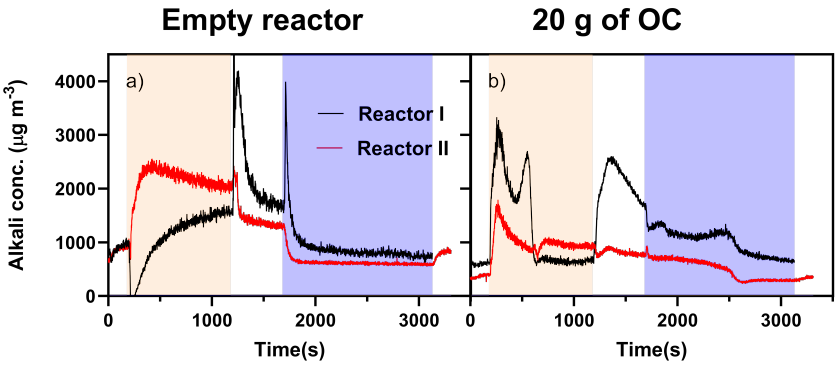

Figure 5.13: Outlet alkali concentrations measured during one redox cycle at 850 °C reactor temperature with constant KCl injection to (a) empty reactor and (b) reactor filled with 20 g of OC. The colors represent results for experiments with **Reactor I** (black lines) and the novel **Reactor II** (red line). Colored areas mark stages with oxidizing (blue), inert (white) and reducing (orange) atmospheres. Adapted from **Paper V**.

Figure 5.13b presents experimental results using 20 g of the same calcium manganite in both reactors. Since the observed alkali concentration differs for the two reactors, the results are clearly influenced by the configuration of the reactor. One major difference is seen in the inert period following the reducing stage, where a clear alkali peak is seen from **Reactor I**, while **Reactor II** show a more stable concentration. Another clear difference is seen in the middle of the reducing period, where **Reactor I** shows a second peak in the alkali concentration, that is not observed in **Reactor II**.

In conclusion, the novel laboratory reactor design presents an improvement over reactor designs that are typically employed for these kind of studies, as demonstrated when compared to **Reactor I**. The lack of transients in the alkali concentration from **Reactor II** when changing gas composition in empty reactor experiments is an obvious advantage. Another clear benefit with the novel design is that the surface area of OC particles is one to two orders of magnitude higher compared to the area of hot reactor walls, whereas in the previous reactor, substantial areas of hot reactor walls were accessible above and below the fluidized bed. The experiments also reveal that addition of merely 5 g of OC is adequate to qualitatively alter the alkali behavior compared to an empty reactor (as depicted in Figure 5.12), indicating a limited influence of the reactor walls.

5.4 Online characterization of alkali uptake

This part describes the uptake and release of different alkali compounds by three different OC materials that are considered state of the art in CLC. The novel laboratory-scale reactor and TMSI alkali detection method described in previous sections are employed to study alkali-OC processes at different temperatures and atmospheric conditions.

Experiments were carried out where 40 g of either manganese oxide, calcium manganite or ilmenite OC particles were fluidized in **Reactor II** at a constant temperature of 900 °C. Recurring reducing, inert and oxidizing conditions were simulated by introducing synthetic fuel gas, nitrogen and synthetic air to the reactor. The inlet gas concentrations are presented in **Paper VII**, where the time duration for each gas condition depends on the type of OC material being fluidized, as presented in Table 1 of the same paper. Alkali vapor in the form of KCl, NaCl, KOH, NaOH, K_2SO_4 and Na_2SO_4 is continuously injected to the fluidized bed while the outlet alkali concentration is monitored by a dual SID-setup, as explained in Section 3.3.

5.4.1 Alkali concentrations during repeated redox cycles

Figure 5.14 shows the outlet alkali and gas concentrations from fluidized bed experiments with the three OC materials. Each experiment included multiple redox cycles with individual injection of six different alkali salts. Typically, 2 – 4 redox cycles with KCl injection were followed by 2 – 4 redox cycles with KOH injection and lastly 2 – 4 cycles with K_2SO_4 injection. The same type of experiment was then repeated with sodium salts before changing the bed material.

Figure 5.14a shows the experimental results obtained from experiments a fluidized bed of Mn_3O_4 in the reactor. The results show significant variations in gas concentrations within each redox cycle, with high reproducibility between cycles. The same is observed for the alkali concentration during KCl injection. Transitioning from KCl to KOH injection leads to a rapid decrease in alkali concentration, indicating efficient adsorption by the

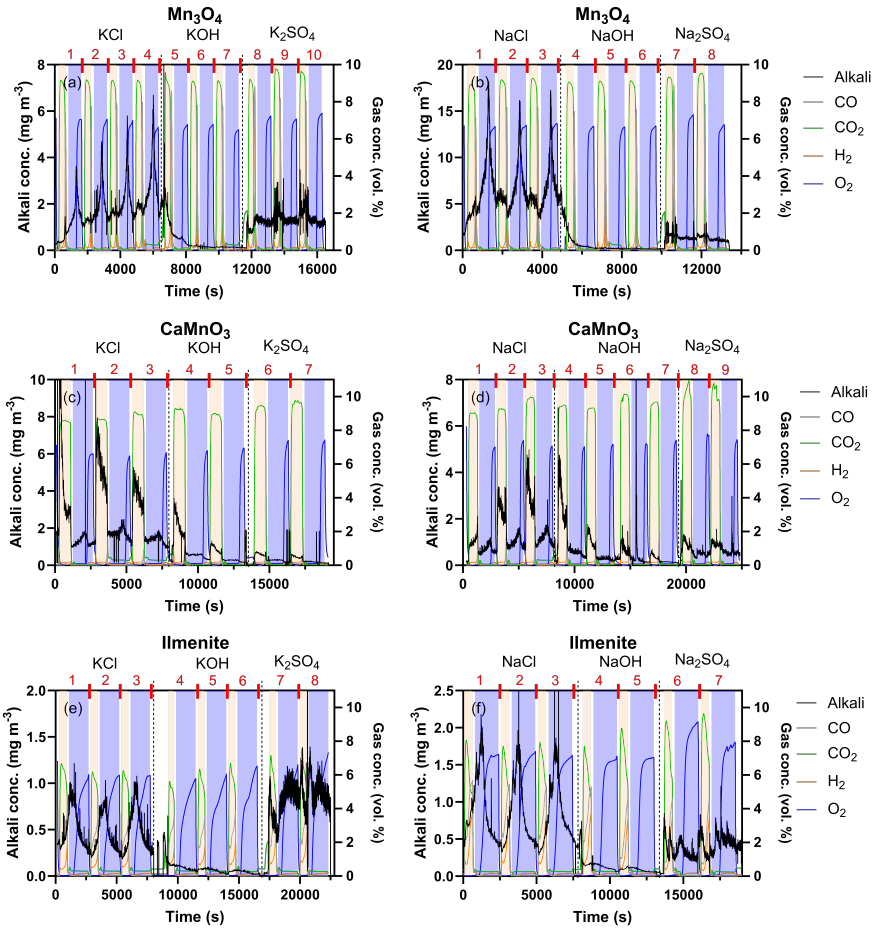

Figure 5.14: Alkali and gas concentration measurements during fluidized bed experiments of (a, b) Mn_3O_4, (c, d) $CaMnO_3$, and (e,f) ilmenite particles. Alkali aerosol of (a, c, e) KCl, KOH or K_2SO_4, and (b, d, f) NaCl, NaOH or Na_2SO_4 was continuously fed to the reactor during several consecutive redox cycles at 900 °C. Adapted from **Paper VII**.

Mn_3O_4 particles, and the alkali remains bound to the bed material regardless of the gas composition within the redox cycle. The alkali signal then reappears when replacing KOH by K_2SO_4, indicating less efficient uptake compared to KOH. The alkali concentrations are similar for KCl and K_2SO_4, indicating a similar degree of alkali uptake by Mn_3O_4. However, the observed pattern differs with respect to gas composition for the two salts, showing that the detailed alkali-OC interactions depend on both the type of alkali salt and the gas composition.

Figure 5.14b shows the corresponding results when sodium salts interact with the fluidized bed of Mn_3O_4 particles. Qualitatively, the results are similar to those observed for the potassium salts, with extensive uptake of NaOH and similar patterns of the alkali concentration with respect to gas composition for NaCl and Na_2SO_4. However, a major difference between sodium and potassium salts is the significantly higher alkali outlet concentration for NaCl compared to KCl. This indicated significant differences in their alkali uptake efficiency, where NaCl is more likely to escape from the fluidized bed.

Considerable changes are observed in the alkali concentration when the fluidized bed material is changed to $CaMnO_3$, Figure 5.14c and Figure 5.14d. While the alkali chlorides are still more likely to escape from the bed compared to hydroxides and sulfates, the differences between the latter two are generally smaller compared to the observations for Mn_3O_4. Moreover, the alkali uptake is generally more efficient during oxidizing conditions compared to reducing conditions for all investigated alkali salts.

Further differences with respect to alkali-OC interactions are observed when changing the bed material to ilmenite particles (Figure 5.14e and Figure 5.14f). Compared to the other two bed materials, the outlet alkali concentrations from ilmenite experiments are substantially lower for all alkali salts under all conditions. This is in accordance with the well-known ability of ilmenite to efficiently capture alkali [34, 36, 73]. The trends with respect to alkali salts are similar to the other experiments, with exceptionally low outlet alkali concentrations during alkali hydroxide injection compared to chlorides and sulfates.

Conclusively, the results in Figure 5.14 shows that the alkali uptake characteristics depends on the type of alkali salt being injected, the type of fluidized bed material and the gas composition in the reactor. The results are summarized in Figure 5.15, showing the average alkali outlet concentrations in reducing and oxidizing conditions for all combinations of alkali salts and OC materials. The results indicate substantial differences in alkali uptake efficiency between the OC materials, where ilmenite is by far most efficient, followed by calcium manganite and manganese oxide.

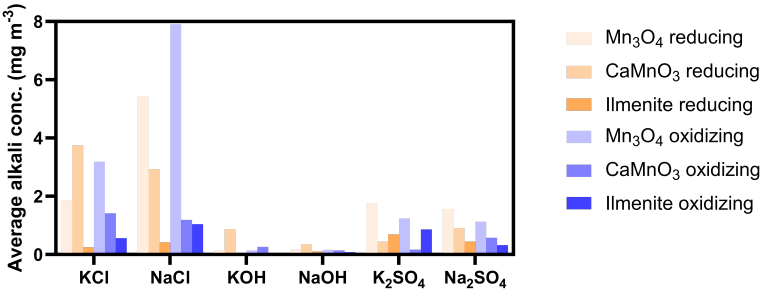

Figure 5.15: Average alkali concentrations in reducing (orange) and oxidizing (blue) conditions when the reactor is filled with 40 g of Mn_3O_4, (bright colors) $CaMnO_3$ (medium bright colors) and ilmenite (dark colors) particles.

In summary, alkali chlorides have a greater tendency to escape from the bed materials in contrast to hydroxides and sulfates. Manganese oxide and ilmenite demonstrate efficient adsorption of alkali hydroxides when compared to chlorides and sulfates. Oxidizing conditions typically result in lower alkali concentrations compared to reducing conditions in experiments with calcium manganite, while experiments using ilmenite and manganese oxide typically result in the opposite trend with higher alkali concentrations in oxidizing conditions relative to reducing conditions.

5.4.2 Influence of redox processes on alkali uptake

To investigate the alkali uptake characteristics in further detail, the outlet alkali and gas concentrations are displayed for single redox cycles. Figure 5.16 shows the results for single redox cycles during fluidization of the three OCs with continuous injection of KCl and NaCl. Corresponding results for the other alkali salts can be found in **Paper VII**.

Starting with Mn_3O_4 (Figure 5.16a and 5.16b), the observed gas concentrations display effective reduction and oxidation of the OC. The reducing stage indicates excellent gas conversion with high CO_2 and low H_2 and CO concentrations. The completion of the OC reduction is marked by a rapid drop in CO_2 concentration with a simultaneous increase in the fuel gas concentrations. The oxidizing conditions display complete uptake of the introduced O_2 until the OC is fully oxidized, at the point where the outlet O_2 concentration rapidly increase. The observed alkali concentrations when injecting KCl and NaCl to the fluidized bed of Mn_3O_4 remains relatively stable throughout the entire reduction phase and exhibits comparable levels during the neighboring inert stages, for both KCl and NaCl. This implies that the alkali uptake is unaffected by the extent of reduction of the OC material. However, the alkali concentration rises during the OC oxidation process, which implies a less efficient alkali uptake during this process. Notably, there is a distinct peak in alkali concentration around the point when the OC reaches complete oxidation, followed by a gradual decrease over the remaining part of the oxidation stage. This gradual adjustment to new steady-state conditions suggests that the underlying process responsible for these observations is governed by kinetics on the timescale of the experiment.

Changing the fluidized bed to $CaMnO_3$ (Figure 5.16c and 5.16d), the outlet gas concentrations again show complete conversion of the fuel gases to CO_2 during the reducing period and complete O_2 uptake during the OC oxidation process under oxidizing conditions. More than the double amount of time is required for complete oxidation and reduction compared to Mn_3O_4, which can partly be explained by the fact that the latter only consist of 40% active phase, while the remaining 60% is inert support material [75]. The alkali concentrations display significantly different behavior with respect to gas conditions during $CaMnO_3$ operation compared to Mn_3O_4. The alkali outlet concentration rapidly increases when the reducing gases are introduced. A gradual decay in the alkali concentration is observed as the OC reduction process proceeds, before shifting to inert gases results in a sharp drop in the concentration. The alkali concentration then remains relatively stable

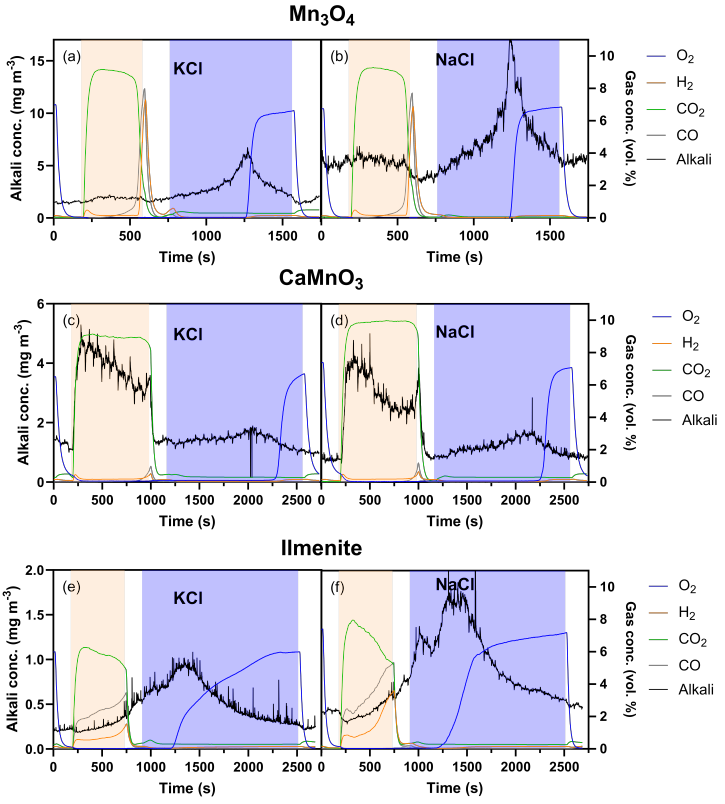

Figure 5.16: Alkali and gas concentrations measured during one redox cycle with 40 g fluidized bed of (a, b) Mn_3O_4, (c, d) $CaMnO_3$, and (e, f) ilmenite during continuous injection of (a, c, e) KCl or (b, d, f) NaCl. Colored areas mark stages with oxidizing (blue), inert (white) and reducing (orange) atmospheres.

when shifting to oxidizing conditions before a modest decrease is observed at the time of complete OC oxidation. This implies that the alkali uptake is affected by both the reduction and oxidation process of $CaMnO_3$ and the gas composition in the reactor.

Figure 5.16e and 5.16f displays the corresponding gas and alkali outlet concentrations from a fluidized bed of ilmenite during injection KCl and NaCl. The gas concentrations display significant differences compared to the two other OC materials. The reducing stage shows incomplete fuel conversion, where approximately 80% of the CO is converted to CO_2 in the beginning of the reduction, and 55% of the CO is converted to CO_2 towards the end of the reducing period. In oxidizing conditions, the ilmenite completely absorbs all ingoing O_2 during the initial 300 s, before the outlet O_2 concentration slowly increases as the OC oxidation proceeds. The time required for complete oxidation, i.e., at the time

when the outlet O_2 concentration equals the inlet concentration, is almost 1600 s which is considerably longer compared to the other two OC materials. The alkali concentrations are low indicating effective alkali uptake by the OC. A gradual increase in alkali concentration is observed during the reduction process and in the subsequent inert stage. The alkali concentration continue to rise during the OC oxidation process, once again implying less efficient alkali uptake during this process in agreement with the Mn_3O_4 observations. The alkali concentration peaks around the time when fractions of the introduced O_2 escapes the bed, followed by a gradual decrease over the remaining period of the oxidation stage. The observations indicate that the alkali uptake efficiency mostly depends on the oxidation state of the material, rather than the environmental conditions in the reactor.

To conclude, potassium and sodium salts of the same nature consistently exhibit qualitatively similar patterns in alkali signal throughout the redox cycle, implying substantial resemblances in how they interact with various types of OCs. Notably, a similar qualitative behavior is consistently evident during the oxidizing phase for all the OCs investigated, indicating a unique role of chlorine for the observed outcomes.

5.4.3 TMSI implementation to fluidized bed experiments

The total alkali concentrations presented in the fluidized bed experiments above are obtained with a SID operating at a constant filament temperature of 1100 °C (SID1 in Figure 3.2). Additional measurements on the alkali emissions leaving the reactor system were conducted with a second SID (SID2 in Figure 3.2), operating according to the previously described TMSI methodology (Section 5.1). SID2 was operated according to the TMSI procedure with subsequent cycles of three filament temperatures, 550 – 1100 – 800 – 1100 °C, with a time duration of 30 s at each temperature. The five-parameter information, *i.e.*, the steady state alkali signals at the three temperatures and the areas of the transient peaks, were calculated for each temperature cycle. The calculated data was used to determine the contributions of K^+ and Na^+ bound to Cl^-, OH^+, ${CO_3}^{2-}$ and ${SO_4}^{2-}$ to the flux from the reactor.

The fluidized bed experiment with $CaMnO_3$ during KOH injection is used to visualize how the TMSI method is implemented to the reactor experiments. Figure 5.17a shows the outlet alkali concentrations during one redox cycle measured with the two SIDs connected in parallel. The results display similar alkali signal intensities when both SIDs operates at the same filament temperature (1100 °C), and with large variations in measured alkali concentration in SID2 when the temperature is lowered. The filament temperature of SID2 shows excellent reproducibility between cycles, and the alkali signal intensity depends on both filament temperature and experimental conditions within the redox cycle.

The steady state alkali signals at 550, 800 and 1100 °C were calculated for each filament temperature cycle, along with the areas of the transient peaks that occur when increasing the filament temperature. Figure 5.17b summarize the values for these parameters for one temperature cycle, in the 2000-2150 s time interval that is marked by the black dotted lines

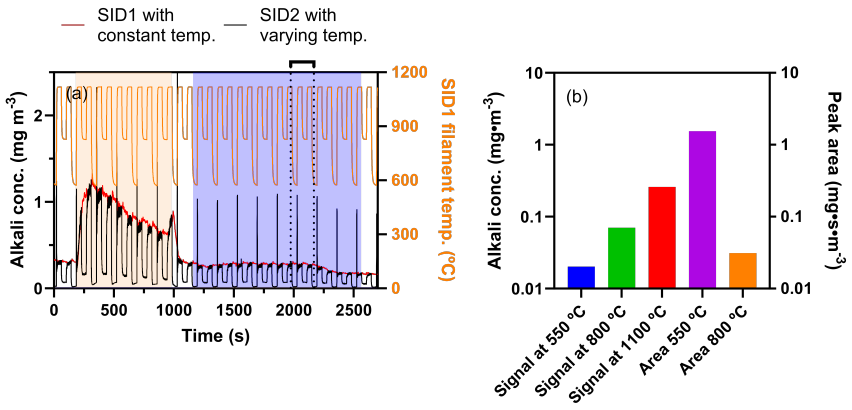

Figure 5.17: Results from one redox cycle with a 40 g $CaMnO_3$ OC fluidized bed at 900 °C and continuous injection of KOH. (a) Alkali concentration measured during constant SID operation (red line) and with the TMSI method (black line) with varying filament temperature (orange). Colored areas mark stages with oxidizing (blue), inert (white) and reducing (orange) atmospheres.(b) Values for the five experimental parameters from one filament temperature cycle, obtained at the time period marked by the dotted lines in panel (a).

in Figure 5.17a. The clear alkali signal at 550 °C indicate the presence of K-compounds, and the significantly higher alkali signal at 1100 °C compared to 800 °C suggests that the emissions are not dominated by alkali hydroxides (see Figure 5.4). While only the steady state alkali signals may correlate well with KCl, the transient peak that occurs when the filament temperature is raised from 800 to 1100 °C shows that it must be accompanied by some other alkali compounds (see Figure 5.4).

Each set of five experimental parameter values were fitted by a linear combination of the corresponding results for pure alkali salts (see Figure 5.4). The parameter values for the three steady state alkali signal intensities during the whole reactor experiment were scaled to give them equal weight in the fitting procedure. The absolute transient peak signals depend on the detailed experimental conditions including the selected length of the temperature modulation steps. Relative transient peak signals were therefore used in the present study and the data were scaled by global scaling parameters at 550 and 800 °C. The experimental results of the five parameters at each temperature cycle are displayed in Figure 5.18a together with the corresponding fits according to the model predictions. The model in general provides a good description of the experimental data with the only exception observed for the transient peak area in the 800-1100 °C temperature risebetween 500 and 825 s into the redox cycle. Figure 5.18b shows the combined fraction of each alkali salt compound in the alkali emissions obtain with the TMSI method.

The amount of alkali leaving the reactor during the complete redox cycle is approximately

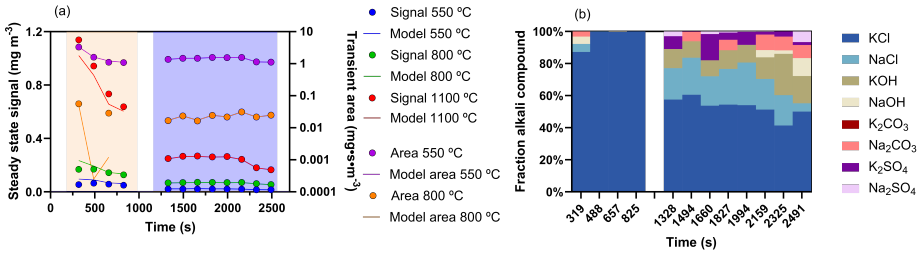

Figure 5.18: (a) The experimental data values (dots) from the experiment in Figure 5.17a and the corresponding values as predicted by the model (lines) for the five parameters of each temperature cycle in the SID. (b) Composition of the alkali emissions from the reactor exhaust gases predicted by the linear combination model for pure salt compounds.

30 μg, based on the observed alkali concentration measured by SID1 (Figure 5.17a) and a total gas flow rate of 1.5 Nl $\cdot$ min^{-1}. Based on a the BET specific surface area of 0.2 m^2 $\cdot$ g^{-1} for the calcium manganite OC [82], the total surface area of the 40 g fluidized bed is 8 m^2. This corresponds to approximately 5.8 $\cdot$ 10^{12} K atoms cm^{-2}, or around 0.006 monolayers (ML), assuming one complete ML consists of 1 $\cdot$ 10^{15} atoms cm^{-2} [159].

Although KOH is being injected, the TMSI method suggests that most of the alkali leaving the reactor is in the form of KCl (Figure 5.18b). This is not unreasonable since KCl(g) is a major release species at high temperature when K and Cl coexist [20, 85, 89]. The amount of alkali leaving the reactor is small compared to the approximately 3.8 mg KCl that were injected to the same fluidized bed prior to the KOH experiment. Nevertheless, the alkali speciation analysis suggests that the injected KOH is highly reactive with the calcium manganite, and that alkali mainly leaves the bed as KCl(g).

5.4.4 Speciation of released alkali compounds

The relative contributions of different alkali species for all alkali-OC combinations are summarized in Figure 5.19, displaying results for both reducing and oxidizing conditions. The experimental values in the analysis are average values obtained under stable reducing or oxidizing conditions.

When KCl is injected to the three types of OC beds, it is also the predominant alkali species in the outflow from the reactor under both oxidizing and reducing conditions. This aligns with expectations, as the introduced concentration of KCl is relatively high and alkali chlorides are known to be highly volatile and a major compound released during conversion of Cl-containing fuels [20, 28, 160]. The identification of minor contributions from other alkali compounds may be attributed to limitations in the speciation methodology rather than the actual formation of these compounds. Similarly, the results for NaCl injection

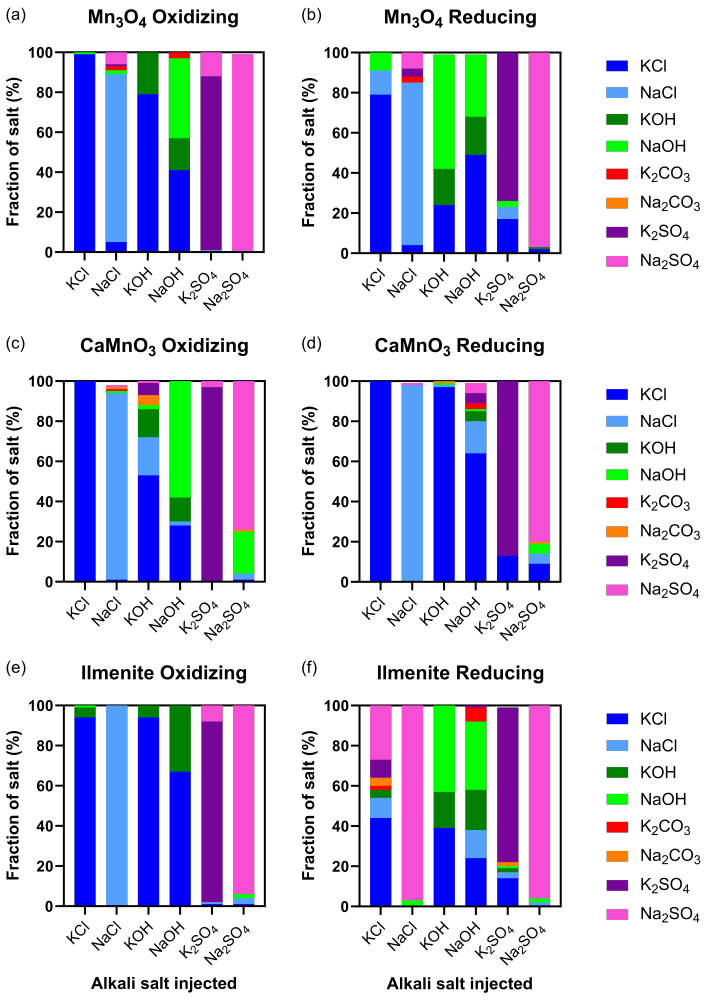

Figure 5.19: Percentage of each alkali compound leaving the reactor during experiments with fluidized beds of (a, b) Mn_3O_4, (c, d) $CaMnO_3$ and (e, f) ilmenite with continuous injection of either KCl, NaCl, KOH, NaOH, K_2SO_4 or Na_2SO_4 aerosol. Measurements were carried out in (a, c, e) oxidizing conditions and (b, d, f) reducing conditions. Adapted from **Paper VII**.

aligns with those of KCl injection. NaCl dominates in the outflow, and it is challenging to definitively confirm the presence of minor contributions from other compounds. The only exception occurs when ilmenite is subjected to reducing conditions, where Na_2SO_4 seems to dominate alkali emissions instead of NaCl. This may be due to limitations in the speciation methodology where two mixtures of alkali salts under unfavorable conditions

give similar results in the analysis.

Turning the attention to the cases involving the injection of K_2SO_4 and Na_2SO_4 into the fluidized beds. In both scenarios, the respective sulfate emerges as the primary alkali compound in the exhaust gases, and the analysis does not definitively establish significant contributions from other compounds.

However, the patterns observed for chlorides and sulfates are not replicated when it comes to alkali hydroxides. The exhaust gas seems to consist of a mixture of alkali compounds. Depending on the specific system, alkali hydroxides make minor contributions with noticeable variability, while substantial fractions of alkali chlorides can be observed. However, the low absolute alkali concentrations observed during experiments with alkali hydroxide injection (Figure 5.15) may impact the precision of the analysis. Conversely, hydroxides display a unique dependence on SID filament temperature, facilitating their differentiation from other alkali compounds in the speciation analysis (Figure 5.2). In conclusion, the release of alkali hydroxides from the OC fluidized beds included in this study appears to be of minor importance. Instead, the release of alkali compounds may be substantially affected by the presence of other counter-ions like Cl^- or $SO_4{}^{2-}$.

5.4.5 Discussion on alkali interactions with OC materials

The fluidized bed provides an extensive surface area for interactions between alkali and OC particles. It is probable that all introduced alkali molecules efficiently interact with the bed material, as indicated by instances of nearly complete alkali hydroxide uptake. These molecules initially adsorb to the OC surface and can undergo subsequent processes, such as dissociation, surface layer diffusion, bulk material diffusion, and association with new counter-ions, followed by eventual desorption. Notably, a large fraction of the introduced alkali compounds tends to form strong bonds with the OC, where it persists throughout the experiments.

The extent of alkali adsorption depends on the characteristics of the introduced alkali compounds and the OC materials. Sodium and potassium salts of the same type exhibit similar qualitative behavior, while the type of counter-ions (Cl^-, OH^-, and $SO_4{}^{2-}$) significantly influences the results. Alkali chloride injection results in the highest outlet alkali concentrations, followed by alkali sulfate experiments, with chlorides and sulfates dominating the exhaust when these salts are introduced. The presence of chlorine and sulfur compounds in the OC surface layers enhances the likelihood of recombination, leading to the formation of volatile compounds that can escape from the bed. In the case of alkali hydroxides, most of the injected alkali is absorbed by the OCs, with limited emissions (Figure 5.14). This suggests that adsorbed alkali hydroxides are less likely to escape from the OC particles, indicating reduced recombination and desorption once absorbed by the OC.

The observations indicate that alkali adsorption is affected by the specific chemical characteristics of the OC materials in both reducing and oxidizing conditions. For

manganese oxide, it exists in the form of Mn_3O_4 when oxidized, which is transformed into MnO when reduced [74]. The dependence of alkali uptake on gas composition for manganese oxide appears limited (illustrated in Figure 5.14a and 5.14b), suggesting that the MnO-Mn_3O_4 transition does not substantially affects the binding of alkali to the material. An exception is the obvious alkali peak that appears when the material reach full oxidation during alkali chloride injection (Figure 5.16a and 5.16b). However, a similar trend is observed with the other two OCs, and does not appear to be directly linked to the specific surface structure.

Regarding calcium manganate, it exhibits less efficient alkali uptake in reducing conditions compared to oxidizing conditions for all alkali salts. This implies that the oxygen deficiency of the material directly impact the stability of K and Na during the reduction process. However, there is no prior research on detailed interactions between alkali and calcium manganite. This material was analyzed with SEM-EDS in **Paper II**, before and after being used for fluidized bed experiments under reducing and oxidizing conditions with continuous KCl injection. Although some potassium was detected within the particles, there were no significant alterations in composition or morphology observed for the particles before and after being used in the reactor.

Ilmenite mineral has undergone extensive prior research, including investigations into alkali interactions [34, 36, 41, 67, 73]. The studies show that ilmenite effectively absorbs alkali during the combustion process, where K diffuse into the particles and form stable compounds with titanium oxides, such as $KTi_8O_{16.5}$ [36], while a concurrently outward migration of iron is observed [34]. This agrees with the low alkali concentrations observed in ilmenite experiments here, which indicates effective alkali uptake.

5.5 Online characterization of alkali release

Among the three materials covered in this thesis, ilmenite is by far the most applicable to CLC and OCAC, where several successful operations in commercial applications has been reported [34, 35, 48, 49, 61]. In fluidized bed experiments, ilmenite OC particles demonstrated significant alkali uptake, consistent with previous combustion-related studies [34, 36, 73]. This capacity to capture alkali as titanates is valuable in mitigating alkali-related issues like fouling, corrosion, and fluidized bed agglomeration. However, studies specifically focusing on alkali desorption from ilmenite are lacking. In a previous study involving the CLC of biomass using a mixture of calcium manganite and ilmenite as OC, significant alkali concentrations were reported in the flue gases from both the AR and FR [41]. This raises questions about the mechanisms responsible for transporting alkali from the FR to the AR. One possible explanation is that alkali was absorbed by the OC in the FR and subsequently released when the OC entered the AR, which typically operates at a higher temperature. Since most of the heat is extracted from the AR flue gases, understanding potential desorption mechanisms is crucial to prevent fouling and corrosion

on heat exchanger surfaces. Furthermore, if alkali can desorb under changing operational conditions, it could open up the possibility of regenerating the ilmenite material.

Therefore, the work continued by developing a method to characterize alkali desorption from OC particles. The method simultaneously monitor the alkali emissions and mass loss from fixed bed samples, and can be employed on various samples, including OC particles, solid fuels, or catalysts for gas reforming.

5.5.1 Development of the novel TGA-SID setup

The experimental set-up involves a SID connected to the exhaust of a commercial TGA, as illustrated in Figure 3.3. While each technique is established on its own, their integration requires careful consideration to ensure reliable results. As previously discussed, alkali compounds interact with surfaces in thermal conversion processes, and the same holds true within the TGA-SID setup. There are mainly two processes responsible for the alkali losses in the system. The first is loss of gaseous alkali to hot TGA walls due to molecular diffusion, and the second is loss of small aerosol particles to the walls of the cold exhaust tubes connecting the TGA with the SID.

The investigations related to the fluidized bed reactors highlight the importance of rapid transport of gaseous alkali species to surrounding walls. Estimates of the potential loss of alkali molecules in the TGA requires information about the temperature and gas flow profiles inside the TGA system. CFD simulations were used for a qualitative evaluation of the temperature gradients and the flow profiles in the employed TGA quartz reactor. The CFD simulations methodology is described in **Paper III**. The temperature and velocity profiles during TGA operation at 1000 °C with a 100 ml min^{-1} air flow are displayed in Figure 5.20. The temperature profile in Figure 5.20a shows that the quarts surface of the TGA compartment and gas outlet has temperatures between 850 and 1000 °C, while the sample holder reach the specified target temperature of 1000 °C. The velocity profile in Figure 5.20b shows that most of the gas flows over the sample holder and exits though the outlet tube without causing significant turbulence inside the main TGA compartment. The low degree of turbulence implies that most alkali interactions with hot walls would take place in the outlet tube.

The hot exhaust gases exit the TGA through a 4 mm inner diameter quartz tube with a length of 3 cm, before entering the cold exhaust tubes. Since alkali will be in the gas phase in this region, the alkali loss to the outlet tube walls may be calculated by the KPS method [153], as described in Section 5.2.3 and Eq. 5.5. Assuming all alkali will be in the form of KCl(g) at 900 °C temperature, the total transmission of alkali in the hot 3 cm tube section was estimated to 25%. Similar to the previous calculations with the KPS method, unity accommodation of molecules reaching the wall is assumed and the total distance travelled by each molecule equals the total tube length. Transmission calculations for alkali molecules through different tube lengths at different operating temperatures can be seen in **Paper III**.

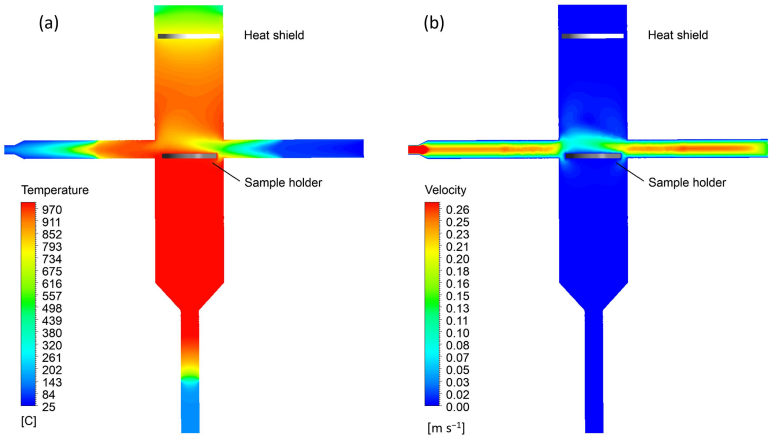

Figure 5.20: Results from CFD simulations of the TGA, operated at 1000 °C in air: (a) temperature profile and (b) velocity profile. Annotated in the figure is the position of a heat shield and the 11 mm wide platinum sample holder, that can be used as a dimension reference. Adapted from **Paper III**.

The reminder of the alkali that is not lost to the hot TGA walls will nucleate to form aerosol particles as the temperature decreases in the exhaust tube system. The exhaust tube system, connecting the SID to the TGA exhaust, comprise of a short metal tube and a slightly longer rubber tube. The loss of alkali aerosol particles to the inner tube walls was estimated by conducting experiments with different tube lengths. Figure 5.21 shows the observed alkali transmission as a function of tube length for metal (red) and rubber (blue) tubes. The figure shows relative values compared to a standard case, represented by a 18 cm metal tube length and a 21 cm rubber tube length. The alkali transmission is substantially influenced by the metal tube length, where the alkali transmission is 2.4 times higher compared to the standard case if the length of the metal tube is extrapolated to zero. Less pronounced is the effect of rubber tube length, where an extrapolation to length zero would result in 1.3 times higher transmission compared to the standard case. The observed alkali signal would be 3.2 times higher than the standard case if both tubes are reduced to zero length simultaneously.

In addition, the linear relationship between the alkali transmission and the tube lengths are consistent with the diffusional particle losses in a laminar flow. The penetration of particles through the tubes were calculated with the model described in Section 5.2.2, Eq. 5.1-5.4, where the diameter of aerosol particles was estimated based on the alkali concentration detected by the SID and an assumed particle number concentration of $5 \cdot 10^8$ cm^{-3} [86]. Although the model is simplified compared to actual conditions, it qualitatively describes the trends observed in the experiments. This confirms that the particle losses to the exhaust tubes can be explained by well-established aerosol science models.

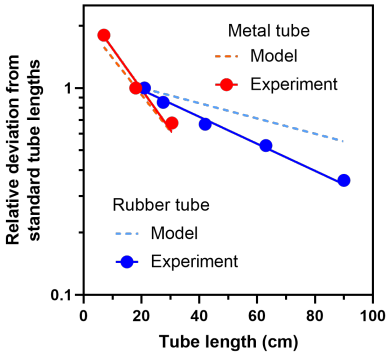

Figure 5.21: Relative alkali transmission through tubes connecting the TGA and SID as a function of tube length: metal tube (red symbols and line) and rubber tube (blue symbols and line). Results from a model for particle penetration [86] through tubes are included (dashed lines). Adapted from **Paper III**.

Combining the losses of alkali due to molecular diffusion in the hot TGA outlet with the loss of alkali particles in the cold exhaust tubes result in a total alkali transmission of 20^{+5}_{-4}% between the TGA sample and the SID. For further details, see **Paper III**.

5.5.2 Alkali desorption from used ilmenite

Although the alkali losses in the TGA-SID setup are significant, they can be understood and accounted for. With a suitable method in place, it was possible to characterize the desorption of alkali from ilmenite bed material previously used in an industrial scale OCAC system with biomass, shown in detain in **Paper IV**. The ilmenite was received from a 115 MW_{th} OCAC boiler after 225 h of biomass combustion [48, 49] and contains approximately 2 wt% K and 1 wt% Na, see Table 3.1. The ilmenite samples were exposed to temperatures up to 1000 °C under inert and oxidizing conditions in the TGA while the alkali release kinetics were characterized using the SID.

The results from 13 mg ilmenite samples are shown in Figure 5.22 (solid lines), where the effect of surrounding oxygen partial pressure is evaluated. The alkali emission profiles in Figure 5.22a shows a substantial alkali peak between 630 and 800 °C in both inert and oxidizing environments, which likely originates from loosely bound alkali on the surface of the particles. HHowever, no substantial mass loss is observed at this stage despite the large alkali peak, which demonstrates the high sensitivity of the SID. A second alkali release started as the temperature rose above approximately 900 °C and continued throughout the subsequent isothermal period. During the extended period with isothermal conditions at 1000 °C, both alkali release and mass loss profile decayed on a similar time scale in inert atmosphere, and the decay was approximately five times slower in oxidizing atmosphere.

Therefore, changes in sample properties depend on the oxygen activity of the surrounding atmosphere. In addition, Figure 5.22 also display the alkali desorption and mass loss profiles for reference ilmenite samples that were not utilized in the combustion process. The reference ilmenite lacks the early alkali desorption peak, and the release of alkali is restrained under isothermal conditions. This discrepancy strongly suggests that the alkali release observed from the OCAC ilmenite is a result of the alkali introduced to the material during biomass combustion, rather than an inherent property of the ilmenite material itself.

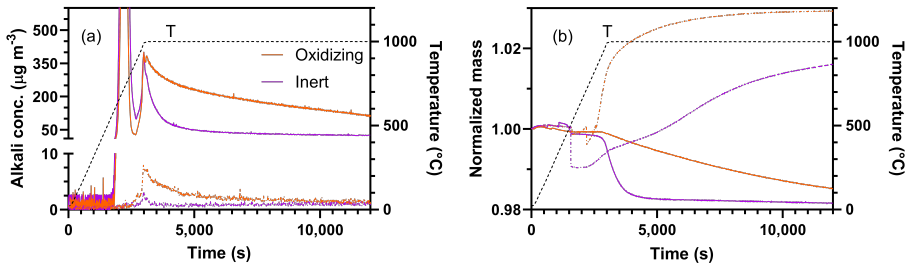

Figure 5.22: (a) Alkali desorption and (b) normalized mass loss profiles from samples of (solid lines) ilmenite particles that has been used during OCAC of biomass in a 115 MW_{th} power plant, and (dashed lines) unused reference ilmenite. Experiments were carried out under inert and oxidizing conditions at a heating rate of 20 °C · min^{-1} followed by an extended period at 1000 °C. Adapted from **Paper IV**.

By integrating the alkali release curves, a total alkali amount of 1.27 and 2.87 g · kg^{-1} sample was estimated to be released in inert and oxidizing conditions, respectively. Compared to a total alkali content of 27.8 g · kg^{-1} in the original sample, approximately 4.6 and 10.3 wt% of the available alkali was released in the inert and oxidizing TGA experiments, respectively. This agrees with the findings in a 100 kW CLC study where high alkali concentrations were detected in the flue gases leaving the AR [41], suggesting that ilmenite may release alkali in oxidizing environments.

Additional TGA-SID experiments were conducted with different sample amounts, varying from 0.5 to 20.3 mg, to evaluate the influence of sample size on alkali release. The results are displayed in detail in **Paper IV**, showing that the total alkali desorption increases with increasing sample size under both inert and oxidizing conditions. By normalizing the height of the alkali peak that takes place when reaching 1000 °C, it was seen that the decay in alkali concentration along the isotherm is steeper for smaller sample sizes. This indicated that the observed desorption kinetics at 1000 °C are influenced by the amount of sample used in the experiments.

5.5.3 Alkali desorption kinetics

Figure 5.23 displays the alkali desorption and mass loss profiles for two different sample sizes in inert and oxidizing atmospheres at a constant temperature of 1000 °C. The desorption profiles under isothermal conditions can be described by an exponential decay function:

$$I(t) = I_0 exp(-kt) \tag{5.8}$$

where $I(t)$ is the alkali intensity measured at time t, I_0 is the initial intensity and k is the rate constant of the exponential decay. Eq. 5.8 was used to determine the alkali desorption rate constant at 1000 °C, and the mass loss data are treated by a similar approach. Figure 5.23 includes exponential decay functions fitted to the experimental data from the point when the temperature has stabilized at 1000 °C and 5000 s onward, except for the mass loss profile in Figure 5.23b, which is fitted between 3000 – 3800 experimental time. Since a single exponential decay function can be used to represent the experimental data, the alkali desorption and mass loss follow first order kinetics. An exception is seen for the case in Figure 5.23b, showing a more linear dependence for weight, which would suggest zeroth order kinetics.

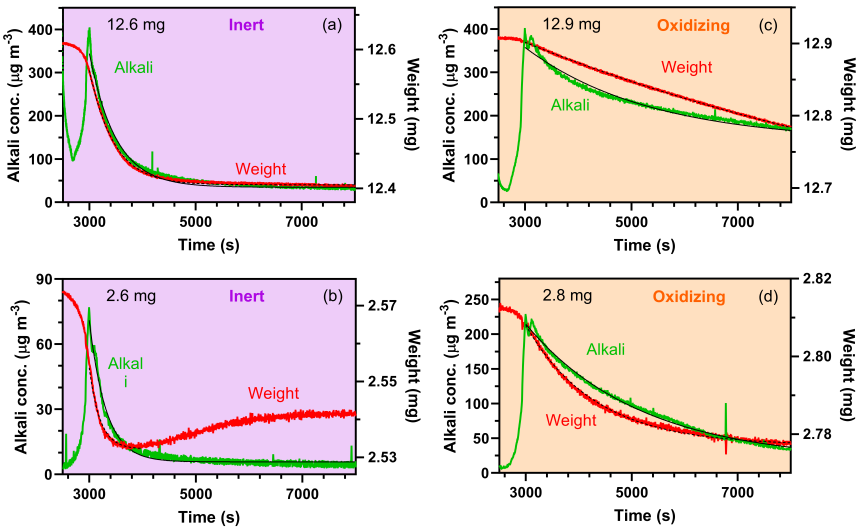

Figure 5.23: Profiles of alkali desorption (green lines) and sample mass loss (red lines) and their corresponding exponential decay functions (black solid and dashed lines, respectively) at a constant temperature of 1000 °C in (a and b) inert conditions and (c and d) oxidizing conditions. Adapted from **Paper IV**.

The corresponding procedure was applied to all investigated cases, and the resulting rate

constants are summarized in Table 5.1. Under inert conditions, smaller sample sizes result in increased rate constants for both alkali desorption and sample weight loss, except for the case with 0.5 mg. A similar trend is true for the rate constant for weight loss under oxidizing conditions, but no clear trend is observed for the alkali desorption rate constant. Furthermore, the rate constants for alkali desorption are 3-7 times higher under inert conditions compared to oxidizing conditions.

Table 5.1: Rate constants (k, in s^{-1}) for alkali desorption and sample weight loss at 1000 °C. Error limits are 95% confidence intervals. Adapted from **Paper IV**.

Sample	**Inert**		**Oxidizing**	
In/Ox (mg)	*Alkali* ($s^{-1} \cdot 10^{-5}$)	*Weight* ($s^{-1} \cdot 10^{-5}$)	*Alkali* ($s^{-1} \cdot 10^{-5}$)	*Weight* ($s^{-1} \cdot 10^{-5}$)
0.5	189 ± 4.0			
1.6/1.2	392 ± 5.9		74 ± 1.1	54 ± 1.8
2.6/2.8	317 ± 3.6	493 ± 6.7	46 ± 0.3	76 ± 0.5
7.4	222 ± 1.1	349 ± 1.6		
12.6/12.9	201 ± 1.4	217 ± 1.1	42 ± 0.5	10 ± 0.1
20.3	120 ± 0.4	185 ± 0.3		

Worth highlighting is the resemblance between the rate constants for alkali desorption and weight loss. This relationship implies that the alkali emissions are associated with alterations in the sample properties. However, the sample mass loss observed is significantly greater than the quantity of alkali that is released (where an integration of the alkali profile in Figure 5.22 shows that 2.6 μg alkali desorbs while 200 μg of mass is lost between 3000 and 5000 s under inert conditions). Therefore, the observed decline in mass cannot be attributed to alkali depletion alone; instead, the alkali desorption is likely influenced by the kinetics of the mass loss process.

Results from the experiments in inert atmosphere show that the rate constants for alkali and weight loss as a function of initial sample mass can be described by a linear dependence. By assuming a complete linear relationship, the rate constants for alkali desorption and weight loss equals $3.7 \cdot 10^{-3}$ s^{-1} and $5.0 \cdot 10^{-3}$ s^{-1}, respectively, when the regressions are extrapolated to zero mass. Greater sample sizes offer an expanded surface area for potential interactions with desorbed alkali, potentially resulting in alkali re-condensation on adjacent particle surfaces. This phenomenon could subsequently alter the observed desorption rate constants. Consequently, it is worth considering the desorption rates derived from the "zero mass" extrapolations as more indicative, as they account for the limited surface area available for "condensation-evaporation" processes.

The temperature dependence of the alkali desorption rate constant is described by the Arrhenius Eq. 4.4, which can be expressed as,

$$ln(k) = -\frac{E_a}{R} \cdot \frac{1}{T} + ln(A) \tag{5.9}$$

where E_a is the activation energy, R is the ideal gas constant, T is the temperature and A is a pre-exponential factor. To estimate the activation energy required for alkali

release, the alkali signal intensity can be analyzed as a function of temperature during the temperature ramp in the TGA. The alkali signal intensity, I, detected by the SID can be expressed in terms of the release rate of alkali, r, and an instrument-specific constant C:

$$I = C \cdot r = C \cdot k \cdot [Na, K]^n \tag{5.10}$$

where $[Na, K]$ is the alkali concentration available for desorption and C describes the effect of several experimental parameters, including the alkali losses and the SID function. By combining Eq. 5.9 and 5.10, the temperature dependence of the alkali signal intensity can be expressed as Eq. 5.11:

$$ln(I) = -\frac{E_a}{R} \cdot \frac{1}{T} + ln(A) + ln[Na, K] + ln(C) \tag{5.11}$$

Figure 5.24 displays the alkali signal intensity as a function of $1/T$ for experiments with 2.6 and 2.8 mg ilmenite samples in inert and oxidizing atmospheres, respectively. The solid black lines represent fits to the experimental data using Eq. 5.11.

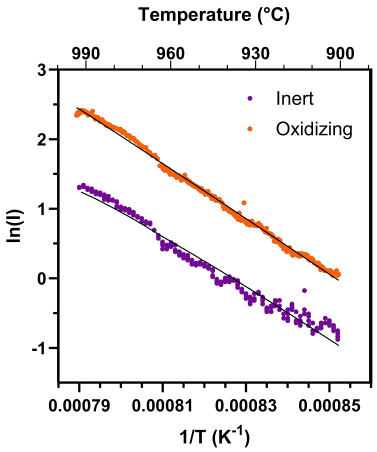

Figure 5.24: Logarithmic alkali signal intensity as a function of $1/T$ in the temperature ramp between 900 – 994 °C for ilmenite samples in inert and oxidizing conditions. Black lines show $ln(I)$ described by Eq.5.10. Adapted from **Paper IV**.

The Arrhenius parameters for both cases are presented in Table 5.2, together with the Arrhenius parameters for the other investigated samples. Under oxidizing conditions, both E_a and A increase as the sample mass decreases. The case involving the smallest sample mass (1.2 mg) exhibits a pre-exponential factor of $1 \cdot 10^{12.4 \pm 0.1}$ s^{-1}, which closely aligns with the typical value of $1 \cdot 10^{13}$ s^{-1} for a general first-order desorption process [161]. This suggests that the observed kinetics are primarily governed by the desorption process, and the determined activation energy of 378 ± 3 kJ $\cdot$ mol^{-1} may be attributed to the

binding energy between alkali and the ilmenite surface. Conversely, for larger sample sizes, the kinetics are influenced by re-condensation and evaporation within the samples, leading to lower E_a and A values. The trends are less distinct under inert conditions, with A values ranging between $1 \cdot 10^{11.0\pm0.1}$ s^{-1} and $1 \cdot 10^{10.4\pm0.1}$ s^{-1} and E_a values between 317 and 323 kJ $\cdot$ mol^{-1} across sample masses ranging from 1.6 to 7.4 mg. The smallest sample, 0.5 mg, appears to be an outlier due to noisy alkali signals and results in low A and E_a values. In contrast, the two largest samples generally exhibit low A and E_a values.

Table 5.2: Rate constants (k, in s^{-1}) for alkali desorption and sample weight loss at 1000 °C. Error limits are 95% confidence intervals. Adapted from **Paper IV**.

Sample	**Inert**		**Oxidizing**	
In/Ox (mg)	A (s^{-1})	E_a $(kJ \cdot mol^{-1})$	A (s^{-1})	E_a $(kJ \cdot mol^{-1})$
0.5	$1 \cdot 10^{7.5\pm0.4}$	250 ± 10		
1.6/1.2	$1 \cdot 10^{10.9\pm0.3}$	323 ± 7	$1 \cdot 10^{12.4\pm0.1}$	378 ± 3
2.6/2.8	$1 \cdot 10^{11.0\pm0.2}$	329 ± 6	$1 \cdot 10^{10.4\pm0.1}$	334 ± 2
7.4	$1 \cdot 10^{10.4\pm0.2}$	317 ± 5		
12.6/12.9	$1 \cdot 10^{5.9\pm0.2}$	209 ± 4	$1 \cdot 10^{7.9\pm0.1}$	275 ± 3
20.3	$1 \cdot 10^{6.3\pm0.3}$	224 ± 6		

There are three cases involving samples of similar masses that were investigated under both oxidizing and inert conditions. In most cases, both the pre-exponential factor (A) and activation energy (E_a) tend to be lower in the inert environment compared to the oxidizing environment.

Previous research on the interaction between ilmenite and biomass ashes has shown that K and Ca migrate inward to form products with titanium oxides, while Fe migrates outward [34]. The migration seems faster for K compared to Ca, and accumulation of Ca can be found on the surface of the ilmenite particles while the outer ash layer does not include K [36]. Less than 1 wt% of the total K-content in ilmenite can be leached, and it is believed that this corresponds to the K that had not yet formed the product KTi_8O_{16} [34].

Although a minor fraction of the available alkali desorbs from the ilmenite in the present study, the total desorption is more than twice as high under oxidizing conditions (10% of available alkali) compared to inert conditions (5% of available alkali). The TGA experiments reveal two distinct alkali desorption stages. The second high-temperature stage shows a clear environmental dependence with higher desorption rate in oxidizing atmosphere compared to an inert atmosphere. This aligns with a previous 100 kW CLC study, which detected substantial alkali concentrations after the AR [41], suggesting that ilmenite may release alkali in oxidizing conditions. The specific alkali responsible for desorption is not clearly identified, and future experiments could benefit from the use of the TMSI technique to differentiate between different alkali components in emissions.

5.5.4 TMSI implementation to TGA-SID experiments

In addition to studying alkali desorption from ilmenite particles, the TGA-SID setup was used to monitor the alkali emissions from solid biomass, included in **Paper VI**. In these experiments, the SID is operated according to the presented TMSI method in order to specify the alkali emissions. A biomass sample of 11.6 mg pine wood was placed on the TGA sample holder and heated at a rate of 10 °C · min^{-1} to 1000 °C, where it was kept at a constant temperature for an extended time. The TGA was operated under inert conditions with pure nitrogen, and alkali emissions were measured online in the exhaust gases with the TMSI method during simultaneous monitoring of the sample mass loss.

Figure 5.25a shows the alkali concentration during the experiment, together with the sample temperature and the SID filament temperature. Alkali is released in two main stages, the first at temperatures between 300 and 500 °C where the wood sample is pyrolyzed and the main sample mass loss occurs, and a second when temperature exceeds 850 °C, corresponding to alkali release from remaining char and ash. A minor peak in alkali release is also observed around 700 °C, which is tentatively attributed to changes in ash properties as the temperature is raised after the pyrolysis.

The observed alkali concentration in each filament temperature modulation cycle displays some interesting features during the different alkali release periods (Figure 5.25a). During the pyrolysis, a relatively strong SID signal is observed even at the lowest, 550 °C, filament temperature. This indicates that the alkali emissions contain a large fraction of potassium compounds, since sodium compounds produce low signals at this filament temperature (Figure 5.2). This agrees with trends observed in the transient peaks that occur when the filament temperature is increased. Large transient peaks are observed when temperature increases from 550 to 1100 °C, while the temperature shift between 800 and 1100 °C give rise to significantly smaller or no transient peaks, as expected for potassium compounds.

The alkali signal shows a different behavior at high sample temperatures (6000 s into the experiment of Figure 5.25a). Here, the alkali signal at 550 °C filament temperatures is low, and transient peaks are observed when the filament temperature is increased from both 550 and 800 to 1100 °C. Therefore, it is likely that the alkali emissions contain a significant fraction of sodium compounds.

In agreement with the previously described TMSI methodology, the steady state alkali signals at 550, 800 and 1100 °C were calculated for each filament temperature cycle, along with the areas of the transient peaks that occur when increasing the filament temperature. The absolute transient peak signals depend on the detailed experimental conditions including the length of the temperature modulation steps, and relative transient peak signals were therefore used in the present study and the data are scaled by two global scaling parameters at 550 and 800 °C, respectively. The results are displayed in 5.25b together with fits of the five experimental parameters based on the methodology described above. The model in general provides a good description of the experimental data. The

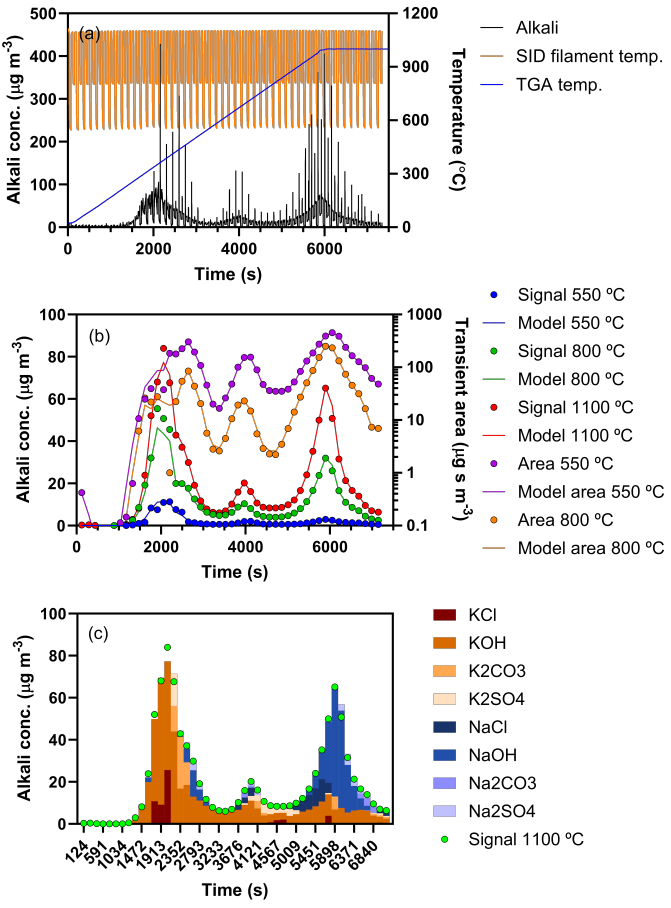

Figure 5.25: (a) Alkali signal (black), SID filament temperature (orange) and TGA temperature (blue) during biomass conversion under inert conditions with 10 °C · min^{-1} heating rate to 1000 °C. (b) The five factors of the SID signal with experimental data as dots and the corresponding values predicted by the model as lines. (c) Alkali concentration measured by the SID at 1100 °C filament temperature (green dots) and the alkali emission composition predicted by the model (bars). Adapted from **Paper VI**.

only exception is seen in the beginning of the time series before pyrolysis begins and the alkali signal is low.

Figure 5.25c shows the steady state alkali concentration measured at 1100 °C (green dots) together with the predicted composition of the alkali emissions. The model predictions are in accordance with the qualitative observations in Figure 5.25a, namely that the alkali

emissions during the pyrolysis stage are dominated by potassium compounds, mainly KOH and to a lesser extent KCl. A minor emission of NaOH is also identified during the later stage of the pyrolysis process. The potassium compounds continue to dominate as the sample temperature is increased above 550 °C. At temperatures above 700 °C, eemissions of NaOH become increasingly import and dominate at 1000 °C.

Averaged over the whole experiment, the alkali emissions consist of approximately 66% potassium and 34% sodium compounds. By integrating the alkali signal at 1100 °C, the total alkali emissions are 0.78 μg K and 0.42 μg Na, considering the 100 ml $\cdot$ min^{-1} flow rate through the TGA and assuming 20% total transmission of the alkali emissions between the TGA and the SID (see Section 5.5.1). Based on the 11.6 mg sample, 0.007 wt% K and 0.004 wt% Na is released from the wood, and the values are consistent with the initial sample concentrations of 0.034 wt% K and 0.011 wt% Na [138].

5.5.5 Material analysis on ilmenite particles

In addition to the alkali desorption experiments, **Paper IV** includes detailed material analyses on the ilmenite particles before and after the TGA experiments to determine the abundance and distribution of key elements in the OC.

Figure 5.26 illustrates the cross-section micrograph, along with corresponding chemical maps, of a broad area of the OCAC ilmenite sample prior to TGA experiments, to observe the overall trends in composition. Regions where Fe and Ti coexist have been identified as ilmenite ($FeTiO_3$) particles (Figure 5.26b and 5.26c). These ilmenite particles exhibit a significant presence of Ca, both internally and on their surfaces. The complete sample composition can be found in the table, highlighting Ca and Si as the predominant ash elements. Furthermore, there is an apparent overlap in the distribution of K, Al, and Si elements on some particles. Detailed point analyses conducted on several such particles display a molar ratio of approximately 1:1:3 for K:Al:Si, aligning closely with the composition of potassium feldspar ($KAlSi_3O_8$). It is worth noting that these silicates may have been present in the boiler system from the start, introduced through the fuel, and/or stemming from impurities within the ilmenite material. They most likely absorb K during the combustion process until they are saturated, whereafter they are assumed to remain stable and thus can be considered inert with respect to alkali in the TGA experiments.

Figure 5.27a shows a line scan analysis over the ash layer on an ilmenite particle and Figure 5.27b presents the corresponding elemental composition along the indicated arrow. The prominent elements include Ca, Fe and Ti, while Al, Si, K, and Na constitute minor elements. The composition profile shows that K is concentrated deeper into the particle, specifically at a depth of 11 μm, while Na exhibits higher concentrations at the surface of the particle. Furthermore, K is found at the interface between the ilmenite particle and an external ash layer characterized by its abundance of Ca. This observation aligns with previous research on ilmenite, as reported in references [36, 49].

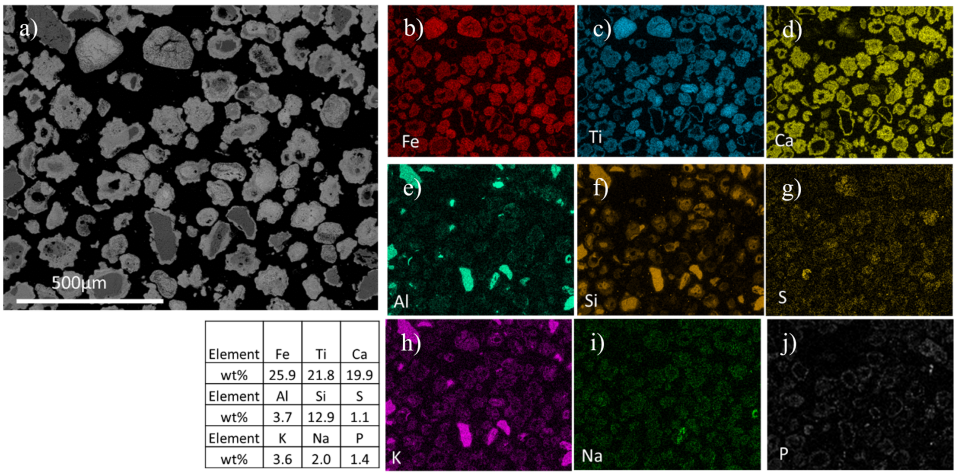

Element	Fe	Ti	Ca
wt%	25.9	21.8	19.9
Element	Al	Si	S
wt%	3.7	12.9	1.1
Element	K	Na	P
wt%	3.6	2.0	1.4

Figure 5.26: (a) Micrograph of the cross-section of ilmenite sample prior to TGA experiments. (b-j) Chemical maps of the major components of ilmenite (Fe and Ti), major ash elements (Ca, Si) along with Al, P and the alkali species (K and Na). The total content in weight percent is presented in the table (excluding C and O). Adapted from **Paper IV**.

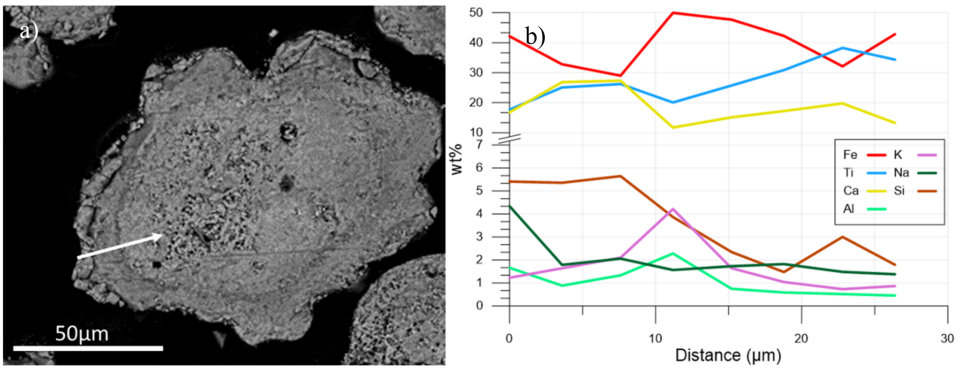

Figure 5.27: (a) Micrograph of the cross-section of ilmenite sample prior to TGA experiments. (b-j) Chemical maps of the major components of ilmenite (Fe and Ti), major ash elements (Ca, Si) along with Al, P and the alkali species (K and Na). The total content in weight percent is presented in the table (excluding C and O). Adapted from **Paper IV**.

Similar material analyses were conducted on ilmenite particles obtained after 10 h TGA experiments at 1000 °C under inert or oxidizing conditions. The results were similar for the particles received after inert and oxidizing conditions. Small spots of phosphate compounds, rich in P, Na and Ca, were found near the surface of the particle ash layer. However, since these phosphates were observed in particles prior to TGA experiments as

well, they are assumed to remain stable throughout the TGA experiments. The results align with recent thermodynamic analyses, investigating the fate of ash elements in ilmenite particles, showing that K is likely to form products of titanates while Na is more likely to form phosphates [67].

The outermost surface of the ilmenite particles before and after TGA experiments was also analyzed. The surface composition prior to TGA experiments is abundant in Fe, Ti and Ca, while Na and lower levels of K are also observed. The results further indicates that the alkali compounds may be present in the form of oxides, chlorides and sulfates. Previous x-ray photoelectron spectroscopy (XPS) studies on the same ilmenite material have reported similar results regarding the alkali composition on the outermost particle surface [35]. Interestingly, when comparing the surface composition of the particles before and after TGA experiments, higher Ca concentrations were found on the surface of the latter, with reduced levels of Fe and Ti. Additionally, another distinction between the particles pre- and post-TGA experiments is a reduced presence of S and Cl on the surface in the latter case. Based on these observations, it is plausible that alkali elements departed from the ilmenite sample in the form of alkali chlorides during the TGA experiments. As for the difference in sulfur content, it may be linked to the desorption of alkali sulfates, although a more probable explanation could be variations in the surface concentrations of $CaSO_4$ [61].

Additional material analysis were performed at a depth of 16 nm into the particle surface. While Cl are almost completely absent from the surface of particles after TGA experiments in both oxidizing and inert atmospheres, particles after inert experiments exhibit significantly higher Cl concentrations at 16 nm depth, compared to the particles after oxidizing experiments. This discrepancy suggests that alkali, along with Cl, may leave the sample from a deeper level under oxidizing conditions in contrast to the inert. This may involve diffusion either as alkali chlorides or they diffuse independently before eventually combining at the surface and desorbing. The observations align with the experimental data displayed in Figure 5.22, which illustrates a more significant release of alkali from the sample when subjected to oxidizing conditions.

5.6 Relevance to industrial applications

The outcomes of the presented research adds to the existing knowledge regarding the characteristics of alkali in biomass conversion applications. In CLC, involving interconnected air and fuel reactors, alkali is introduced into the FR alongside the fuel where a fraction of the alkali is released into the gas phase as a result of fuel conversion. According to the present findings, gaseous alkali is absorbed to varying degrees by fluidized beds composed of manganese oxide, calcium manganite and ilmenite. Furthermore, ilmenite samples containing K and Na release alkali to some extent under conditions relevant to CLC and other thermal conversion systems.

Ilmenite absorbs nearly all injected KCl, NaCl, KOH or NaOH in reducing conditions. In practical applications, this would lead to minimal alkali emissions in the flue gases exiting the FR. This substantial alkali uptake aligns with prior research, affirming that ilmenite effectively functions as an alkali scavenger [34, 36]. Nevertheless, the residence time of the OC material in the reactor used here is short in comparison to the lifespan of a bed in a commercial application [162]. Over extended operational periods, the alkali binding to the ilmenite may approach saturation. When compared to ilmenite, manganese oxide and calcium manganite permits a larger portion of the injected alkali to exit the FR.

The majority of heat extraction equipment in a CLC application is typically positioned within the gas stream exiting the exothermic AR [15], which also operates with substantially higher gas flow rates compared to the FR [14, 16, 163]. Therefore, it is preferred to have higher alkali concentrations in the flue gas stream from the FR, while minimizing the release of corrosive alkali compounds from the AR. Although alkali is introduced to the FR side along with the fuel, significant portions of the alkali may be transferred over to the AR side. This transfer can occur in the form of solid ash particles or by alkali adhering to the surface of OC particles [41]. The high absorption of the injected alkali by ilmenite and calcium manganite in oxidizing conditions is, therefore, beneficial with regard to CLC operation. In comparison, significantly lower alkali absorption is observed for manganese oxide in oxidizing conditions. It should be noted that the experiments involving alkali uptake characteristics are carried out with continuous alkali injection to OC beds which do not contain significant fractions of alkali. In a real system, the main source of alkali originates from the fuel under reducing conditions to OC materials which may already contain considerable amounts of alkali.

The studied alkali desorption profiles show that ilmenite containing 2 wt% K and 1 wt% Na releases alkali at temperatures above 900 °C. The AR in a CLC system generally operates at temperatures up to 1050 °C in an oxidizing atmosphere [164]. The alkali desorption studies show that alkali-containing ilmenite releases alkali at temperatures relevant for CLC with higher desorption in oxidizing atmosphere (relevant for AR) compared to inert atmosphere (conditions relevant for the loop-seals in a CLC process). Nevertheless, merely 10 wt% and 5 wt% of the total available alkali was able to desorb from the ilmenite particles during an extensive time period at 1000 °C in oxidizing and inert atmosphere, respectively.

In summary, these investigations indicate that ilmenite is superior in terms of reducing gaseous alkali concentrations when compared to calcium manganite and manganese oxide. Conversely, calcium manganite and manganese oxide demonstrate higher fuel conversion and oxidizing efficiency in comparison. The accumulation of alkali by the ilmenite may potentially enhance fuel conversion due to the catalytic properties of alkali [87], which was not investigated in this study. Furthermore, the minor amount of alkali desorbing from alkali-containing ilmenite particles under inert and oxidizing conditions may be mitigated further by a more frequent bed replacement, reducing the amount of accumulated alkali in the material.

6

Conclusions and Outlook

The work in this thesis includes the development of novel alkali monitoring techniques and laboratory reactor systems to study the uptake and release characteristics of different alkali compounds by OC materials commonly used in CLC. A combination of experimental investigations and CFD simulations led to an improved understanding regarding the behavior of alkali compounds in high temperature environments. This enabled groundbreaking studies related to the interactions between gaseous alkali compounds and solid OC particles.

This work presents a novel way to operate the SID, based on repeated temperature modulation of the platinum filament which is used to ionize alkali. It was seen that the alkali signal intensity measured in the SID at different temperatures, and the transient signals produced when raising the filament temperature, depend on the molecular composition of the alkali species. By comparing the unique temperature dependence in the alkali signal for a variety of pure salt compounds, with corresponding measured signals in reactor experiments, it was possible to determine the contributions of K^+ and Na^+ bound to Cl^-, OH^-, CO_3^{2-} and SO_4^{2-} to the flux from different reactor systems. The functionality was further demonstrated by quantifying the alkali emissions from a sample of solid biomass.

The work investigated the interactions between alkali compounds and the inner walls of a stainless steel reactor, which is considered a standard set-up for fluidized bed studies on laboratory-scale. The alkali experiments in the empty reactor showed that wall interactions are extensive and require careful consideration when studying alkali processes in thermal conversion applications. The introduction and sampling of alkali can be done in a controlled way by using alkali in the form of aerosol particles. However, the actual amount of alkali interacting with a fluidized bed is to a large extent influenced by the accessibility and surface properties of the surrounding hot reactor walls. Extensive areas with hot reactor walls above and below the location of a fluidized bed may obscure the signature of alkali interactions with the bed particles.

The obvious outcome of the initial studies was that the reactor configuration could be improved considerably with regard to mitigating alkali losses in the system. A novel laboratory reactor configuration was developed based on a combination of fundamental understanding of alkali processes at high temperatures and CFD simulations. The experimental set-up of the novel reactor facilitates continuous alkali injection to the reactor system, where the operational parameters can be changed to study their effects on the interactions between gaseous alkali and a fluidized bed of solid particles. The

development of the novel reactor opened up for detailed studies of alkali-OC interactions under different operational conditions.

The work also included developing a method to characterize alkali emissions and mass loss from small fixed bed samples by employing interconnected TGA and SID instruments. The method can be applied to monitor the real-time alkali release and mass loss from a large variety of samples, including OC particles and biomass, under well-controlled atmospheric conditions and temperatures. The development included quantifying the losses of alkali in the system that arise due to molecular diffusion in hot zones and aerosol particle losses in sampling lines. Although the alkali losses were found to be significant, they could be understood and accounted for and the experimental observations aligned with modeling estimates. The technique was deemed well-suited for characterizing alkali emissions by temperature and conducting kinetics studies under isothermal conditions. The functionality was demonstrated using biomass and ilmenite OC samples from an industrial process.

Experiments were carried out to evaluate the interactions between different alkali salt compounds and three different OC materials used in CLC of biomass. Alkali desorption experiments in the TGA-SID set-up shows that ilmenite samples used for OCAC of biomass release alkali in both inert and oxidizing environments at high temperatures and kinetics were characterized. The total desorption is more than twice as large under oxidizing conditions compared to inert conditions (10 wt% and 5 wt% of the available alkali amount respectively). Material analyses showed some K and significant amounts of Na on the outermost surface of the ilmenite particles, and both concentrations decreased, together with Cl, during TGA experiments. Alkali uptake experiments, where KCl, NaCl, KOH, NaOH, K_2SO_4 and Na_2SO_4 were fed to a fluidized bed of calcium manganite, ilmenite or manganese oxide particles at 900 °C under reducing, inert and oxidizing conditions showed efficient uptake of alkali by the OC materials. The key findings can be summarized as follows:

- The type of OC material plays a crucial role in alkali uptake, with calcium manganite, manganese oxide, and ilmenite exhibiting varying levels of efficiency depending on the gas conditions. Among them, ilmenite showed near-complete absorption of alkali, especially during reducing conditions, making it a promising option for limiting alkali emissions.

- The alkali speciation analysis revealed that NaCl and KCl were the predominant alkali species emitted during NaCl and KCl injection. Likewise, alkali sulfates were the dominating species during alkali sulfate injection, while alkali hydroxide injection resulted in low emissions dominated by alkali hydroxides and chlorides.

- Furthermore, the study highlights the trade-off between alkali absorption efficiency and fuel conversion/oxidizing efficiency of the OC materials. While ilmenite demonstrated excellent alkali uptake, manganese oxide and calcium manganite exhibited superior fuel conversion and oxidizing efficiency.

Overall, the work in this thesis demonstrate the complex behavior of alkali in a CLC process, influenced by factors such as gas conditions, OC material, and alkali salt composition. The development of novel reactor systems and alkali speciation methods, together with experimental investigations on the interactions between alkali compounds and OC, contribute to a deeper understanding of alkali behavior in biomass thermal conversion systems and provide valuable insights for the design and optimization of CLC processes. Several future experiments could be helpful to develop a deeper understanding of the alkali processes that are discussed in this thesis. Regarding alkali desorption studies, maybe the most interesting for CLC would be to conduct TGA experiments in reducing atmospheres to resemble the conditions in a FR. Additional experiments with different heating rates could provide valuable information related to the kinetic parameters and employing the developed TMSI method could provide value information regarding the composition of the desorbed alkali. Further development of the TMSI method could focus on optimization of time resolution and selectivity of the speciation method under conditions of relevance to thermal conversion, including both laboratory and field studies. Future research regarding alkali uptake characteristics by OC fluidized beds could explore the long-term performance of OC materials and further investigate the catalytic effects of alkali on fuel conversion. Detailed material analyses on OCs that has been exposed to different alkali salts could provide valuable information regarding the alkali distribution within the samples and possible reaction products.

Bibliography

[1] IEA. Key world energy statistics 2021, 2021.

[2] Intergovernmental Panel on Climate Change, Climate Change 2014: Mitigation of Climate Change: Working Group III Contribution to the IPCC Fifth Assessment Report. Report 9781107058217, Cambridge University Press, 2015.

[3] Intergovernmental Panel on Climate Change, Climate Change 2021 – The Physical Science Basis: Working Group I Contribution to the Sixth Assessment Report of the Intergovernmental Panel on Climate Change. Report, Cambridge, 2023.

[4] UNFCCC. Convention on Climate Change: Climate Agreement of Paris, 2018.

[5] UNFCCC. Decision-/COP26 Glasgow Climate Pact.

[6] IEA. CO_2 emissions in 2022. Report, 2023.

[7] R. Stuart Haszeldine. Carbon capture and storage: How green can black be? *Science*, 325(5948):1647, 2009.

[8] Filip Johansson, Jan Kjärstad, and Mikael Odenberger. The importance of CO_2 capture and storage: A geopolitical discussion. *Thermal Science*, 16(3):655–668, 2012.

[9] Bert Metz, Ogunlade Davidson, Helen de Coninck, Manuela Loos, Leo Meyer, and (Eds.). IPCC Special Report on Carbon Dioxide Capture and Storage. Report, Prepared by Working Group III of the Intergovernmental Panel on Climate Change, 2005.

[10] T. Gasser, C. Guivarch, K. Tachiiri, C. D. Jones, and P. Ciais. Negative emissions physically needed to keep global warming below 2°C. *Nature Communications*, 6(1):7958, 2015.

[11] Change Intergovernmental Panel on Climate. *Climate Change 2022 – Impacts, Adaptation and Vulnerability: Working Group II Contribution to the Sixth Assessment Report of the Intergovernmental Panel on Climate Change*. Cambridge University Press, Cambridge, 2023.

[12] Pete Smith, Steven J. Davis, Felix Creutzig, Sabine Fuss, Jan Minx, Benoit Gabrielle, and et al. Biophysical and economic limits to negative CO_2 emissions. *Nature Climate Change*, 6(1):42–50, 2016.

[13] Stephen Smith, Oliver Geden, Gregory Nemet, Matthew Gidden, William Lamb, Carter Powis, and et al. *The State of Carbon Dioxide Removal - 1st Edition*. 2023.

[14] Anders Lyngfelt, Bo Leckner, and Tobias Mattisson. A fluidized-bed combustion process with inherent CO_2 separation; application of chemical-looping combustion. *Chemical Engineering Science*, 56(10):3101–3113, 2001.

[15] Anders Lyngfelt. Chemical looping combustion: Status and development challenges. *Energy & Fuels*, 34(8):9077–9093, 2020.

[16] Anders Lyngfelt and Bo Leckner. A 1000MWth boiler for chemical-looping combustion of solid fuels – Discussion of design and costs. *Applied Energy*, 157:475–487, 2015.

[17] Lin Zhu, Yangdong He, Luling Li, and Pengbin Wu. Tech-economic assessment of second-generation CCS: Chemical looping combustion. *Energy*, 144:915–927, 2018.

[18] Edward M. W. Smeets and André P. C. Faaij. The impact of sustainability criteria on the costs and potentials of bioenergy production – applied for case studies in brazil and ukraine. *Biomass and Bioenergy*, 34(3):319–333, 2010.

[19] Helmut Haberl, Tim Beringer, Sribas C. Bhattacharya, Karl-Heinz Erb, and Monique Hoogwijk. The global technical potential of bio-energy in 2050 considering sustainability constraints. *Current Opinion in Environmental Sustainability*, 2(5):394–403, 2010.

[20] Maria Zevenhoven, Patrik Yrjas, and Mikko Hupa. *Ash-Forming Matter and Ash-Related Problems*, volume 4. 2010.

[21] Samsudin Anis and Z. A. Zainal. Tar reduction in biomass producer gas via mechanical, catalytic and thermal methods: A review. *Renewable and Sustainable Energy Reviews*, 15(5):2355–2377, 2011.

[22] Junqin Yu, Qinghua Guo, Yan Gong, Lu Ding, Jiajian Wang, and Guangsuo Yu. A review of the effects of alkali and alkaline earth metal species on biomass gasification. *Fuel Processing Technology*, 214:106723, 2021.

[23] Keiichirou Mitsuoka, Shigeya Hayashi, Hiroshi Amano, Kenji Kayahara, Eiji Sasaoaka, and Md Azhar Uddin. Gasification of woody biomass char with CO_2: The catalytic effects of K and Ca species on char gasification reactivity. *Fuel Processing Technology*, 92(1):26–31, 2011.

[24] Juntao Wei, Xudong Song, Qinghua Guo, Lu Ding, Kunio Yoshikawa, and Guangsuo Yu. Reactivity, Synergy, and Kinetics Analysis of CO_2 Co-pyrolysis/Co-gasification of Biomass after Hydrothermal Treatment and Coal Blends. *Energy & Fuels*, 34(1):294–303, 2020.

[25] Toshimitsu Suzuki, Hiroshi Nakajima, Na-oki Ikenaga, Hirokazu Oda, and Takanori Miyake. Effect of mineral matters in biomass on the gasification rate of their chars. *Biomass Conversion and Biorefinery*, 1(1):17–28, 2011.

[26] Oskar Karlström, Meheretu Jaleta Dirbeba, Mario Costa, Anders Brink, and Mikko Hupa. Influence of K/C Ratio on Gasification Rate of Biomass Chars. *Energy & Fuels*, 32(10):10695–10700, 2018.

[27] Marcus Öhman, Anders Nordin, Bengt-Johan Skrifvars, Rainer Backman, and Mikko Hupa. Bed agglomeration characteristics during fluidized bed combustion of biomass fuels. *Energy & Fuels*, 14(1):169–178, 2000.

[28] A. A. Khan, W. de Jong, P. J. Jansens, and H. Spliethoff. Biomass combustion in fluidized bed boilers: Potential problems and remedies. *Fuel Processing Technology*, 90(1):21–50, 2009.

[29] Ivana Staničić, Viktor Andersson, Malin Hanning, Tobias Mattisson, Rainer Backman, and Henrik Leion. Combined manganese oxides as oxygen carriers for biomass combustion — ash interactions. *Chemical Engineering Research and Design*, 149:104–120, 2019.

[30] Ulrich Kleinhans, Christoph Wieland, Flemming J. Frandsen, and Hartmut Spliethoff. Ash formation and deposition in coal and biomass fired combustion systems: Progress and challenges in the field of ash particle sticking and rebound behavior. *Progress in Energy and Combustion Science*, 68:65–168, 2018.

[31] Simone C. van Lith, Violeta Alonso-Ramírez, Peter A. Jensen, Flemming J. Frandsen, and Peter Glarborg. Release to the gas phase of inorganic elements during wood combustion. part 1: Development and evaluation of quantification methods. *Energy & Fuels*, 20(3):964–978, 2006.

[32] J. Lehmusto and P. And. Reactions of potassium chloride with chromium as a first step towards high temperature corrosion in biomass combustion. 2019.

[33] Pouya H. Moud, Klas J. Andersson, Roberto Lanza, Jan B. C. Pettersson, and Klas Engvall. Effect of gas phase alkali species on tar reforming catalyst performance: Initial characterization and method development. *Fuel*, 154:95–106, 2015.

[34] Angelica Corcoran, Jelena Marinkovic, Fredrik Lind, Henrik Thunman, Pavleta Knutsson, and Martin Seemann. Ash properties of ilmenite used as bed material for combustion of biomass in a circulating fluidized bed boiler. *Energy & Fuels*, 28(12):7672–7679, 2014.

[35] Ivana Staničić, Tobias Mattisson, Rainer Backman, Yu Cao, and Magnus Rydén. Oxygen carrier aided combustion (OCAC) of two waste fuels - Experimental and theoretical study of the interaction between ilmenite and zinc, copper and lead. *Biomass and Bioenergy*, 148:106060, 2021.

[36] A. Corcoran, P. Knutsson, F. Lind, and H. Thunman. Mechanism for migration and layer growth of biomass ash on ilmenite used for oxygen carrier aided combustion. *Energy and Fuels*, 32(8):8845–8856, 2018.

[37] Hari C. Mantripragada, Haibo Zhai, and Edward S. Rubin. Boundary Dam or Petra Nova – Which is a better model for CCS energy supply? *International Journal of Greenhouse Gas Control*, 82:59–68, 2019.

[38] Lars Strömberg, Göran Lindgren, Jürgen Jacoby, Rainer Giering, Marie Anheden, Uwe Burchhardt, Hubertus Altmann, Frank Kluger, and Georg-Nikolaus Stamatelopoulos. Update on Vattenfall's 30 MWth oxyfuel pilot plant in Schwarze Pumpe. *Energy Procedia*, 1(1):581–589, 2009.

[39] Haiming Gu, Laihong Shen, Jun Xiao, Siwen Zhang, and Tao Song. Chemical looping combustion of biomass/coal with natural iron ore as oxygen carrier in a continuous reactor. *Energy & Fuels*, 25(1):446–455, 2011.

[40] T. Mendiara, A. Abad, L. F. de Diego, F. García-Labiano, P. Gayán, and J. Adánez. Biomass combustion in a CLC system using an iron ore as an oxygen carrier. *International Journal of Greenhouse Gas Control*, 19:322–330, 2013.

[41] Ivan Gogolev, Carl Linderholm, Dan Gall, Matthias Schmitz, Tobias Mattisson, Jan B. C. Pettersson, and Anders Lyngfelt. Chemical-looping combustion in a 100 kW unit using a mixture of synthetic and natural oxygen carriers - Operational results and fate of biomass fuel alkali. *International Journal of Greenhouse Gas Control*, 88:371–382, 2019.

[42] Ivan Gogolev, Toni Pikkarainen, Juho Kauppinen, Carl Linderholm, Britt-Marie Steenari, and Anders Lyngfelt. Investigation of biomass alkali release in a dual circulating fluidized bed chemical looping combustion system. *Fuel*, 297:120743, 2021.

[43] I. Adanez-Rubio, A. Abad, P. Gayan, L. F. de Diego, F. Garcia-Labiano, and J. Adanez. Biomass combustion with CO_2 capture by chemical looping with oxygen uncoupling (CLOU). *Fuel Processing Technology*, 124:104–114, 2014.

[44] J. C. Abanades, B. Arias, A. Lyngfelt, T. Mattisson, D. E. Wiley, H. Li, M. T. Ho, E. Mangano, and S. Brandani. Emerging CO_2 capture systems. *International Journal of Greenhouse Gas Control*, 40:126–166, 2015.

[45] Xiao Zhao, Hui Zhou, Vineet Singh Sikarwar, Ming Zhao, Ah-Hyung A. Park, Paul S. Fennell, Laihong Shen, and Liang-Shih Fan. Biomass-based chemical looping technologies: the good, the bad and the future. *Energy & Environmental Science*, 10(9):1885–1910, 2017.

[46] Avishek Goel, Elyas M. Moghaddam, Wen Liu, Chao He, and Jukka Konttinen. Biomass chemical looping gasification for high-quality syngas: A critical review and technological outlooks. *Energy Conversion and Management*, 268:116020, 2022.

[47] Henrik Thunman, Fredrik Lind, Claes Breitholtz, Nicolas Berguerand, and Martin Seemann. Using an oxygen-carrier as bed material for combustion of biomass in a 12-MWth circulating fluidized-bed boiler. *Fuel*, 113:300–309, 2013.

[48] Patrick Moldenhauer, Angelica Gyllén, Henrik Thunman, and Fredrik Lind. A Scale-Up Project for Operating a 115 MWth Biomass-Fired CFB boiler with Oxygen Carriers as Bed Material. In *Proceeding of the 5th International Conference on Chemical Looping*.

[49] Angelica Gyllén, Pavleta Knutsson, Fredrik Lind, and Henrik Thunman. Magnetic separation of ilmenite used as oxygen carrier during combustion of biomass and the effect of ash layer buildup on its activity and mechanical strength. *Fuel*, 269:117470, 2020.

[50] Fredrik Lind, Angelica Corcoran, Bengt Andersson, and Henrik Thunman. 12,000 Hours of Operation with Oxygen-Carriers in Industrially Relevant Scale (75,000 kWth).

[51] Hugo S. Caram, Ramesh Gupta, Hans Thomann, Fan Ni, Simon C. Weston, and Mobae Afeworki. A simple thermodynamic tool for assessing energy requirements for carbon capture using solid or liquid sorbents. *International Journal of Greenhouse Gas Control*, 97:102986, 2020.

[52] Henrik Leion, Tobias Mattisson, and Anders Lyngfelt. The use of petroleum coke as fuel in chemical-looping combustion. *Fuel*, 86(12):1947–1958, 2007.

[53] David Sutton, Brian Kelleher, and Julian R. H. Ross. Review of literature on catalysts for biomass gasification. *Fuel Processing Technology*, 73(3):155–173, 2001.

[54] Tobias Mattisson, Anders Lyngfelt, and Henrik Leion. Chemical-looping with oxygen uncoupling for combustion of solid fuels. *International Journal of Greenhouse Gas Control*, 3(1):11–19, 2009.

[55] Henrik Leion, Tobias Mattisson, and Anders Lyngfelt. Using chemical-looping with oxygen uncoupling (CLOU) for combustion of six different solid fuels. *Energy Procedia*, 1(1):447–453, 2009.

[56] Tobias Mattisson, Henrik Leion, and Anders Lyngfelt. Chemical-looping with oxygen uncoupling using CuO/ZrO_2 with petroleum coke. *Fuel*, 88(4):683–690, 2009.

[57] A. Lyngfelt. Oxygen carriers for chemical looping combustion - 4 000 h of operational experience. *Oil & Gas Science and Technology - Revue d'IFP Energies nouvelles*, 66(2):161–172, 2011.

[58] Magnus Rydén, Malin Hanning, Angelica Corcoran, and Fredrik Lind. Oxygen Carrier Aided Combustion (OCAC) of Wood Chips in a Semi-Commercial Circulating Fluidized Bed Boiler Using Manganese Ore as Bed Material. *Applied Sciences*, 6(11):347, 2016.

[59] Oscar Condori, Francisco García-Labiano, Luis F. de Diego, María T. Izquierdo, Alberto Abad, and Juan Adánez. Biomass chemical looping gasification for syngas production using ilmenite as oxygen carrier in a 1.5 kWth unit. *Chemical Engineering Journal*, 405:126679, 2021.

[60] Fredrik Lind, Nicolas Berguerand, Martin Seemann, and Henrik Thunman. Ilmenite and nickel as catalysts for upgrading of raw gas derived from biomass gasification. *Energy & Fuels*, 27(2):997–1007, 2013.

[61] Ivana Staničić, Emil Ola Lidman Olsson, Hao Wu, Peter Glarborg, Iñaki Adánez-Rubio, Henrik Leion, and Tobias Mattisson. Investigating the interaction between ilmenite and zinc for chemical looping. *Energy & Fuels*, 37(11):7856–7870, 2023.

[62] Sebastian Sundqvist, Nazli Khalilian, Henrik Leion, Tobias Mattisson, and Anders Lyngfelt. Manganese ores as oxygen carriers for chemical-looping combustion (CLC) and chemical-looping with oxygen uncoupling (CLOU). *Journal of Environmental Chemical Engineering*, 5(3):2552–2563, 2017.

[63] V. Purnomo, F. Hildor, P. Knutsson, and H. Leion. Interactions between potassium ashes and oxygen carriers based on natural and waste materials at different initial oxidation states. *Greenhouse Gases-Science and Technology*, 2023.

[64] F. Hildor, T. Mattisson, C. Linderholm, and H. Leion. Metal impregnation on steel converter slag as an oxygen carrier. *Greenhouse Gases-Science and Technology*, 2023.

[65] Marcus Johansson, Tobias Mattisson, and Anders Lyngfelt. Comparison of oxygen carriers for chemical-looping combustion. *Thermal Science - THERM SCI*, 10:93–107, 2006.

[66] J. Adánez, L. F. de Diego, F. García-Labiano, P. Gayán, A. Abad, and J. M. Palacios. Selection of oxygen carriers for chemical-looping combustion. *Energy & Fuels*, 18(2):371–377, 2004.

[67] Ivana Staničić, Joakim Brorsson, Anders Hellman, Tobias Mattisson, and Rainer Backman. Thermodynamic analysis on the fate of ash elements in chemical looping combustion of solid fuels-iron-based oxygen carriers. *Energy & Fuels*, 36(17):9648–9659, 2022.

[68] Felicia Störner, Fredrik Lind, and Magnus Rydén. Oxygen carrier aided combustion in fluidized bed boilers in sweden—review and future outlook with respect to affordable bed materials. *Applied Sciences*, 11(17):7935, 2021.

[69] D. Bhogeswara Rao and M. Rigaud. Kinetics of the oxidation of ilmenite. *Oxidation of Metals*, 9(1):99–116, 1975.

[70] Jianbo Zhang, Qingshan Zhu, Zhaohui Xie, Chao Lei, and Hongzhong Li. Morphological changes of panzhihua ilmenite during oxidation treatment. *Metallurgical and Materials Transactions B*, 44, 2013.

[71] Hongsheng Chen, Zhong Zheng, Zhiwei Chen, and Xiaotao Bi. Reduction of Hematite (Fe_2O_3) to Metallic Iron (Fe) by CO in a Micro Fluidized Bed Reaction Analyzer: A Multistep Kinetics Study. *Powder Technology*, 2017.

[72] Juan Adánez, Ana Cuadrat, Alberto Abad, Pilar Gayán, Luis F. de Diego, and Francisco García-Labiano. Ilmenite activation during consecutive redox cycles in chemical-looping combustion. *Energy & Fuels*, 24(2):1402–1413, 2010.

[73] Ivan Gogolev, Amir H. Soleimanisalim, Carl Linderholm, and Anders Lyngfelt. Commissioning, performance benchmarking, and investigation of alkali emissions in a 10 kWth solid fuel chemical looping combustion pilot. *Fuel*, 287:119530, 2021.

[74] A. Abad, T. Mattisson, A. Lyngfelt, and M. Rydén. Chemical-looping combustion in a 300 W continuously operating reactor system using a manganese-based oxygen carrier. *Fuel*, 85(9):1174–1185, 2006.

[75] M. Johansson, T. Mattisson, and A. Lyngfelt. Investigation of Mn_3O_4 With Stabilized ZrO_2 for Chemical-Looping Combustion. *Chemical Engineering Research and Design*, 84(9):807–818, 2006.

[76] E. Jerndal, T. Mattisson, and Anders Lyngfelt. Thermal analysis of chemical-looping combustion. *Chemical Engineering Research and Design*, 84:795–806, 2006.

[77] Juan Adanez, Alberto Abad, Francisco Garcia-Labiano, Pilar Gayan, and Luis F. de Diego. Progress in chemical-looping combustion and reforming technologies. *Progress in Energy and Combustion Science*, 38(2):215–282, 2012.

[78] Magnus Rydén, Henrik Leion, Tobias Mattisson, and Anders Lyngfelt. Combined oxides as oxygen-carrier material for chemical-looping with oxygen uncoupling. *Applied Energy*, 113:1924–1932, 2014.

[79] Henrik Leion, Yngve Larring, Egil Bakken, Rune Bredesen, Tobias Mattisson, and Anders Lyngfelt. Use of $CaMn_{0.875}Ti_{0.125}O_3$ as Oxygen Carrier in Chemical-Looping with Oxygen Uncoupling. *Energy & Fuels*, 23(10):5276–5283, 2009.

[80] Magnus Rydén, Anders Lyngfelt, and Tobias Mattisson. $CaMn_{0.875}Ti_{0.125}O_3$ as oxygen carrier for chemical-looping combustion with oxygen uncoupling (CLOU)—Experiments in a continuously operating fluidized-bed reactor system. *International Journal of Greenhouse Gas Control*, 5(2):356–366, 2011.

[81] Malin Källén, Magnus Rydén, Cristina Dueso, Tobias Mattisson, and Anders Lyngfelt. $CaMn_{0.9}Mg0_{0.1}O_{3-\delta}3$ as Oxygen Carrier in a Gas-Fired 10 kWthChemical-Looping Combustion Unit. *Industrial & Engineering Chemistry Research*, 52(21):6923–6932, 2013.

[82] Dazheng Jing, Marijke Jacobs, Peter Hallberg, Anders Lyngfelt, and Tobias Mattisson. Development of $CaMn_{0.775}Mg_{0.1}Ti_{0.125}O_{3-\delta}$ oxygen carriers produced from different Mn and Ti sources. *Materials & Design*, 89:527–542, 2016.

[83] Peter Hallberg, Malin Hanning, Magnus Rydén, Tobias Mattisson, and Anders Lyngfelt. Investigation of a calcium manganite as oxygen carrier during 99h of operation of chemical-looping combustion in a 10 kWth reactor unit. *International Journal of Greenhouse Gas Control*, 53:222–229, 2016.

[84] Chonghe Li, Kitty Chi Kwan Soh, and Ping Wu. Formability of ABO3 perovskites. *Journal of Alloys and Compounds*, 372(1):40–48, 2004.

[85] L. S. Johansson, C. Tullin, B. Leckner, and P. Sjövall. Particle emissions from biomass combustion in small combustors. *Biomass and Bioenergy*, 25(4):435–446, 2003.

[86] W.C. Hinds. *Aerosol Technology - Properties, behavior and measurement of airborne particles*. Wiley, New York, 1999.

[87] Wei Wang, Romain Lemaire, Ammar Bensakhria, and Denis Luart. Review on the catalytic effects of alkali and alkaline earth metals (AAEMs) including sodium, potassium, calcium and magnesium on the pyrolysis of lignocellulosic biomass and on the co-pyrolysis of coal with biomass. *Journal of Analytical and Applied Pyrolysis*, 163:105479, 2022.

[88] Stanislav V. Vassilev, David Baxter, Lars K. Andersen, and Christina G. Vassileva. An overview of the composition and application of biomass ash. part 1. phase–mineral and chemical composition and classification. *Fuel*, 105:40–76, 2013.

[89] Jacob N. Knudsen, Peter A. Jensen, and Kim Dam-Johansen. Transformation and Release to the Gas Phase of Cl, K, and S during Combustion of Annual Biomass. *Energy & Fuels*, 18(5):1385–1399, 2004.

[90] Joakim M. Johansen, Jon G. Jakobsen, Flemming J. Frandsen, and Peter Glarborg. Release of K, Cl, and S during Pyrolysis and Combustion of High-Chlorine Biomass. *Energy & Fuels*, 25(11):4961–4971, 2011.

[91] Placid A. Tchoffor, Kent O. Davidsson, and Henrik Thunman. Transformation and release of potassium, chlorine, and sulfur from wheat straw under conditions relevant to dual fluidized bed gasification. *Energy & Fuels*, 27(12):7510–7520, 2013.

[92] John G. Olsson, Ulf Jäglid, Jan B. C. Pettersson, and Pia Hald. Alkali metal emission during pyrolysis of biomass. *Energy & Fuels*, 11(4):779–784, 1997.

[93] A. L. Elled, L. E. Åmand, and B. M. Steenari. Composition of agglomerates in fluidized bed reactors for thermochemical conversion of biomass and waste fuels: Experimental data in comparison with predictions by a thermodynamic equilibrium model. *Fuel*, 111:696–708, 2013.

[94] Pirita Mikkanen, Esko I. Kauppinen, Jouni Pyykönen, Jorma K. Jokiniemi, Minna Aurela, Esa K. Vakkilainen, and Kauko Janka. Alkali salt ash formation in four finnish industrial recovery boilers. *Energy & Fuels*, 13(4):778–795, 1999.

[95] Henrik Leion, Tobias Mattisson, and Anders Lyngfelt. Solid fuels in chemical-looping combustion. *International Journal of Greenhouse Gas Control*, 2(2):180–193, 2008.

[96] Kent Davidsson, Lars-Erik Åmand, Britt-Marie Steenari, A. L. Elled, D. Eskilsson, and B. Leckner. Countermeasures against alkali-related problems during combustion of biomass in a circulating fluidized bed boiler. *Chemical Engineering Science*, 63:5314–5329, 2008.

[97] Maria Zevenhoven, Christoffer Sevonius, Patrik Salminen, Daniel Lindberg, Anders Brink, Patrik Yrjas, and Leena Hupa. Defluidization of the oxygen carrier ilmenite – laboratory experiments with potassium salts. *Energy*, 148:930–940, 2018.

[98] Jelena Marinkovic, Henrik Thunman, Pavleta Knutsson, and Martin Seemann. Characteristics of olivine as a bed material in an indirect biomass gasifier. *Chemical Engineering Journal*, 279:555–566, 2015.

[99] Matthias Kuba, Hanbing He, Friedrich Kirnbauer, Dan Boström, Marcus Öhman, and Hermann Hofbauer. Deposit build-up and ash behavior in dual fluid bed steam gasification of logging residues in an industrial power plant. *Fuel Processing Technology*, 139:33–41, 2015.

[100] Matthias Kuba, Friedrich Kirnbauer, and Hermann Hofbauer. Influence of coated olivine on the conversion of intermediate products from decomposition of biomass tars during gasification. *Biomass Conversion and Biorefinery*, 7(1):11–21, 2017.

[101] Pavleta Knutsson, Valentina Cantatore, Martin Seemann, Pui Lam Tam, and Itai Panas. Role of potassium in the enhancement of the catalytic activity of calcium oxide towards tar reduction. *Applied Catalysis B: Environmental*, 229:88–95, 2018.

[102] Kawnish Kirtania, Joel Axelsson, Leonidas Matsakas, Paul Christakopoulos, Kentaro Umeki, and Erik Furusjö. Kinetic study of catalytic gasification of wood char impregnated with different alkali salts. *Energy*, 118:1055–1065, 2017.

[103] Capucine Dupont, Timothée Nocquet, José Augusto Da Costa, and Christèle Verne-Tournon. Kinetic modelling of steam gasification of various woody biomass chars: Influence of inorganic elements. *Bioresource Technology*, 102(20):9743–9748, 2011.

[104] Capucine Dupont, Sylvain Jacob, Khalil Ould Marrakchy, Céline Hognon, Maguelone Grateau, Françoise Labalette, and Denilson Da Silva Perez. How inorganic elements of biomass influence char steam gasification kinetics. *Energy*, 109:430–435, 2016.

[105] Naoki Shimada, H. Kawamoto, and S. Saka. Different action of alkali/alkaline earth metal chlorides on cellulose pyrolysis. *Journal of Analytical and Applied Pyrolysis*, 81(1):80–87, 2008.

[106] Pushkaraj R. Patwardhan, Justinus A. Satrio, Robert C. Brown, and Brent H. Shanks. Influence of inorganic salts on the primary pyrolysis products of cellulose. *Bioresource Technology*, 101(12):4646–4655, 2010.

[107] Kaige Wang, Jing Zhang, Brent H. Shanks, and Robert C. Brown. The deleterious effect of inorganic salts on hydrocarbon yields from catalytic pyrolysis of lignocellulosic biomass and its mitigation. *Applied Energy*, 148:115–120, 2015.

[108] Viktor Andersson, Amir H. Soleimanisalim, Xiangrui Kong, Fredrik Hildor, Henrik Leion, Tobias Mattisson, and Jan B. C. Pettersson. Alkali-wall interactions in a laboratory-scale reactor for chemical looping combustion studies. *Fuel Processing Technology*, 217:106828, 2021.

[109] G. Nurk, T. Huthwelker, A. Braun, Chr Ludwig, E. Lust, and R. P. W. J. Struis. Redox dynamics of sulphur with Ni/GDC anode during SOFC operation at mid- and low-range temperatures: An operando S K-edge XANES study. *Journal of Power Sources*, 240:448–457, 2013.

[110] Marco Wellinger, Serge Biollaz, Jörg Wochele, and Christian Ludwig. Sampling and online analysis of alkalis in thermal process gases with a novel surface ionization detector. *Energy & Fuels*, 25(9):4163–4171, 2011.

[111] Mikko Hupa, Oskar Karlström, and Emil Vainio. Biomass combustion technology development – it is all about chemical details. *Proceedings of the Combustion Institute*, 36(1):113–134, 2017.

[112] S. C. Cha and M. Spiegel. Local reactions of KCl particles with iron, nickel and chromium surfaces. *Materials and Corrosion*, 57(2):159–164, 2006.

[113] J. Pettersson, J. E. Svensson, and L. G. Johansson. KCl-Induced Corrosion of a 304-type Austenitic Stainless Steel in O2 and in O2 + H2O Environment: The Influence of Temperature. *Oxidation of Metals*, 72(3):159–177, 2009.

[114] T. Jonsson, H. Larsson, S. Karlsson, H. Hooshyar, M. Sattari, J. Liske, J. E. Svensson, and L. G. Johansson. High-Temperature Oxidation of FeCr(Ni) Alloys: The Behaviour After Breakaway. *Oxidation of Metals*, 87(3):333–341, 2017.

[115] Jingxin Sui, Juho Lehmusto, Mikael Bergelin, and Leena Hupa. Initial oxidation mechanisms of stainless steel Sanicro 28 (35Fe27Cr31Ni) exposed to KCl, NaCl, and K_2CO_3 under dry and humid conditions at 535°C. *Corrosion Science*, 155:29–45, 2019.

[116] M. Aho, T. Envall, and J. Kauppinen. Corrosivity of flue gases during co-firing chinese biomass with coal at fluidised bed conditions. *Fuel Processing Technology*, 105:82–88, 2013.

[117] Peter Glarborg and Paul Marshall. Mechanism and modeling of the formation of gaseous alkali sulfates. *Combustion and Flame*, 141(1):22–39, 2005.

[118] Håkan Kassman, Jesper Pettersson, Britt-Marie Steenari, and Lars-Erik Åmand. Two strategies to reduce gaseous KCl and chlorine in deposits during biomass combustion — injection of ammonium sulphate and co-combustion with peat. *Fuel Processing Technology*, 105:170–180, 2013.

[119] Sven Andersson, Evalena W. Blomqvist, Linda Bäfver, Frida Jones, Kent Davidsson, Jan Froitzheim, Martin Karlsson, Erik Larsson, and Jesper Liske. Sulfur recirculation for increased electricity production in waste-to-energy plants. *Waste Management*, 34(1):67–78, 2014.

[120] Robin Faust, Ali Valizadeh, Ren Qiu, Alyona Tormachen, Jelena Maric, Teresa Berdugo Vilches, Nils Skoglund, Martin Seemann, Mats Halvarsson, Marcus Öhman, and Pavleta Knutsson. Role of surface morphology on bed material activation during indirect gasification of wood. *Fuel*, 333:126387, 2023.

[121] Robin Faust, Teresa Berdugo Vilches, Per Malmberg, Martin Seemann, and Pavleta Knutsson. Comparison of Ash Layer Formation Mechanisms on Si-Containing Bed Material during Dual Fluidized Bed Gasification of Woody Biomass. *Energy & Fuels*, 34(7):8340–8352, 2020.

[122] Penelope Monkhouse. On-line diagnostic methods for metal species in industrial process gas. *Progress in Energy and Combustion Science*, 28(4):331–381, 2002.

[123] Wubin Weng, Christian Brackmann, Tomas Leffler, Marcus Aldén, and Zhongshan Li. Ultraviolet Absorption Cross Sections of KOH and KCl for Nonintrusive Species-Specific Quantitative Detection in Hot Flue Gases. *Analytical Chemistry*, 91(7):4719–4726, 2019.

[124] T. Leffler, C. Brackmann, M. Alden, and Z. S. Li. Laser-induced photofragmentation fluorescence imaging of alkali compounds in flames. *Applied Spectroscopy*, 71(6):1289–1299, 2017.

[125] C. Erbel, M. Mayerhofer, P. Monkhouse, M. Gaderer, and H. Spliethoff. Continuous in situ measurements of alkali species in the gasification of biomass. *Proceedings of the Combustion Institute*, 34(2):2331–2338, 2013.

[126] Alexey Sepman, Yngve Ögren, Zhechao Qu, Henrik Wiinikka, and Florian M. Schmidt. Real-time in situ multi-parameter tdlas sensing in the reactor core of an entrained-flow biomass gasifier. *Proceedings of the Combustion Institute*, 36(3):4541–4548, 2017.

[127] Emil Thorin and Florian M. Schmidt. TDLAS-based photofragmentation spectroscopy for detection of K and KOH in flames under optically thick conditions. *Optics Letters*, 45(18):5230–5233, 2020.

[128] Jan Viljanen, Thomas Allgurén, Yueming Wang, Xiaolong Li, Juha Toivonen, Klas Andersson, and Jost O. L. Wendt. In-situ monitoring of transient gas phase K–Cl–S chemistry in a pilot-scale combustor. *Proceedings of the Combustion Institute*, 38(1):1823–1831, 2021.

[129] Dan Gall, Charlotta Nejman, Thomas Allguren, Klas Andersson, and Jan B. C. Pettersson. A new technique for real-time measurements of potassium and sodium aerosols based on field-reversal surface ionization. *Measurement Science and Technology*, 32(7):075802, 2021.

[130] Dirk Porbatzki, Michael Stemmler, and Michael Müller. Release of inorganic trace elements during gasification of wood, straw, and miscanthus. *Biomass and Bioenergy*, 35:S79–S86, 2011.

[131] T. Ferge, J. Maguhn, K. Hafner, F. Mühlberger, M. Davidovic, R. Warnecke, and R. Zimmermann. On-line analysis of gas-phase composition in the combustion chamber and particle emission characteristics during combustion of wood and waste in a small batch reactor. *Environmental Science & Technology*, 39(6):1393–1402, 2005.

[132] M.R. Canagaratna, J.T. Jayne, J.L. Jimenez, J.D. Allan, M.R. Alfarra, Q. Zhang, T.B. Onasch, F. Drewnick, H. Coe, A. Middlebrook, A. Delia, L.R. Williams, A.M. Trimborn, M.J. Northway, P.F. DeCarlo, C.E. Kolb, P. Davidovits, and D.R. Worsnop. Chemical and microphysical characterization of ambient aerosols with the aerodyne aerosol mass spectrometer. *Mass Spectrometry Reviews*, 26(2):185–222, 2007.

[133] Peter Sommersacher, Norbert Kienzl, Thomas Brunner, and Ingwald Obernberger. Simultaneous Online Determination of S, Cl, K, Na, Zn, and Pb Release from a Single Particle during Biomass Combustion. Part 2: Results from Test Runs with Spruce and Straw Pellets. *Energy & Fuels*, 30(4):3428–3440, 2016.

[134] Dan Gall, Mohit Pushp, Anton Larsson, Kent Davidsson, and Jan B. C. Pettersson. Online measurements of alkali metals during start-up and operation of an industrial-scale biomass gasification plant. *Energy & Fuels*, 32(1):532–541, 2018.

[135] Viktor Andersson, Yaxin Ge, Xiangrui Kong, and Jan B. C. Pettersson. A novel method for on-line characterization of alkali release and thermal stability of materials used in thermochemical conversion processes. *Energies*, 15(12):4365, 2022.

[136] Viktor Andersson, Amir H. Soleimanisalim, Xiangrui Kong, Henrik Leion, Tobias Mattisson, and Jan B. C. Pettersson. Alkali interactions with a calcium manganite oxygen carrier used in chemical looping combustion. *Fuel Processing Technology*, 227:107099, 2022.

[137] Y. X. Ge, S. M. Ding, X. R. Kong, E. Kantarelis, K. Engvall, M. Ohman, and J. B. C. Pettersson. Effects of used bed materials on char gasification: Investigating the role of element migration using online alkali measurements. *Fuel Processing Technology*, 238, 2022.

[138] Y. X. Ge, S. M. Ding, X. R. Kong, E. Kantarelis, K. Engvall, and J. B. C. Pettersson. Real-time monitoring of alkali release during CO_2 gasification of different types of biochar. *Fuel*, 327, 2022.

[139] Mohit Pushp, Dan Gall, Kent Davidsson, Martin Seemann, and Jan B. C. Pettersson. Influence of bed material, additives, and operational conditions on alkali metal and tar concentrations in fluidized bed gasification of biomass. *Energy & Fuels*, 32(6):6797–6806, 2018.

[140] Dan Gall, Mohit Pushp, Kent O. Davidsson, and Jan B. C. Pettersson. Online measurements of alkali and heavy tar components in biomass gasification. *Energy & Fuels*, 31(8):8152–8161, 2017.

[141] Particle Instruments. Model 3062 diffusion dryer - instruction manual, 2003.

[142] Ulf Jäglid, John G. Olsson, and Jan B. C. Pettersson. Detection of sodium and potassium salt particles using surface ionization at atmospheric pressure. *Journal of Aerosol Science*, 27(6):967–977, 1996.

[143] Magnus Hagström, Klas Engvall, and Jan B. C. Pettersson. Desorption kinetics at atmospheric pressure: Alkali metal ion emission from hot platinum surfaces. *The Journal of Physical Chemistry B*, 104(18):4457–4462, 2000.

[144] Kent Davidsson, Klas Engvall, Magnus Hagström, John Korsgren, Benny Lönn, and Jan Pettersson. A surface ionization instrument for on-line measurements of alkali metal components in combustion: Instrument description and applications. *Energy & Fuels*, 16, 2002.

[145] K. H. Kingdon. A method for the neutralization of electron space charge by positive ionization at very low gas pressures. *Physical Review*, 21(4):408–418, 1923.

[146] Kenneth Möller and Leif Holmlid. Desorption of cesium from pyrolytic graphite basal surfaces with strongly non-equilibrium behaviour. *Surface Science*, 163(1):L635–L640, 1985.

[147] F. Stienkemeier, M. Wewer, F. Meier, and H. O. Lutz. Langmuir–Taylor surface ionization of alkali (Li, Na, K) and alkaline earth (Ca, Sr, Ba) atoms attached to helium droplets. *Review of Scientific Instruments*, 71(9):3480–3484, 2000.

[148] Maria Svane, Magnus Hagström, and Jan B. C. Pettersson. Online measurements of individual alkali-containing particles formed in biomass and coal combustion: Demonstration of an instrument based on surface ionization technique. *Energy & Fuels*, 19(2):411–417, 2005.

[149] Maria Svane, Torbjörn L. Gustafsson, Borka Kovacevik, Jun Noda, Patrik U. Andersson, E. Douglas Nilsson, and Jan B. C. Pettersson. On-line chemical analysis of individual alkali-containing aerosol particles by surface ionization combined with time-of-flight mass spectrometry. *Aerosol Science and Technology*, 43(7):653–661, 2009.

[150] Yaxin Ge, Saiman Ding, Wennan Zhang, Xiangrui Kong, Klas Engvall, and Jan B. C. Pettersson. Effect of fresh bed materials on alkali release and thermogravimetric behavior during straw gasification. *Fuel*, 336:127143, 2023.

[151] Yaxin Ge, Saiman Ding, Xiangrui Kong, Efthymios Kantarelis, Klas Engvall, and Jan B. C. Pettersson. Online monitoring of alkali release during co-pyrolysis/gasification of forest and agricultural waste: Element migration and synergistic effects. *Biomass and Bioenergy*, 172:106745, 2023.

[152] The World Material. Grade 304 stainless steel properties, tensile yield strength, thermal conductivity.

[153] Daniel A. Knopf, Ulrich Pöschl, and Manabu Shiraiwa. Radial diffusion and penetration of gas molecules and aerosol particles through laminar flow reactors, denuders, and sampling tubes. *Analytical Chemistry*, 87(7):3746–3754, 2015.

[154] Keith J. Laidler and John M. Meiser. *Physical Chemistry*. Benjamin Cummings, Menlo Park, CA, 1982.

[155] I.L. Mostinsky. Diffusion coefficient, 2011.

[156] A. M. Huntz, A. Reckmann, C. Haut, C. Sévérac, M. Herbst, F. C. T. Resende, and A. C. S. Sabioni. Oxidation of aisi 304 and aisi 439 stainless steels. *Materials Science and Engineering: A*, 447(1):266–276, 2007.

[157] A. Khanna. *High Temperature Oxidation and Corrosion*. 2002.

[158] Hiroshi Nakagawa and Yoichi Ono. Effects of potassium chloride on the reduction of iron oxides. *Transactions of the Iron and Steel Institute of Japan*, 25(10):1021–1024, 1985.

[159] James D. Batteas and James H. Helt. Surface chemistry.

[160] Tom Blomberg, P. Makkonen, and M. Hiltunen. Role of alkali hydroxides in the fireside corrosion of heat transfer surfaces, a practical approach. *Materials Science Forum - MATER SCI FORUM*, 461-464:883–890, 2004.

[161] V. N. Kondratev. *Chemical Kinetics of Gas Reactions*. Pergamon Press, London, England, 1964.

[162] Arturo Cabello, Alberto Abad, María T. Izquierdo, P. Gayán, Luis F. de Diego, Francisco García-Labiano, and Juan Adánez. Qualification of operating conditions to extend oxygen carrier utilization in the scaling up of chemical looping processes. *Chemical Engineering Journal*, 430:132602, 2022.

[163] C. Linderholm, M. Schmitz, M. Biermann, M. Hanning, and A. Lyngfelt. Chemical-looping combustion of solid fuel in a 100kw unit using sintered manganese ore as oxygen carrier. *International Journal of Greenhouse Gas Control*, 65:170–181, 2017.

[164] Jochen Ströhle, Matthias Orth, and Bernd Epple. Design and operation of a 1MWth chemical looping plant. *Applied Energy*, 113:1490–1495, 2014.